Journal of Nanomaterials

Hierarchical Nanostructures: Novel Synthetic Strategies and Advanced Applications 2022

Lead Guest Editor: Nguyen Duc Cuong
Guest Editors: Tran Xuan Mau, Mai Duy Hien, and Duong Tuan Quang

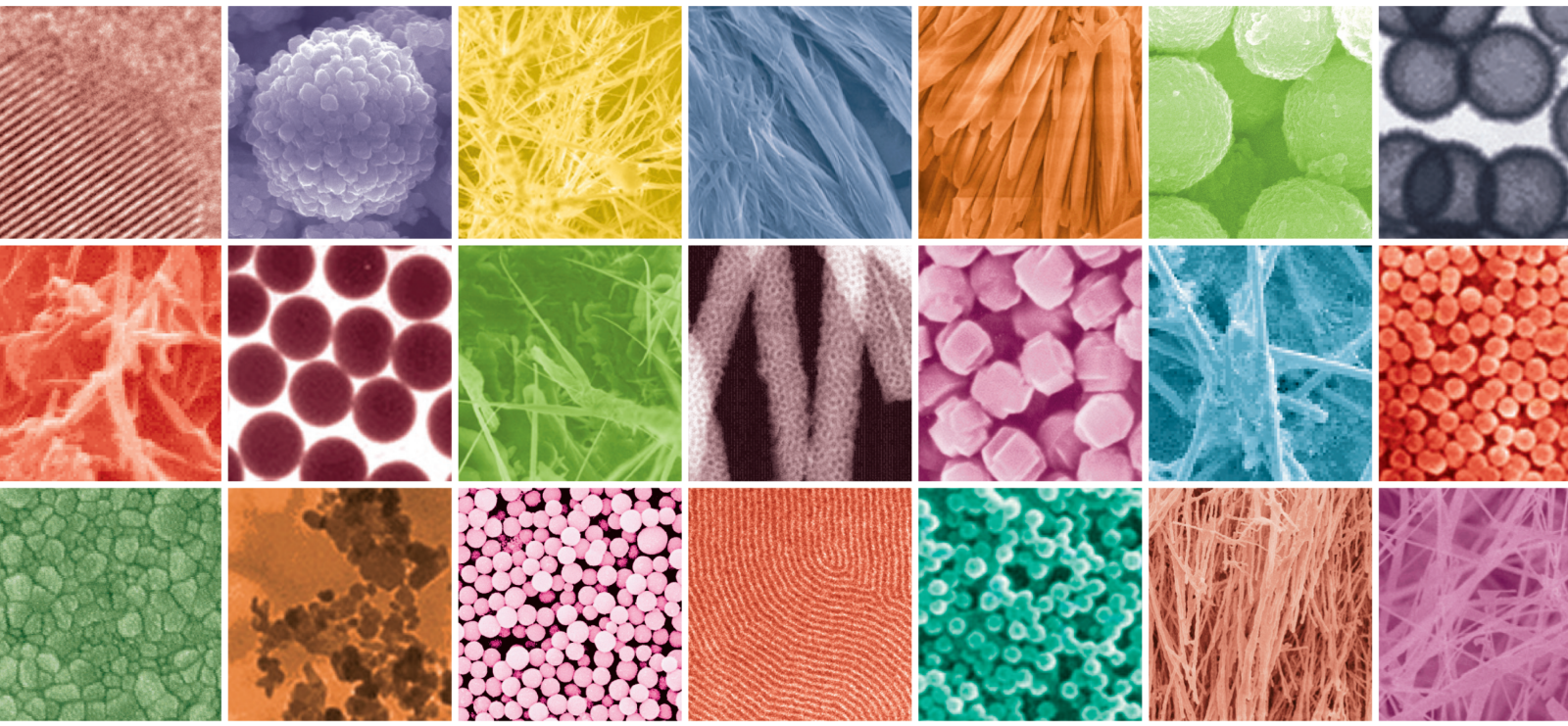

Hierarchical Nanostructures: Novel Synthetic Strategies and Advanced Applications 2022

Journal of Nanomaterials

Hierarchical Nanostructures: Novel Synthetic Strategies and Advanced Applications 2022

Lead Guest Editor: Nguyen Duc Cuong
Guest Editors: Tran Xuan Mau, Mai Duy Hien, and Duong Tuan Quang

Contents

Hindawi
Journal of Nanomaterials
Volume 2022, Article ID 8630685, 11 pages
https://doi.org/10.1155/2022/8630685

Research Article

Zinc/Cobalt-Based Zeolite Imidazolate Frameworks for Simultaneously Degrading Dye and Inhibiting Bacteria

Nguyen Thi Thanh Tu,[1] **Lu Hoang Khang**,[1] **Nguyen Ngoc Phuong Thao**,[1] **Nguyen Thi Thu Hien**,[2] **Thuy Chau To**,[2] **Le Thi Hong Diep**,[3] **Le Van Thanh Son**,[4] **Phan Lien**,[4] **Vo Thang Nguyen**,[4] **and Dinh Quang Khieu**[5]

[1]*Faculty of Applied Technology, School of Engineering and Technology, Van Lang University, 700000, Vietnam*
[2]*Thu Dau Mot University, Binh Duong 75000, Vietnam*
[3]*Faculty of Environmental & Food Engineering, Nguyen Tat Thanh University, 700000, Vietnam*
[4]*University of Education and Science, The University of Danang, 500000, Vietnam*
[5]*University of Sciences, Hue University, 530000, Vietnam*

Correspondence should be addressed to Nguyen Thi Thanh Tu; tu.ntt@vlu.edu.vn
and Dinh Quang Khieu; dqkhieu@hueuni.edu.vn

Received 4 May 2022; Revised 25 August 2022; Accepted 15 September 2022; Published 30 September 2022

Academic Editor: Mai Duy Hien

In this work, the zinc/cobalt-based zeolite imidazolate frameworks ((Co/Zn)ZIFs) were synthesized with the solvothermal method. The obtained material was characterized by utilizing scanning electron microscopy (SEM), X-ray diffraction (XRD), UV-Vis diffusive reflectance spectroscopy, and nitrogen adsorption-desorption isotherms. XRD and SEM analyses show that (Co/Zn)ZIFs are composed of nanocrystals with polyhedral shapes of around 50–100 nm and belong to the I-43m space group as those of ZIF-8 and ZIF-67. Optical studies demonstrate a red shift in the absorbance spectrum of (Co/Zn)ZIFs compared with individual components of ZIF-67 or ZIF-8. (Co/Zn)ZIF composite was utilized as photocatalytic material to treat a model aqueous solution containing rhodamine B and bacteria. It was found that (Co/Zn)ZIFs could simultaneously degrade rhodamine B and inhibit bacteria (*E. coli* and *S. aureus*). The manufactured composite could catalyze the mineralization of rhodamine B and also exhibited good antibacterial activity against Gram-negative *E. coli* (93.32% inhibition rate) and Gram-positive *S. aureus* (90.86% inhibition rate) in the visible-light region within four hours of irradiation. Gram-negative bacteria were more resistant to (Co/Zn)ZIFs than Gram-positive bacteria. (Co/Zn)ZIFs can be used as light-driven catalysts for water and environmental detoxification from organic compounds like dyes and bacteria.

1. Introduction

The rapid development of industrialization in recent years has contributed to significant economic growth. At the same time, environmental pollution is also at an alarming level, affecting the living environment of humans and animals. In particular, wastewater from industrial production facilities, especially wastewater from textile dyeing factories, poses a severe threat to the environment. The presence of dyes in wastewater is a major concern because of their toxicity and unaesthetic that can cause adverse effects on biological life, including cancer and genetic mutations [1–3]. In addition, the presence of bacteria in water also affects the environment, especially strains of enterobacteria and Gram-negative, anaerobic bacteria, including *Escherichia coli* (*E. coli*), being able to cause diseases on the digestive tract in humans and animals. Therefore, developing friendly and effective techniques to degrade dyes and, at the same time, disinfect wastewater has become a vital and urgent issue in environmental protection. Numerous techniques for separate treatment of dyes or bacteria have been reported. Physicochemical methods have been developed to treat dye wastewater, such as

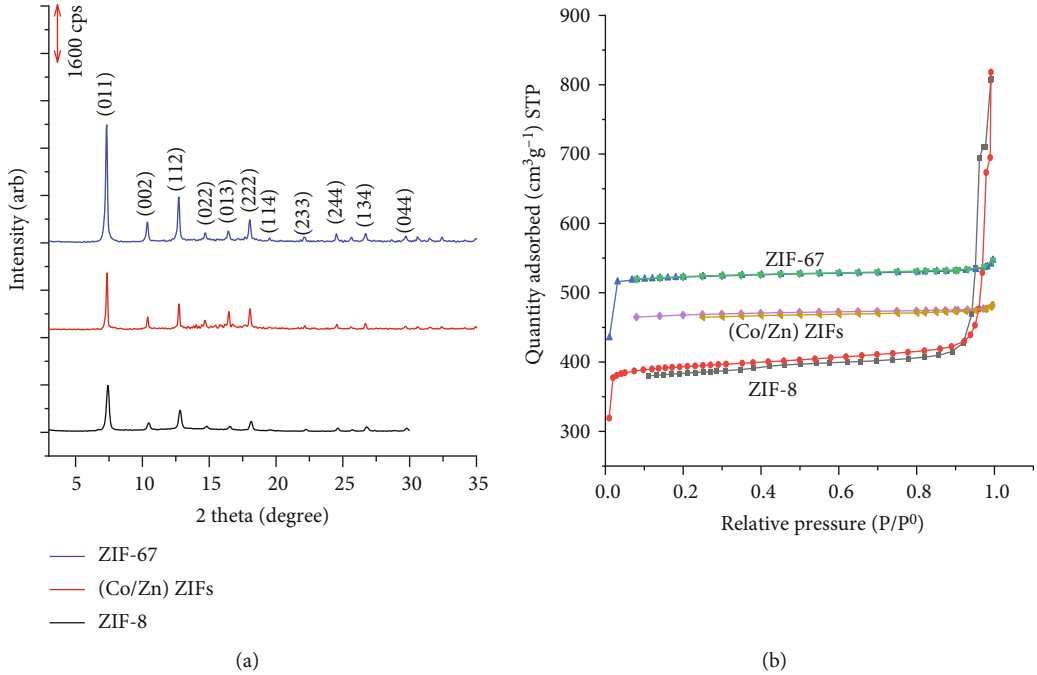

Figure 1: (a) XRD diagram and (b) nitrogen adsorption and desorption isotherms of ZIF-67, ZIF-8, and (Co/Zn)ZIFs.

biochemical oxidation [4], adsorption [5–7], ion exchange [8, 9], photocatalysis [10, 11], and advanced oxidation [12]. Recently, several oxide or metal nanoparticles exhibiting antibacterial activity or both antibacterial and organic compound degradation activities have been reported. Nair et al. addressed the antibacterial activity of ZnO- and Co-doped ZnO nanoparticles on Gram-positive and Gram-negative bacteria [13]. Valerini et al. presented that Ag-coated polycaprolactone exhibited an excellent antibacterial action against *E. coli* [14]. In another study, Rao et al. found that Ag nanoparticles/g-C_3N_4 nanosheets showed efficient photocatalytic and antibacterial performance [15].

ZIFs (zeolitic imidazole frameworks) are a class of metal-organic frameworks (MOFs) formed from tetrahedral divalent cations ($M^{2+} = Zn^{2+}$ or Co^{2+}) with imidazolate ligands [16, 17]. Most ZIFs have a large bandgap energy (E_g); for example, E_g of ZIF-67 and ZIF-8 is 4.3 and 5.3 eV [18]. Therefore, reducing E_g to improve the photocatalytic performance of ZIFs in the visible-light region is essential and has practical significance. Chen et al. [19] reported that ZnO/ZIF-8 was an effective photocatalyst for completely degrading methylene blue. Yang et al. [20] added Cu to ZIF-67 to promote the catalytic activity of Cu/ZIF-67 for methyl orange decomposition in the visible-light region. Zhou et al. [17] synthesized ZIFs based on Zn/Co for the first time with improved chemical properties compared with single ZIF-8 or ZIF-67. Taheri et al. reported the antibacterial activity of ZIF-8 for *E. coli* [21]. According to our best knowledge, research on the photocatalytic activity of this kind of material for simultaneously degrading dyes and inhibiting bacteria is less available. Therefore, developments of ZIFs with antimicrobial properties are of considerable interest. In the present study, we present the synthesis of (Co/Zn)ZIFs with the hydrothermal method and the photocatalytic activity toward rhodamine B. The antimicrobial activity of (Co/Zn)ZIFs against *E. coli* ATCC 25922 (Gram-negative) and *S. aureus* ATCC 25923 (Gram-positive) in aqueous solutions was also addressed.

2. Experimental

2.1. Materials. Cobalt nitrate ($Co(NO_3)_2{\cdot}6H_2O$, Deajung, Korea), 2-methylimidazole ($C_4H_6N_2$, Sigma, USA) (Hmim), methanol (CH_3OH, Guangzhou, China), ethanol (C_2H_5OH, Guangzhou, China), zinc nitrate ($Zn(NO_3)_2{\cdot}6H_2O$, Deajung, Korea), and rhodamine B ($C_{28}H_{31}ClN_2O_3$, denoted RhB) were used in the study.

2.2. Preparation of ZIF-8, ZIF-67, and (Co/Zn)ZIFs. ZIF-8, ZIF-67, and (Co/Zn)ZIFs were synthesized according to references [22, 23]. For ZIF-67, 1.164 g of $Co(NO_3)_2{\cdot}6H_2O$ and 1.312 g of 2-methylimidazole were dissolved in 100 mL of CH_3OH. The mixture was placed in a Teflon autoclave and kept in an oven at 150°C for 5 h. The product was then centrifuged for 15 min (1500 rpm). The obtained solid was rinsed three times with ethanol. Then, the resulting purple solid was dried at 120°C for about 24 h to obtain the ZIF-67. ZIF-8 was synthesized with the same procedure with $Zn(NO_3)_2{\cdot}6H_2O$ (1.188 g). A series of (Co/Zn)ZIFs with different molar Co/Zn ratios (1 : 9), (2 : 8), (3 : 7), (5 : 5), (6 : 4), and (7 : 3) was synthesized in a similar manner by using a mixture of $Co(NO_3)_2{\cdot}6H_2O$ and $Zn(NO_3)_2{\cdot}6H_2O$. In a preliminary test, (Co/Zn)ZIFs with Co/Zn molar ratio of 6/4 exhibit high photocatalytic and antibacterial activity; therefore, this material was selected for further experiments (Table S1).

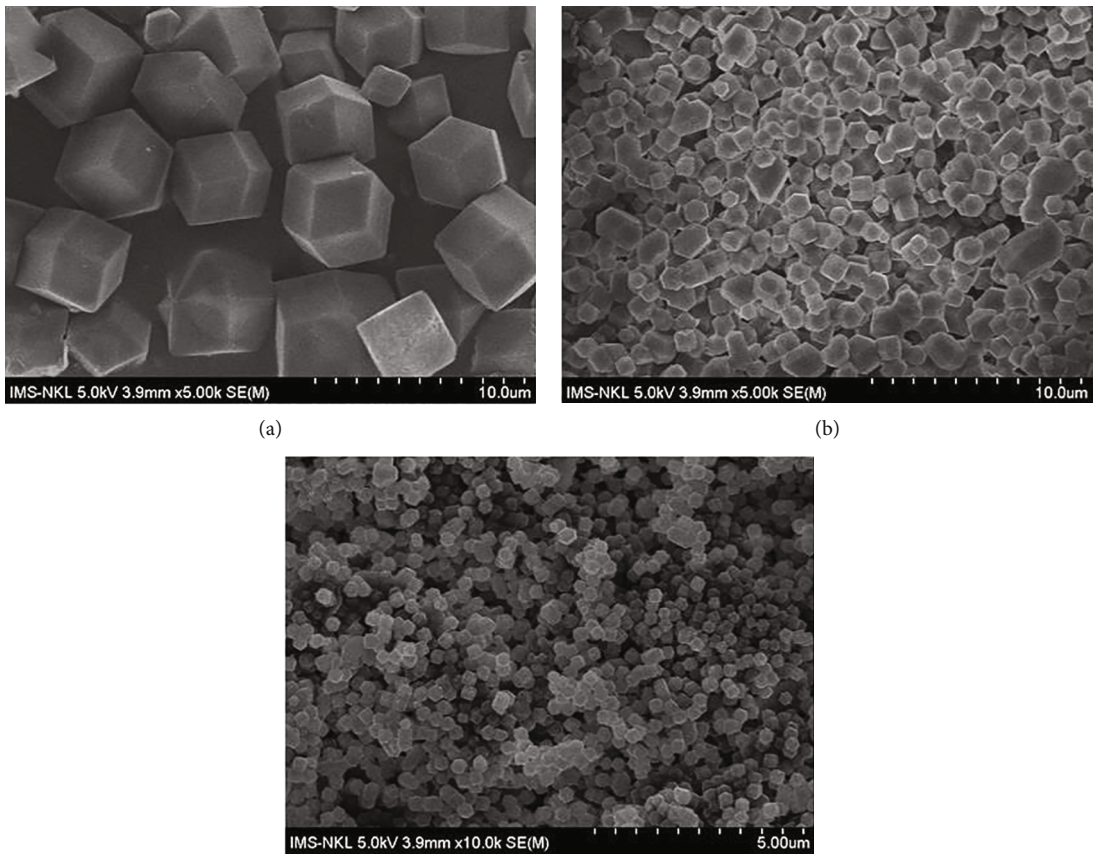

(a) (b)

(c)

Figure 2: SEM images of ZIF-67 (a), ZIF-8 (b), and (Co/Zn)ZIFs (c).

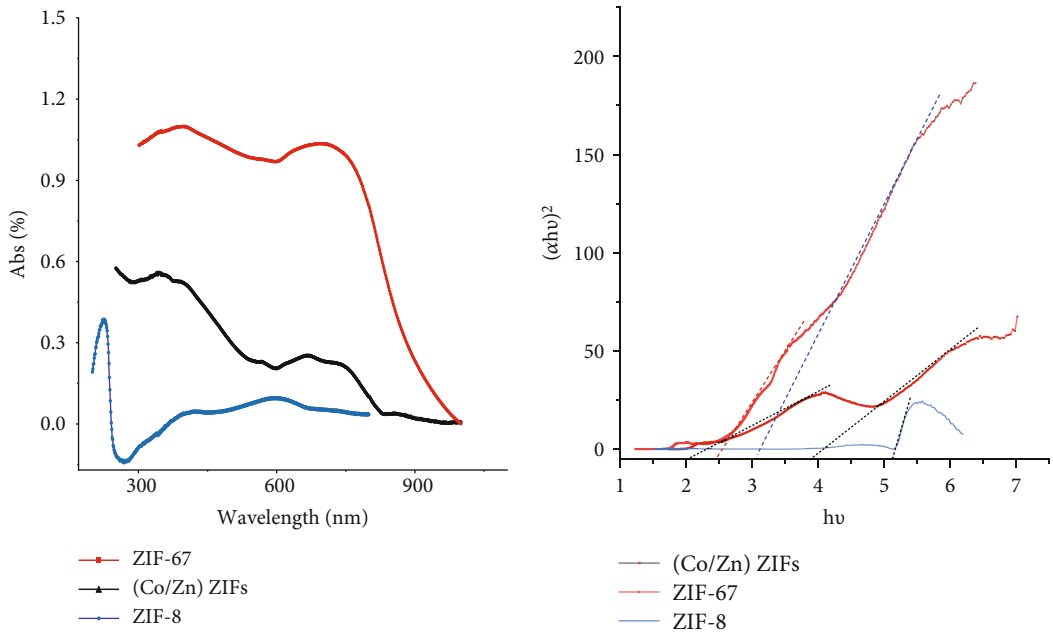

(a) (b)

Figure 3: UV-Vis DRS spectra (a) and Tauc's plots of (Co/Zn)ZIFs, ZIF-67, and ZIF-8 (b).

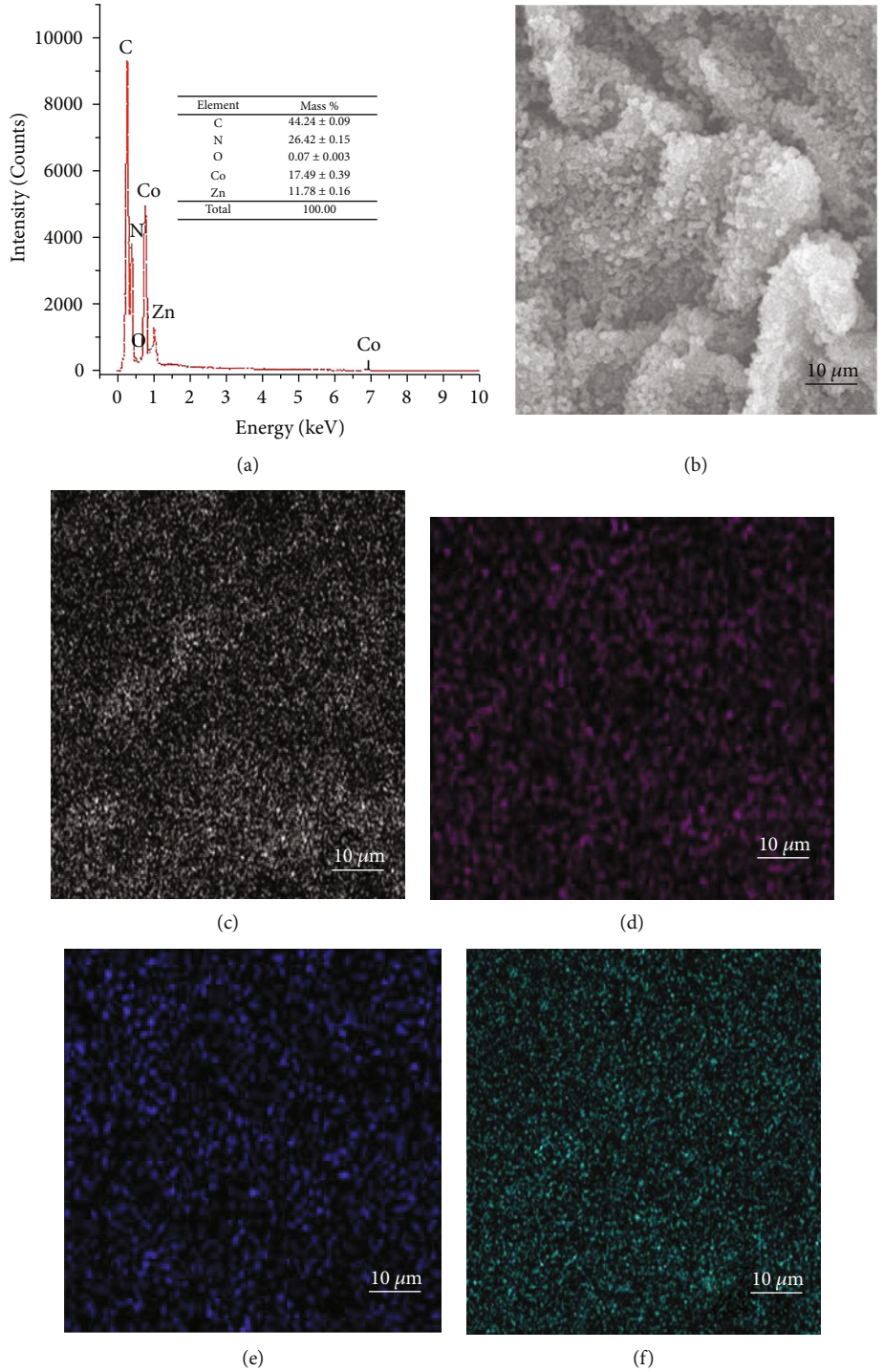

Figure 4: EDX spectrum of (Co/Zn)ZIFs (a), SEM image (b), carbon mapping (c), nitrogen mapping (d), cobalt mapping (e), and zinc mapping (f).

2.3. Apparatus. The powder X-ray diffraction (XRD) was performed on D8 Advance, Bruker (Germany). The morphology of ZIF-8, ZIF-67, and (Co/Zn)ZIFs was observed from scanning electron microscopy (SEM JMS-5300LV, Japan) images. Textural properties were investigated by means of nitrogen adsorption-desorption isotherms (Micrometrics TriStar 3000 at 77 K). The elemental composition of samples was detected by EDX mapping (JSM-IT200 InTouchScope). UV-Vis spectroscopy was measured by using a Lambda 25 Spectrophotometer-Perkin Elmer at λ_{max} of RhB (553 nm). Total organic carbon (TOC) was measured on TOC-VCPH/CP (Shimadzu).

2.4. Bacterial Strains and Growing Conditions. Gram (–) *Escherichia coli* ATCC 25922 (*E. coli*) and Gram (+) *Staphylococcus aureus* ATCC 25923 (*S. aureus*) were used to study

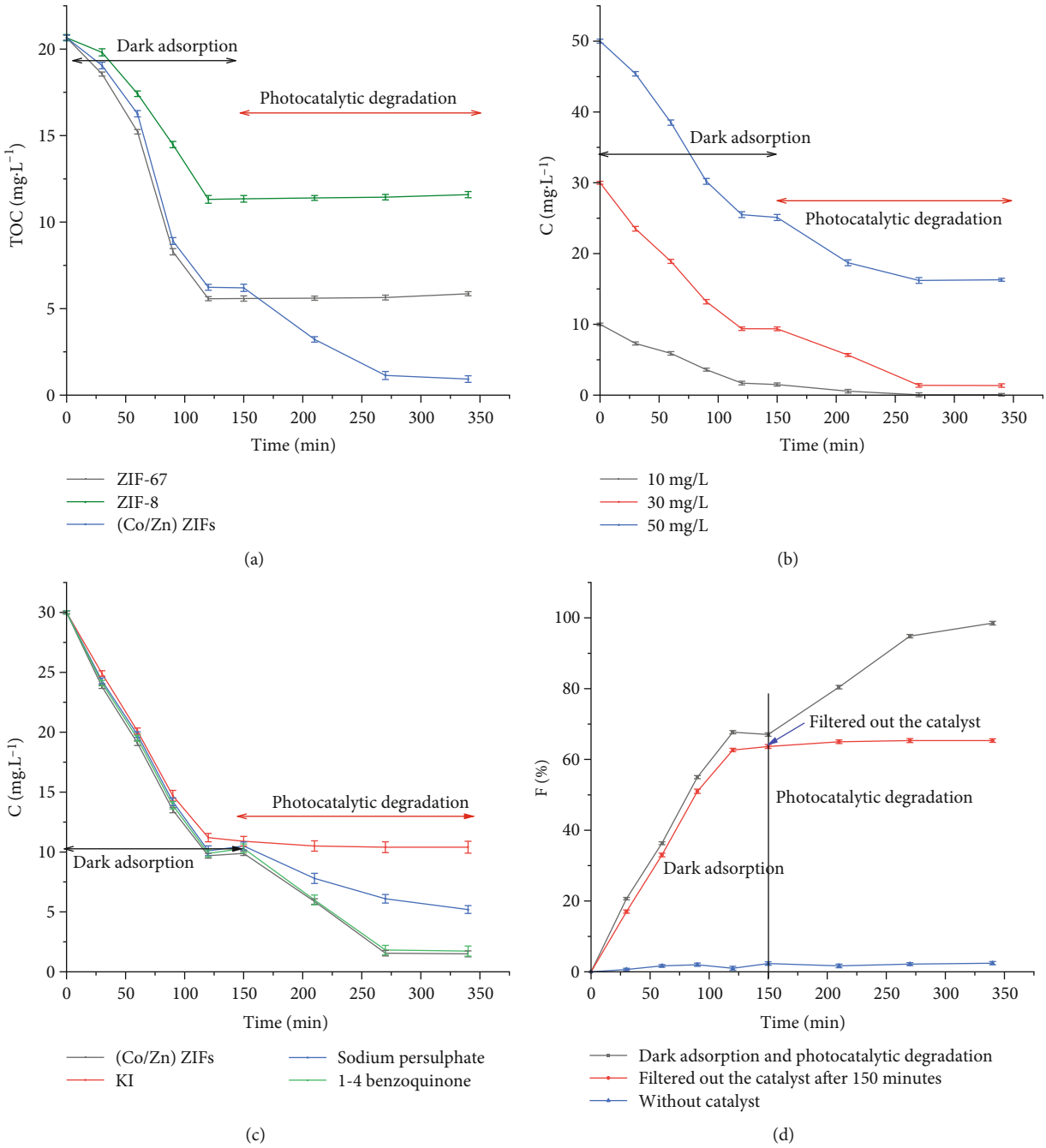

Figure 5: (a) Visible light-driven photocatalytic degradation of RhB on different ZIF materials (experimental condition: $V = 1000$ mL; the initial concentration is from 30 mg·L^{-1}; the adsorbent mass is 0.1 g) and (b) kinetics of decolorization on (Co/Zn)ZIFs (experimental condition: $V = 1000$ mL; the initial concentration is from 10, 30, and 50 mg·L^{-1}; the adsorbent mass is 0.1 g). (c) Effect of photogenerated carrier scavenger on photodegradation of RhB. (d) Leaching (experimental conditions: $V = 1000$ mL, mass of catalyst = 0.1 g, dark adsorption in 150 min, and photodegradation in 340 min).

the antibacterial activity of the synthesized products. The *E. coli* strain culture was grown in LB (Luria–Bertani) broth, and *S. aureus* was grown in TS (tryptic soy) broth.

2.5. Visible-Light-Derived Photocatalytic Activity for RhB Degradation and Antibacterial Activity against E. coli and S. aureus with (Co/Zn)ZIFs. 0.1 g of each ZIF-67, ZIF-8, and (Co/Zn)ZIF material was placed into a 1000 mL beaker containing 500 mL of RhB solution (30 mg·L^{-1}) and *E. coli* and *S. aureus* strains (10^6–10^7 CFU·mL^{-1}). The beakers were sealed and placed in the dark to prevent light exposure, and the mixture was stirred with a magnetic stirrer for 120 min to reach adsorption/desorption equilibrium. Then, an Osram 160 W filament lamp (filter cutoff $\lambda < 420$ nm) illuminated the resulting suspension. 5 mL of suspension was withdrawn at defined intervals and then centrifuged to remove the solid. The mineralization degree of RhB in the supernatant was estimated with the total organic carbon

measurement. Each experiment was repeated three times. Simultaneously, 100 μL of the solution was taken, diluted 10,000 times, and spread on LB or TSB agar plates (incubated at 37°C; the number of colonies was recorded after 24 h to assess the antibacterial activity of the material via the plate spread method).

The antibacterial rate was utilized to assess the antibacterial activity according to the following equation:

$$H\,(\%) = \frac{C_{CS} - C_{SS}}{C_{CS}} \times 100\%, \quad (1)$$

where C_{SS} and C_{CS} are the bacterial population of the survey and control samples ($CFU{\cdot}mL^{-1}$).

The kinetics study was performed in a similar manner on RhB solution at initial concentrations of 10, 30, and 50 ppm. The concentration of remaining RhB in the supernatant was determined with a UV-Vis adsorption spectroscope at λ_{max} equal to 553 nm.

3. Results and Discussion

3.1. Characterization of Materials. Figure 1 shows the XRD patterns of the ZIF-67, ZIF-8, and (Co/Zn)ZIF samples. The spatial distances d of the faces (011), (002), (112), (022), (113), (222), and (114) of ZIF-8 or ZIF-67 are in good agreement with those reported previously [17, 24–26]. Since both ZIF-67 and ZIF-8 crystallize in the crystal system I-43m [20], the diffraction peaks of (Co/Zn)ZIFs are observed at the same 2θ as ZIF-67 and ZIF-8 with an intermediate intensity between ZIF-67 and ZIF-8. The surface area and pore properties of the materials were investigated by measuring nitrogen adsorption and desorption at 77 K (Figure 1(b)). The adsorption and desorption isotherms follow the type I according to the IUPAC classification. All samples have a microporous structure. However, the isotherm of ZIF-8 rises remarkably at high relative pressures, indicating that a mesoporous capillary system was formed between the particles.

The BET-specific surface area of ZIF-67, ZIF-67, and (Co/Zn)ZIFs calculated from the N_2 adsorption and desorption isotherm is 1530, 1176, and 1325 $m^2{\cdot}g^{-1}$, respectively. The pore size distribution calculated from the Barrett-Joyner-Halenda model shows that ZIF-67 and (Co/Zn)ZIFs have almost the same pore width (around 20 Å), indicating their structural similarities. In addition, the adsorption on (Co/Zn)ZIFS is fast with saturation at a relative pressure of less than 0.1, confirming its microporous structure, analogous to ZIF.

The morphology of ZIF-67, ZIF-8, and (Co/Zn)ZIFs is presented in Figure 2. While ZIF-67 consists of polyhedron particles with a diameter ranging from 200 to 500 nm, (Co/Zn)ZIFs retain the polyhedral morphology of ZIF-67, yet with a smaller size (50–200 nm).

To assess the optical absorption capacity of the as-prepared ZIFs, we calculated the bandgap (E_g) of the material by using UV–Vis diffuse reflection spectroscopy (Figure 3(a)). The bandgap of a material can be obtained from the Kubelka–Munk function formula.

Table 1: A comparison of rate coefficient of (Co/Zn)ZIFs with other previously reported materials.

Catalyst	C_{RhB} ($mg{\cdot}L^{-1}$)	k_r (min^{-1})	Reference
$BiVO_4$	5	0.00102	[30]
$CuO–ZrO_2$	10	0.0006	[31]
ZnO	5	0.0028	[32]
CuO	5	0.0203	[32]
ZnO/CuO	5	0.0326	[32]
(ZnO/CuO)/rGO	5	0.0627	[32]
ZnO	5	0.0203	[33]
ZnO/g–C_3N_4	5	0.0284	[33]
(Co/Zn)ZIFs	10	0.028	This work
(Co/Zn)ZIFs	30	0.016	This work
(Co/Zn)ZIFs	50	0.004	This work

$$\alpha \times h \times \nu = A \times \left(h \times \nu - E_g\right)^{n/2}, \quad (2)$$

where α, h, ν, A, and E_g are the absorption coefficient, Plank's constant, light frequency, proportionality constant, and bandgap energy, respectively; $n = 1$ and 4, corresponding to direct and indirect bandgap semiconductors. Figure 3(b) presents the fitting diagram of $(\alpha \times h \times \nu)^2$ vs. $h \times \nu$ for the indirect bandgap [27]. Thus, extrapolating the linear region to the abscissa yields the bandgap energy of the material. Two bandgaps are found at 2.05 and 3.98 eV for ZIF-67, while only one bandgap is around 5.18 eV for ZIF-8. (Co/Zn)ZIFs have two bandgaps at around 2.45 and 3.05 eV. The high bandgap energy at 5.18 and 3.98 eV for ZIF-8 and ZIF-67 can mainly be attributed to the charge transfer between the ligand and the metals [28]. The low bandgap of ZIF-67 (2.05 eV), corresponding to the characteristic absorption band at 500–650 nm, is attributed to the typical d - d transition in tetrahedral cobalt [29]. Furthermore, the bandgap of (Co/Zn)ZIFs is lower than that of ZIF-8 or ZIF-67, indicating that the combination of Co and Zn reduces the energy required for optical transition and can promote its photocatalytic activity.

The distribution of the elements in the composite was studied with EDX mapping (Figure 4). As expected, the EDX spectrum shows the presence of five elements: Zn (11.78%), Co (17.49%), C (44.24%), O (0.07%), and N (26.42%). The elements randomly disperse throughout the sample surface, indicating the composite homogeneous phase.

3.2. Rhodamine B Degradation and Antibacterial Activity of ZIF-67, ZIF-8, and (Co/Zn)ZIFs. The elimination of RhB with ZIF-67, ZIF-8, and (Co/Zn)ZIFs might occur in two steps: adsorption and photocatalytic degradation. The ability to eliminate RhB was evaluated *via* the decrease of TOC, which is expressed as elimination efficiency (F)

$$F = \frac{100 * (C_0 - C_t)}{C_0}, \quad (3)$$

where C_0 is the initial TOC and C_t is TOC at time t.

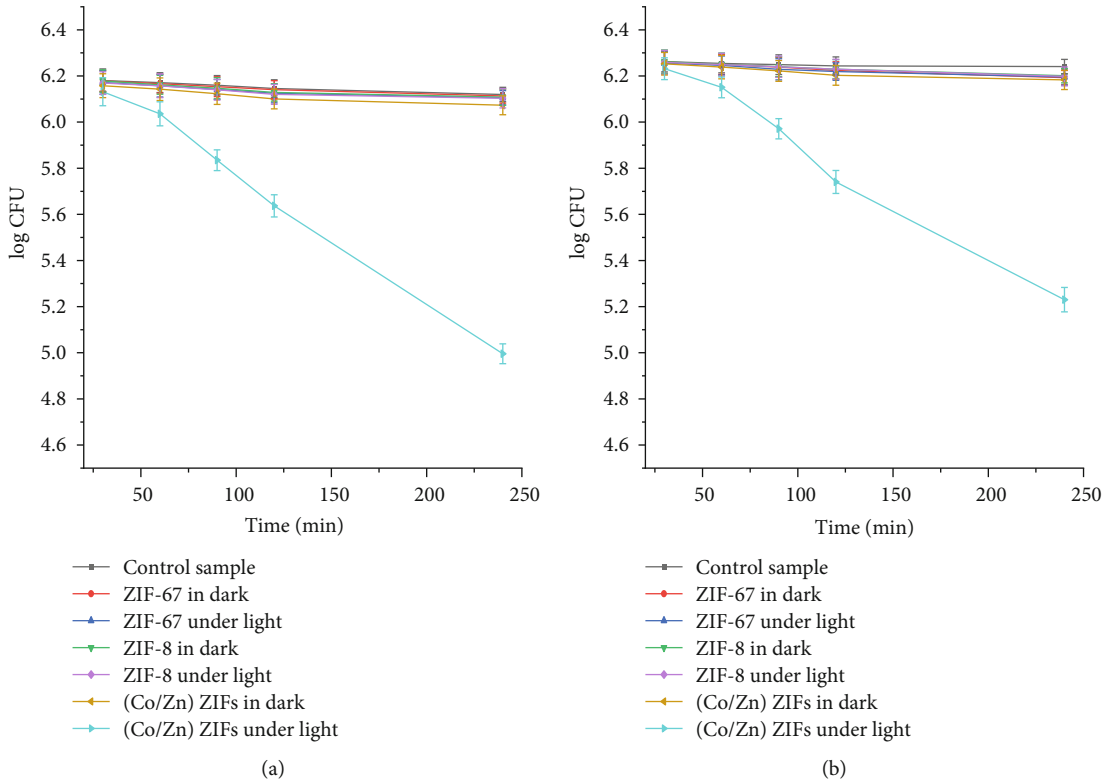

Figure 6: Variation of logarithm of bacterial population of *E. coli* (a) and *S. aureus* (b) with different treatment materials in the dark and under visible-light illumination at different times (each experiment in triplicate).

The adsorption was carried out in the dark for 120 min (to ensure that the adsorption/desorption equilibrium was reached), and then, the light turned up. The TOC data show that ZIF-67, (Co/Zn)ZIFs, and ZIF-8 adsorb a significant amount of RhB in the aqueous solution. The adsorption efficiency of ZIF-67, (Co/Zn)ZIFs, and ZIF-8 is 79.8, 68.7, and 45.6%, respectively (Figure 5(a)). However, ZIF-67 and ZIF-8 do not exhibit any photocatalytic activity under the visible light region. The decreasing TOCs of the solutions treated with ZIF-8 and ZIF-67 are due only to adsorption, whereas (Co/Zn)ZIFs catalyze the degradation of RhB up to 95.5% under illumination. Figure 5(a) shows that TOC decreases from 20.66 to 0.93 $mg{\cdot}L^{-1}$ for the RhB solution treated with (Co/Zn)ZIFs, in which the decrease of 14.19 $mg{\cdot}L^{-1}$ is due to adsorption and 5.54 $mg{\cdot}L^{-1}$ due to photocatalytic degradation.

The leaching experiment was also performed where the catalyst was filtered after 150 min of reaction; the decolorization of RhB almost stopped despite further illumination (Figure 5(c)). This halt indicates that (Co/Zn)ZIF is a heterogeneous catalyst in the photocatalytic degradation of RhB. Because heterogeneous catalysts usually leach the metal ions to the solution, the presence of Zn and Co in the supernatant was detected by using AAS. The results show that a small amount of zinc is present, but cobalt is detected a very small amount in the solution (Table S2). It is possible that the Co-imidazole bond (Co–N) is stronger than the Zn-imidazole bond (Zn–N) because cobalt possesses higher electronegativity (1.88) than zinc (1.65).

The kinetics of the decomposition of RhB on (Co/Zn)ZIFs was studied by using the Hinshelwood–Langmuir model for heterogeneous catalysis at different concentrations in the reduced form as follows:

$$\ln\left(\frac{C_t}{C_0}\right) = -k_r \times t, \tag{4}$$

where k_r is the decomposition rate constant (min^{-1}) and C_0 and C_t are the concentration of RhB at equilibrium in the dark and at time t of photocatalysis. The results (Figure 5(b)) show that the decomposition rate coefficient (k_r) decreases gradually from 0.028 to 0.004 min^{-1} when the RhB concentration increases from 10 to 50 $mg{\cdot}L^{-1}$. RhB at a higher concentration might prevent light from interacting with the catalyst, reducing the photocatalytic efficiency and thus the degradation rate. It is difficult to compare the decomposition rate coefficient because the data are derived from different reaction conditions. However, the k_r value of RhB decomposition in this study is comparable to that of other previously reported studies if the initial concentration is concerned (Table 1).

The antibacterial activity of ZIF materials in an aqueous solution was evaluated by comparing the number of viable bacterial cells after contact with the material with the control sample (without ZIF). Figure 6 shows that ZIF-67 and ZIF-8 have poor antibacterial performance on both *S. aureus* and *E. coli*, with cell survival rates ranging from 87 to 96% with

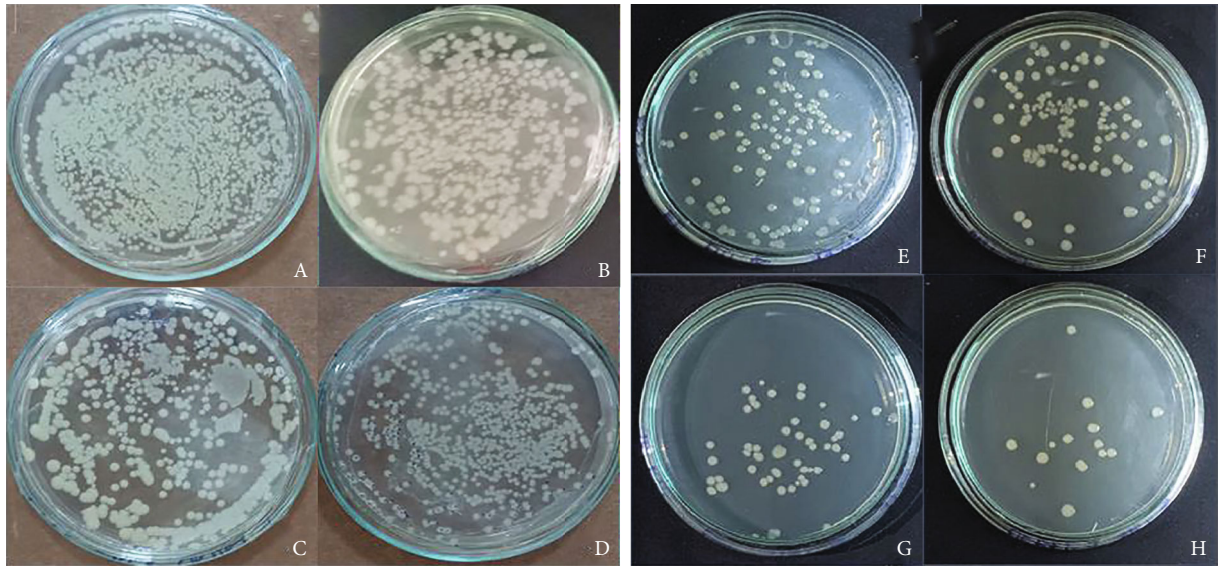

(a) (b)

Figure 7: Cell density of bacterial *E. coli* (a) in the dark (A: control sample, B: 60 min, C: 120 min, and D: 240 min). Cell density of bacterial *E. coli* (b) under illumination (E: control sample, F: 60 min, G: 120 min, and H: 240 min).

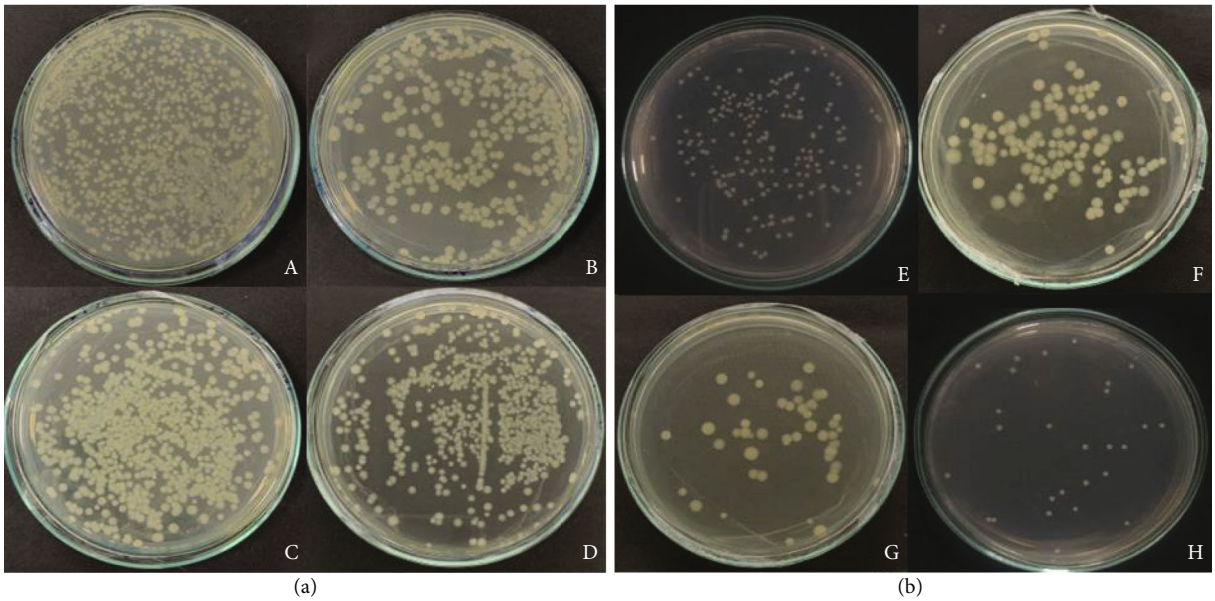

(a) (b)

Figure 8: Cell density of bacterial *S. aureus* (a) in the dark (A: control sample, B: 60 min, C: 120 min, and D: 240 min). Cell density of bacterial *S. aureus* (b) under illumination (E: control sample, F: 60 min, G: 120 min, and H: 240 min).

or without light illumination. However, (Co/Zn)ZIFs have much higher antibacterial activity against both *S. aureus* and *E. coli* without light. Specifically, in the presence of light, (Co/Zn)ZIFs exhibit excellent antibacterial activity on *S. aureus* and *E. coli* strains with a survival rate of 9.14 and 6.68%. The photographs of Petri dishes obtained from *E. coli* and *S. aureus* culture without or with (Co/Zn)ZIFs in the dark and under illumination are shown in Figures 7 and 8. As expected, the *E. coli* and *S. aureus* cultures in the absence of (Co/Zn)ZIFs, *i.e.*, the control samples, continue to grow within four hours (Figures 7(a), 7(e), 8(a), and 8(e)) regardless of lighting or not. The results also show that Gram-negative bacteria *E. coli* are more sensitive to the (Zn/Co)ZIFs than Gram-positive bacteria *S. aureus* because of the difference in their cell membrane structure [34].

Table 2 shows that (Co/Zn)ZIFs have antibacterial activities against Gram-positive and Gram-negative bacteria equivalent to some previously reported materials.

The (Co/Zn)ZIF material is a potential photocatalyst, capable of decolorizing RhB and also inhibiting microorganisms. ZIF-8 and ZIF-67 have large E_g and therefore are not excited under visible light. Combining Zn with Co creates a catalyst with photochemical degradation ability under visible light. This ability of (Co/Zn)ZIFs may result from the

Table 2: A comparison of antibacterial activity of (Co/Zn)ZIF with other materials reported previously.

Materials	Bacterial strains	Antibacterial activity	References
RFP&o-NBA@ZIF-8	*E. coli*	Inhibition rate of 95% against *E. coli* under light condition during 12 hours	[35]
MOF-53(Fe)/Van	*S. aureus*	Inhibition rate of 99.3% against *S. aureus* at concentration 200 $\mu g \cdot mL^{-1}$ of MOF-53(Fe)/Van	[36]
HKUST-1/OCBs	*E. coli*	Growth inhibition of bacteria: 90.2%	[37]
CP/CNF/ZIF-67	*E. coli*	Antibacterial rate reached 80%	[38]
WO_{3-X}	*E. coli* and *S. aureus*	Inhibition rate of 100% against *E. coli* and *S. aureus* at 100 $\mu g \cdot mL^{-1}$ after six hours of contact	[39]
(Co/Zn)ZIFs	*E. coli* and *S. aureus*	Inhibition rate 90.86% against *S. aureus* and 93.8% against *E. coli* after four hours of contact under visible light condition	The present study

addition of Zn to the intermediate band formation between the conduction (CB) and valence (VB) regions of ZIF-67 and ZIF-8. Visible light can excite electrons from VB, and an energy state adds to the Co3d level to CB, causing electron formation (e^-) and photogenerated hole (h^+). The e^-/h^+ pair initiates the reduction or oxidation of O_2 and H_2O in the solution to generate free radicals. These free radicals oxidize organic pollutants to form mineral products. The photocatalytic reaction can occur as follows:

$$\begin{gathered}\left(\frac{\mathrm{Co}}{\mathrm{Zn}}\right)\mathrm{ZIFs} + h\nu \longrightarrow \left(\frac{\mathrm{Co}}{\mathrm{Zn}}\right)\mathrm{ZIFs}\left(\frac{\mathrm{h}^+}{\mathrm{e}^-}\right)\\ \mathrm{e}^- + \mathrm{O}_2 \longrightarrow \mathrm{O}_2{}^{*-}\\ \left(\frac{\mathrm{Co}}{\mathrm{Zn}}\right)\mathrm{ZIFs}\left(\mathrm{h}^+\right) + \mathrm{H}_2\mathrm{O} \longrightarrow {}^{\cdot}\mathrm{OH} + \mathrm{H}^+ + \left(\frac{\mathrm{Co}}{\mathrm{Zn}}\right)\mathrm{ZIFs}\left(\mathrm{h}^+\right)\\ \frac{{}^{\cdot}\mathrm{OH}}{\mathrm{O}_2{}^{*-}} + \mathrm{RhB} \longrightarrow \text{Decomposition products}\end{gathered} \tag{5}$$

The free radicals ${}^{\cdot}OH/O_2{}^{*-}$ can oxidize and damage cell membranes, organelles, and bacterial DNA, resulting in the destruction of bacteria. This pathway is also considered one of many materials' principal bactericidal mechanisms, as reported in previous studies [8–12, 34, 40–43].

4. Conclusion

The ZIF-8, ZIF-67, and (Zn/Co)ZIF materials synthesized with the solvothermal method have uniform morphology with a large surface area. Under visible light, (Zn/Co)ZIFs exhibit high photocatalytic activity toward the RhB degradation and, simultaneously, inhibit *E. coli* and *S. aureus*, while ZIF-8 and ZIF-67 do not. The synergistic system ZIF-67/ZIF-8 for simultaneous dye degradation and bacteria inhibition suggests a new approach for developing multifunctional materials for environmental treatments.

Data Availability

The data used to support the findings of this study are available from the corresponding authors upon request.

Conflicts of Interest

The authors declare that they have no conflicts of interest.

Acknowledgments

This study was financially supported by the Van Lang University, Vietnam.

Supplementary Materials

Table S1: the (Co/Zn)ZIF sample with Co/Zn molar ratio of 6/4 presents highest photocatalytic and antibacterial activity; therefore, this material was selected for further experiments. Table S2: metal elements were leached out but a small amount of zinc is present, but cobalt is detected a very small amount. *(Supplementary Materials)*

References

[1] M. Rafatullah, O. Sulaiman, R. Hashim, and A. Ahmad, "Adsorption of methylene blue on low-cost adsorbents: a review," *Journal of Hazardous Materials*, vol. 177, no. 1-3, pp. 70–80, 2010.

[2] K.-T. Chung, "Azo dyes and human health: a review," *Journal of Environmental Science and Health, Part C*, vol. 34, no. 4, pp. 233–261, 2016.

[3] K. Golka, S. Kopps, and Z. W. Myslak, "Carcinogenicity of azo colorants: influence of solubility and bioavailability," *Toxicology Letters*, vol. 151, no. 1, pp. 203–210, 2004.

[4] S. Ghoreishi and R. Haghighi, "Chemical catalytic reaction and biological oxidation for treatment of non-biodegradable textile effluent," *Chemical Engineering Journal*, vol. 95, no. 1-3, pp. 163–169, 2003.

[5] S. Chatterjee, M. W. Lee, and S. H. Woo, "Adsorption of Congo red by chitosan hydrogel beads impregnated with carbon nanotubes," *Bioresource Technology*, vol. 101, no. 6, pp. 1800–1806, 2010.

[6] E. Lorenc-Grabowska and G. Gryglewicz, "Adsorption characteristics of Congo red on coal-based mesoporous activated carbon," *Dyes and Pigments*, vol. 74, no. 1, pp. 34–40, 2007.

[7] I. D. Mall, V. C. Srivastava, N. K. Agarwal, and I. M. Mishra, "Removal of congo red from aqueous solution by bagasse fly ash and activated carbon: kinetic study and equilibrium isotherm analyses," *Chemosphere*, vol. 61, no. 4, pp. 492–501, 2005.

[8] C.-H. Liu, J.-S. Wu, H.-C. Chiu, S.-Y. Suen, and K. H. Chu, "Removal of anionic reactive dyes from water using anion exchange membranes as adsorbers," *Water Research*, vol. 41, no. 7, pp. 1491–1500, 2007.

[9] J.-S. Wu, C.-H. Liu, K. H. Chu, and S.-Y. Suen, "Removal of cationic dye methyl violet 2B from water by cation exchange membranes," *Journal of Membrane Science*, vol. 309, no. 1-2, pp. 239–245, 2008.

[10] U. G. Akpan and B. H. Hameed, "Parameters affecting the photocatalytic degradation of dyes using TiO2-based photocatalysts: a review," *Journal of Hazardous Materials*, vol. 170, no. 2-3, pp. 520–529, 2009.

[11] K. Rajeshwar, M. Osugi, W. Chanmanee et al., "Heterogeneous photocatalytic treatment of organic dyes in air and aqueous media," *Journal of Photochemistry and Photobiology C: Photochemistry Reviews*, vol. 9, no. 4, pp. 171–192, 2008.

[12] J. L. Wang and L. J. Xu, "Advanced oxidation processes for wastewater treatment: formation of hydroxyl radical and application," *Critical Reviews in Environmental Science and Technology*, vol. 42, no. 3, pp. 251–325, 2012.

[13] M. G. Nair, M. Nirmala, K. Rekha, and A. Anukaliani, "Structural, optical, photo catalytic and antibacterial activity of ZnO and Co doped ZnO nanoparticles," *Materials Letters*, vol. 65, no. 12, pp. 1797–1800, 2011.

[14] D. Valerini, L. Tammaro, R. Vitali, G. Guillot, and A. Rinaldi, "Sputter-deposited Ag nanoparticles on electrospun PCL scaffolds: morphology, wettability and antibacterial activity," *Coatings*, vol. 11, no. 3, p. 345, 2021.

[15] S. Rao, Y. Li, H. Liu et al., "Polyethyleneimine induced highly dispersed Ag nanoparticles over g-C_3N_4 nanosheets for efficient photocatalytic and antibacterial performance," *Ceramics International*, vol. 47, no. 6, pp. 8528–8537, 2021.

[16] L. Zhao, H.-H. Wu, C. Yang et al., "Mechanistic origin of the high performance of Yolk@Shell Bi_2S_3@N-doped carbon nanowire electrodes," *ACS Nano*, vol. 12, no. 12, pp. 12597–12611, 2018.

[17] K. Zhou, B. Mousavi, Z. Luo, S. Phatanasri, S. Chaemchuen, and F. Verpoort, "Characterization and properties of Zn/Co zeolitic imidazolate frameworks vs. ZIF-8 and ZIF-67," *Journal of Materials Chemistry A*, vol. 5, no. 3, pp. 952–957, 2017.

[18] K. T. Butler, C. H. Hendon, and A. Walsh, "Designing porous electronic thin-film devices: band offsets and heteroepitaxy," *Faraday Discussions*, vol. 201, pp. 207–219, 2017.

[19] M.-H. Chen, Q.-Y. Lu, Y.-M. Li, M.-M. Chu, and X.-B. Cao, "ZnO@ZIF-8 core–shell heterostructures with improved photocatalytic activity," *CrystEngComm*, vol. 23, no. 24, pp. 4327–4335, 2021.

[20] H. Yang, X.-W. He, F. Wang, Y. Kang, and J. Zhang, "Doping copper into ZIF-67 for enhancing gas uptake capacity and visible-light-driven photocatalytic degradation of organic dye," *Journal of Materials Chemistry*, vol. 22, no. 41, pp. 21849–21851, 2012.

[21] M. Taheri, D. Ashok, T. Sen et al., "Stability of ZIF-8 nanopowders in bacterial culture media and its implication for antibacterial properties," *Chemical Engineering Journal*, vol. 413, article 127511, 2021.

[22] N. T. T. Tu, P. C. Sy, T. T. Minh et al., "Synthesis of (Zn/Co)-based zeolite imidazole frameworks and their applications in visible light-driven photocatalytic degradation of Congo red," *Journal of Inclusion Phenomena and Macrocyclic Chemistry*, vol. 95, no. 1-2, pp. 99–110, 2019.

[23] N. T. T. Tu, T. V. Thien, P. D. Du, V. T. T. Chau, T. X. Mau, and D. Q. Khieu, "Adsorptive removal of Congo red from aqueous solution using zeolitic imidazolate framework–67," *Journal of Environmental Chemical Engineering*, vol. 6, no. 2, pp. 2269–2280, 2018.

[24] G. Zhong, D. Liu, and J. Zhang, "The application of ZIF-67 and its derivatives: adsorption, separation, electrochemistry and catalysts," *Journal of Materials Chemistry A*, vol. 6, no. 5, pp. 1887–1899, 2018.

[25] Z.-X. Y. J. Low, J. Yao, Q. Liu et al., "Crystal transformation in zeolitic-imidazolate framework," *Crystal Growth & Design*, vol. 14, no. 12, pp. 6589–6598, 2014.

[26] Y. Li, K. Zhou, M. He, and J. Yao, "Synthesis of ZIF-8 and ZIF-67 using mixed-base and their dye adsorption," *Microporous and Mesoporous Materials*, vol. 234, pp. 287–292, 2016.

[27] Q. Luo, X. Huang, Q. Deng et al., "Novel 3D cross-shaped Zn/Co bimetallic zeolite imidazolate frameworks for simultaneous removal Cr (VI) and Congo Red," *Environmental Science and Pollution Research*, vol. 29, no. 26, pp. 40041–40052, 2022.

[28] S. Bordiga, C. Lamberti, G. Ricchiardi et al., "Electronic and vibrational properties of a MOF-5 metal–organic framework: ZnO quantum dot behaviour," *Chemical Communications*, vol. 20, pp. 2300-2301, 2004.

[29] T. N. Nguyen, H. P. Nguyen, T.-H. Kim, and S. W. Lee, "Bimetallic Co/Zn-ZIF as an efficient photocatalyst for degradation of indigo carmine," *Korean Journal of Materials Research*, vol. 28, no. 1, pp. 68–74, 2018.

[30] R. Ran, J. G. McEvoy, and Z. Zhang, "Synthesis and optimization of visible light active $BiVO_4$ photocatalysts for the degradation of RhB," *International Journal of Photoenergy*, vol. 2015, Article ID 612857, 14 pages, 2015.

[31] A. H. Kianfar, M. A. Arayesh, and M. M. Momeni, "Degradation of MB and RhB by modified ZrO_2 nanoparticles via sunlight," *Applied Physics A*, vol. 127, no. 2, pp. 1–9, 2021.

[32] N. Kumaresan, M. M. A. Sinthiya, K. Ramamurthi, R. R. Babu, and K. Sethuraman, "Visible light driven photocatalytic activity of ZnO/CuO nanocomposites coupled with rGO heterostructures synthesized by solid-state method for RhB dye degradation," *Arabian Journal of Chemistry*, vol. 13, no. 2, pp. 3910–3928, 2020.

[33] R. Uma, K. Ravichandran, S. Sriram, and B. Sakthivel, "Cost-effective fabrication of ZnO/g-C_3N_4 composite thin films for enhanced photocatalytic activity against three different dyes (MB, MG and RhB)," *Materials Chemistry and Physics*, vol. 201, pp. 147–155, 2017.

[34] L. Wang, C. Hu, and L. Shao, "The antimicrobial activity of nanoparticles: present situation and prospects for the future," *International Journal of Nanomedicine*, vol. 12, pp. 1227–1249, 2017.

[35] Z. Song, Y. Wu, Q. Cao, H. Wang, X. Wang, and H. Han, "pH-responsive, light-triggered on-demand antibiotic release from functional metal-organic framework for bacterial infection combination therapy," *Advanced Functional Materials*, vol. 28, no. 23, article 1800011, 2018.

[36] S. Lin, X. Liu, L. Tan et al., "Porous iron-carboxylate metal–organic framework: a novel bioplatform with sustained antibacterial efficacy and nontoxicity," *ACS Applied Materials & Interfaces*, vol. 9, no. 22, pp. 19248–19257, 2017.

[37] C. Duan, X. Meng, C. Liu et al., "Carbohydrates-rich corncobs supported metal-organic frameworks as versatile biosorbents for dye removal and microbial inactivation," *Carbohydrate Polymers*, vol. 222, article 115042, 2019.

[38] L. Qian, D. Lei, X. Duan et al., "Design and preparation of metal-organic framework papers with enhanced mechanical properties and good antibacterial capacity," *Carbohydrate Polymers*, vol. 192, pp. 44–51, 2018.

[39] C. Bankier, R. Matharu, Y. Cheong, G. Ren, E. Cloutman-Green, and L. Ciric, "Synergistic antibacterial effects of metallic nanoparticle combinations," *Scientific Reports*, vol. 9, no. 1, pp. 1–8, 2019.

[40] W. Wang, K. J. Lu, C. H. Yu, Q. L. Huang, and Y. Z. Du, "Nano-drug delivery systems in wound treatment and skin regeneration," *Journal of nanobiotechnology*, vol. 17, no. 1, pp. 1–15, 2019.

[41] D. Liu, Y. Chen, F. Ding et al., "Simultaneous production of butanol and acetoin by metabolically engineered Clostridium acetobutylicum," *Metabolic Engineering*, vol. 27, pp. 107–114, 2015.

[42] B. Ahmed, A. K. Ojha, A. Singh et al., "Well-controlled in-situ growth of 2D WO_3 rectangular sheets on reduced graphene oxide with strong photocatalytic and antibacterial properties," *Journal of Hazardous Materials*, vol. 347, pp. 266–278, 2018.

[43] M. M. Khan, S. Kumar, T. Ahamad, and A. N. Alhazaa, "Enhancement of photocatalytic and electrochemical properties of hydrothermally synthesized WO_3 nanoparticles via Ag loading," *Journal of Alloys and Compounds*, vol. 743, pp. 485–493, 2018.

Hindawi
Journal of Nanomaterials
Volume 2022, Article ID 8677321, 5 pages
https://doi.org/10.1155/2022/8677321

Review Article

Green Plasma Electrochemical Synthesized Colloidal Silver Nanoparticles and Their Antibacterial Activity

Nguyen Thi Thu Thuy,[1,2] Nguyen Thi Thanh Bao,[3] and Do Hoang Tung[3]

[1]*Faculty of Engineering Physics and Nanotechnology, VNU University of Engineering and Technology, 144 Xuan Thuy Road, Cau Giay District, Hanoi 10000, Vietnam*
[2]*Faculty of Basic Science, University of Fire Prevention and Fighting, 243 Khuat Duy Tien, Thanh Xuan, Hanoi 10000, Vietnam*
[3]*Institute of Physics, Vietnam Academy of Science and Technology, Vietnam, 18 Hoang Quoc Viet Street, Cau Giay District, Hanoi 10000, Vietnam*

Correspondence should be addressed to Do Hoang Tung; dhtung@iop.vast.vn

Received 23 June 2022; Accepted 10 August 2022; Published 20 September 2022

Academic Editor: Nguyen Duc Cuong

Nanosilver solutions of colloidal silver nanoparticles at reasonable price, good quality, and availability are increasingly demanded for the application in agriculture and aquaculture for the prevention and treatment of diseases. In this paper, we have applied a new simple and environmental-friendly fabrication method based on a plasma electrochemical procedure, where silver nanoparticles are directly formed in the plasma environment from silver ions generated by the electrochemical process from the silver anode. The electrode dissolution rate, the formation percentage, and quality of the silver nanoparticles were examined and evaluated using atomic absorption spectroscopy, electrode mass change, transmission electron microscopy, and UV-Vis absorption spectroscopy. The silver nanoparticle formation was found of nearly 100% with the rate of about 3.3 mg per minute. Spherical nanoparticles are found in quite homogenous size distribution around about 9.7 nm in the solution. The solution of the plasma synthesized nanosilvers shows better antibacterial property in comparison to that of $AgNO_3$ of the same molar concentration on both normal and antibiotics resistant *E. coli* strains.

1. Introduction

Silver is known as the chemical element with the most powerful antibacterial properties, which are significantly enhanced when the material is in the dimensions in nanometer scale, namely, in the form of nanoparticles [1]. Silver nanoparticles (AgNPs) are widely used in agriculture and aquaculture for the prevention and treatment of diseases [1, 2] as well as in many other areas [3–8]. However, accessing to appropriately high-quality silver nanoparticle products is still a challenge for quite a number of farmers. High price due to expensive and complicated manufacture procedure is also a big barrier. In Vietnam, in accordance with the restructure and transition of the agricultural production to successfully adapt to the more and more apparent climate and environment changing conditions and also to essential improve the agriproduct quality to meet the high standard of export markets much attentions are paid to the application of new, advanced technologies and materials, among which antibacterially active metal nanoparticles and materials are highly demanded.

AgNPs have been synthesized by various physical [9–11], chemical [12, 13], and biological methods [14, 15] targeting at different application purposes [16]. They all show also diverse advantages and disadvantages with respect to the fabrication cost and time consumptions, the stability, the size distribution, the purity, and other properties. One of the most commonly used methods is the chemical reduction owing to the convenient procedure and simple and easily available equipment needed [17, 18]. However, the chemical method is the most environment-unfriendly and expensive with rather low purity synthesized AgNPs. In contrast, biological methods using naturally reducing agents, such as microorganism (bacteria or fungi) or plant extracts to obtain

AgNPs from appropriate silver salts, are environment-friendly and quite cost effective [19, 20]. Nonetheless, a major disadvantage of these methods is that the produced AgNP solutions only reach low concentrations and uncontrollable particle size distributions [16]. In comparison to these, the physical approaches have approved the ability to produce large quantities of high-purity AgNPs by different routes. It is even quite convenient to fabricate large quantity of AgNPs with well-homogeneous particle size distribution from bulk silver in just a single process [9–11]. Several groups have successfully produced good quality AgNP solutions using the plasma liquid interaction techniques [21]. Thuy [22] used two pure silver metal electrodes, one of them is submerged in the solution, and the other touched the surface of the solution. With this configuration, it is possible to produce a fairly pure AgNP solution. However, the resulting solution is still dilute (concentration was lower than 300 ppm) with rather wide particle size distribution.

In this work, we apply a plasma electrochemical method using the plasma-in-liquid configuration with both discharging electrodes from bulk silver metal submerged in the solution for the green synthesis of colloidal AgNPs. The experimental results have revealed that this low-cost fabrication method could provide high concentration and high-quality colloidal AgNP solution with high antibacterial effectiveness in a single process.

2. Materials and Experimental Methods

2.1. The Plasma Electrochemical Fabrication of the Colloidal AgNP Solution. The plasma electrochemical system for the synthesis of the colloidal AgNP solution consists of two electrodes submerged into the solution confined in a glass container and a pulsed DC high voltage up to 6 kV power source with the repetition rate of 25 Hz and the duty cycle of 50% as is shown in Figure 1. Both electrodes were covered by a Teflon tube with only a small uncovered tip part directly exposed to the solution. The cathode was a sharped molybdenum rod placed oppositely polarized to the anode in the distance of about 2 mm. The anode was a bulk silver rod (99.999% purity) with diameter of 6 mm purchased from a domestic jewelry company in Hanoi, Vietnam.

Large amount of the synthetic conditions has been investigated including pH, supply voltage, peak plasma current as well as distance between electrodes. In this present work, we perform only the best condition with pH 7, 6 kV supply voltage, 1.4 A peak plasma current, and 2 mm electrode distance. We examine only the synthesis duration and the properties of synthesised AgNPs.

The principle of AgNP formation in the plasma electrochemical system can be described with 3 stages as follows.

Stage 1. Electrolysis

At the beginning of a cycle, the system acts as an electrolysis cell. The cathodic reaction is an electrolysis of water that produces hydrogen gas in the form of bubbles:

$$2H_2O + 2e^- \longrightarrow H_2 + 2OH^-. \quad (1)$$

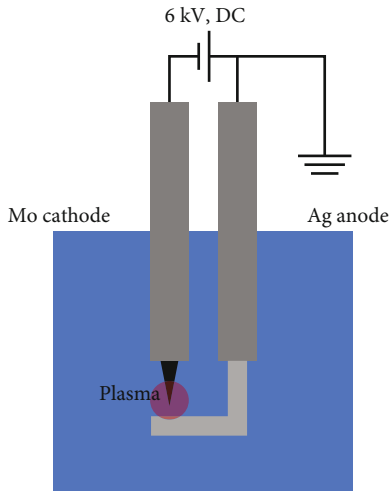

Figure 1: Plasma electrochemical system for the colloidal AgNP synthesis.

Meanwhile, on the anode side, silver is electrolyzed, releasing the Ag^+ ions into the solution:

$$Ag \longrightarrow e^- + Ag^+. \quad (2)$$

When the amount of generated hydrogen is large enough to cover the surface of the cathode and the voltage increases sufficiently (about 2 kV), the continuous electric discharge will occur; the reaction system moves to stage 2.

Stage 2. Plasma and particle formation

After the electric field between the cathode and the anode was broken down, the plasma arc was formed between the two electrodes. The original plasma was the plasma of the ionic species of hydrogen and water vapor mixture. However, the steam plasma will then prevail. During this stage, the space between the two electrodes is divided into three regions as shown in Figure 2:

(i) Electrolytic region, adjection to the anode, where Ag^+ ions continuously are released from the anode and moving towards the cathode

(ii) The reduction region, where the Ag^+ ions were reduced to silver atom Ag^0 by atomic hydrogen and electrons

(iii) Nucleation and growth region, where the silver nanonucleus were formed and grown into nanoparticles

Stage 3. Extinguishing and electrolysis

When the voltage drops to about 400 V, the plasma was no longer maintained, and the system returned to an electrolysis cell.

2.2. Estimation of the AgNP Formation Rate. Every two minutes, the anode was weighed to determine the Ag^+ release rate. Meanwhile, the AgNP solution was centrifuged to collect the generated AgNPs, and the silver content was determined by the atomic absorption spectroscopy.

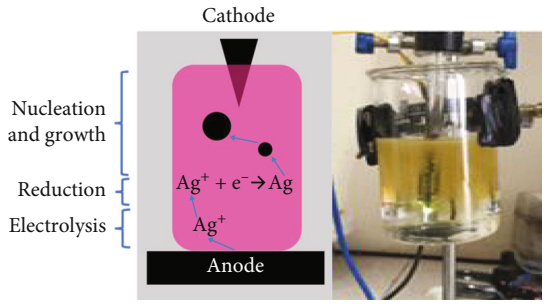

Figure 2: Structure of a plasma electrochemical system for the AgNP formation.

2.3. Characterizations of AgNPs. The morphology and particle size of AgNPs were examined by the transmission electron microscopy (TEM using the JEM 1010, JEOL system) at 80 kV. The UV–visible absorption was measured using the UV-near IR spectrometer of the type V-570 (Jasco).

2.4. Antibacterial Assays. Two bacterial strains, namely, normal and antibiotic-resistant *Escherichia coli* (ATCC 25923), were provided by the Genome Research Institute, Vietnam Academy of Science and Technology, Vietnam. The disc-diffusion technique (the so-called modified Kirby–Bauer technique) was applied to examine the antibacterial activity of AgNPs. Plastic Petri dishes were first filled with Luria–Bertani (LB) agar and then inoculated separately with two bacterial strains, respectively, of normal and antibiotic-resistant *E. coli*. Bacterial concentrations of the order of 10^8 colony-forming unit (cfu)/ml were used. Each LB agar dish was punched with four holes of 5 mm diameter. Two of these holes on each disk were filled with the $AgNO_3$ solutions and the others with the AgNP solutions of the same concentrations. Six values of concentrations of 250 ppm, 160 ppm, 80 ppm, 40 ppm, 20 ppm, and 10 ppm were examined. Zones of inhibition were determined after 24 h of incubation at temperature of 37°C.

3. Results and Discussion

Initially, the solution was colorless, then gradually turned yellow due to the formation of silver nanoparticles. The longer the plasma processing time is, the darker the solution becomes.

As can be seen in Figure 3, the measured UV-vis spectra show the spectral characteristics of silver NPs with a maximum surface plasmon resonance corresponding to a wavelength of 408 nm. The UV-vis spectra provided strong evidence of the formation of the surface-plasmon-resonance band of spherical AgNPs.

Figure 4 shows that most of the as-synthesized AgNPs are of spherical shape and homogeneous in both size and shape distribution. Particle sizes range mainly from 8 nm to 11 nm, with an average size of 9.7 nm. The AgNP distribution is not sharply homogenous, since the AgNPs formed in the plasma region can leave the region and stop their growth but others can stay or some from outside plasma region can reenter and continue to grow further.

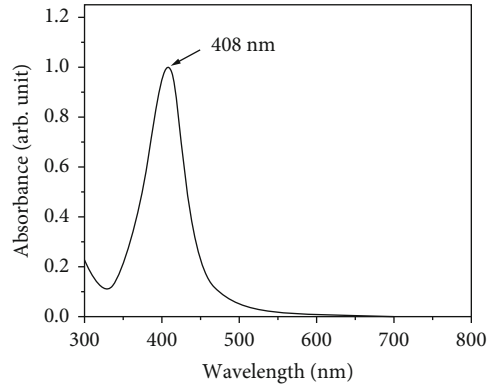

Figure 3: UV–vis spectra of the solution diluted 140 times from the 14 minutes plasma processing with the batch of 40 ml.

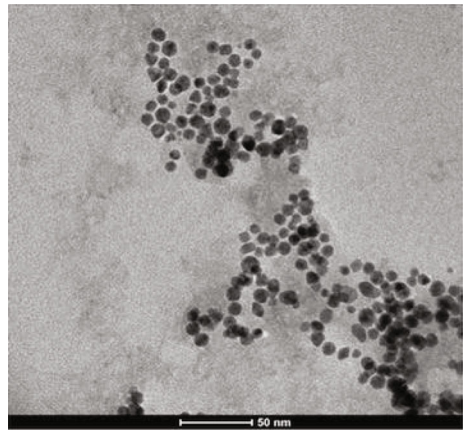

Figure 4: Transmission electron microscopy (TEM) image of silver nanoparticles in solution.

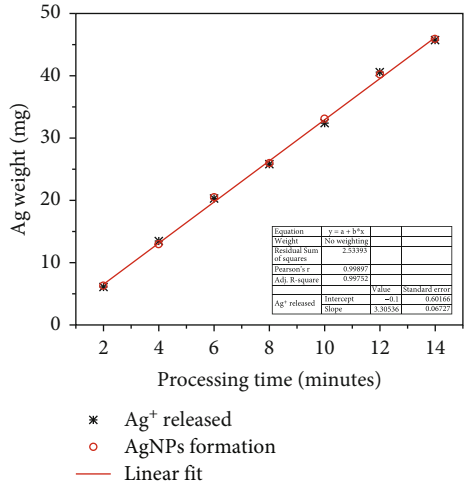

Figure 5: Ag^+ release and AgNP formation.

The measured weight decrease of the Ag electrode with the plasma processing time is shown in Figure 5. As estimated from this weight decrease, the Ag^+ release during

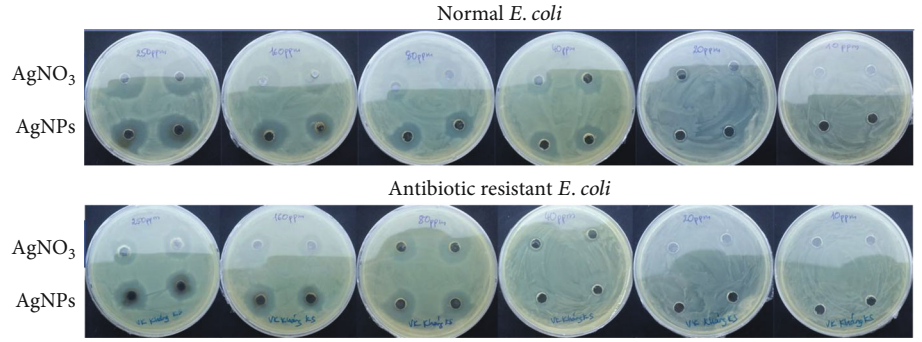

Figure 6: Comparison in the bactericidal properties of the AgNP solution produced by the plasma electrochemical technique and those of the $AgNO_3$ solution on normal and antibiotic-resistant *E. coli*.

the processing is about 3.3 mg/min. The nanoparticle formation rate estimated from the results of atomic absorption spectroscopy, thus, also gives the same rate which indicates a 100% nanoformation. In order to confirm this, ascorbic acid was introduced into the as-synthesized solutions. The UV–vis absorption spectra before and after the ascorbic acid introduction were found to remain identical. There should be no free Ag^+ in the plasma electrochemical AgNP solutions. Using the AgNP formation rate, the concentration of the AgNPs for a batch of 40 ml solution after 14 minutes processing could be estimated as 1150 ppm.

The observed results show that both the $AgNO_3$ solution and the AgNP solution are capable of killing the *E. coli*, even at low concentrations (20 ppm). However, with the antibiotic-resistant *E. coli*, a higher concentration (80 ppm) of the sterile ring is clearly observed. We can see that the inhibition zone created by the plasma electrochemical AgNPs is mostly larger than the inhibition one produced by the nanosilver obtained on the market with the same concentration. In particular, with the antibiotic-resistant bacteria, this difference is even more pronounced, demonstrating the outstanding bactericidal properties of the silver nanoparticles created by the plasma electrochemical method (Figure 6).

4. Conclusions

This work has demonstrated a low-cost green synthesis of colloidal AgNPs in a single process utilizing the plasma electrochemical method. Results have shown that the as-synthesized AgNPs are spherical in shape and homogeneous in size averaged with 9.7 nm diameter. The colloidal AgNP solutions show high antibacterial effectiveness against both normal and antibiotic-resistant bacteria. The advantages of the above described fabrication method have revealed to be a simple high yield preparation technique, which is very promising for the synthesis of colloidal AgNPs of with high homogeneity purity and antibacterial activity for different applications.

Data Availability

No data were used to support this study.

Conflicts of Interest

The authors declare that they have no conflicts of interest regarding the publication of this paper.

Acknowledgments

We acknowledge the support of The Physics Development Program of the Vietnam Academy of Science and Technology under the project grant number KHCBVL.02/18-19.

References

[1] L. Q. Kha, N. H. Chau, and H. T. Lua, "The Tendency of Nanotechnology Application in Plants and Aqueous Products Farming, Center of Science and Technology Information and Statistics, Department of Science and Technology of HCM City," in *Trends of application of nanotechnology in crop and aquaculture farming*, Center for Science and Technology Information and Statistics, Ho Chi Minh City Department of Science and Technology, 2016.

[2] H. C. Nguyen, T. T. Nguyen, T. H. Dao, Q. B. Ngo, H. L. Pham, and T. B. Nguyen, "Preparation of Ag/SiO2nanocomposite and assessment of its antifungal effect on soybean plant (a Vietnamese species DT-26)," *Advances in Natural Sciences: Nanoscience and Nanotechnology*, vol. 7, no. 4, article 045014, 2016.

[3] A. Hebeish, M. H. El-Rafie, M. A. El-Sheikh, A. A. Seleem, and M. E. El-Naggar, "Antimicrobial wound dressing and anti-inflammatory efficacy of silver nanoparticles," *International Journal of Biological Macromolecules*, vol. 65, pp. 509–515, 2014.

[4] D. Roe, B. Karandikar, N. Bonn-Savage, B. Gibbins, and J. B. Roullet, "Antimicrobial surface functionalization of plastic catheters by silver nanoparticles," *The Journal of Antimicrobial Chemotherapy*, vol. 61, no. 4, pp. 869–876, 2008.

[5] EPA, *EPA/600/R-10/081F*, U.S. Environmental Protection Agency, Washington, DC, 2012.

[6] Y. Echegoyen and C. Nerín, "Nanoparticle release from nano-silver antimicrobial food containers," *Food and Chemical Toxicology*, vol. 62, pp. 16–22, 2013.

[7] A. Kumar, P. K. Vemula, P. M. Ajayan, and G. John, "Silver-nanoparticle-embedded antimicrobial paints based on vegetable oil," *Nature Materials*, vol. 7, no. 3, pp. 236–241, 2008.

[8] F. Zhang, X. Wu, Y. Chen, and H. Lin, "Application of silver nanoparticles to cotton fabric as an antibacterial textile finish," *Fibers and Polymers*, vol. 10, no. 4, pp. 496–501, 2009.

[9] K.-H. Tseng, Y.-C. Chen, and J.-J. Shyue, "Continuous synthesis of colloidal silver nanoparticles by electrochemical discharge in aqueous solutions," *Journal of Nanoparticle Research*, vol. 13, no. 5, pp. 1865–1872, 2011.

[10] M. N. Nadagouda, T. F. Speth, and R. S. Varma, "Microwave-assisted green synthesis of silver nanostructures," *Accounts of Chemical Research*, vol. 44, no. 7, pp. 469–478, 2011.

[11] F. Mafuné, J. Y. Kohno, Y. Takeda, T. Kondow, and H. Sawabe, "Formation and size control of silver nanoparticles by laser ablation in aqueous solution," *The Journal of Physical Chemistry. B*, vol. 104, no. 39, pp. 9111–9117, 2000.

[12] C. Ortiz, R. Torres, and D. Paredes, "Synthesis, characterization, and evaluation of antibacterial effect of Ag nanoparticles against Escherichia coli O157:H7 and methicillin- resistant Staphylococcus aureus (MRSA)," *International Journal of Nanomedicine*, vol. 9, pp. 1717–1729, 2014.

[13] A. Panacek and L. Kvitek, "Silver colloid nanoparticles: synthesis, characterization, and their antibacterial activity," *The Journal of Physical Chemistry. B*, vol. 110, no. 33, pp. 16248–16253, 2006.

[14] J. L. López-Miranda, M. Vázquez, N. Fletes, R. Esparza, and G. Rosas, "Biosynthesis of silver nanoparticles using a Tamarix gallica leaf extract and their antibacterial activity," *Materials Letters*, vol. 176, pp. 285–289, 2016.

[15] S. Gurunathan, K. Kalishwaralal, R. Vaidyanathan et al., "Biosynthesis, purification and characterization of silver nanoparticles using Escherichia coli," *Colloids and Surfaces B: Biointerfaces*, vol. 74, no. 1, pp. 328–335, 2009.

[16] Q. H. Tran, V. Q. Nguyen, and A. T. Le, "Silver nanoparticles: synthesis, properties, toxicology, applications and perspectives," *Advances in Natural Sciences: Nanoscience and Nanotechnology*, vol. 4, no. 3, article 033001, 2013.

[17] H. Wang, X. Qiao, J. Chen, and S. Ding, "Preparation of silver nanoparticles by chemical reduction method," *Colloids and Surfaces A: Physicochemical and Engineering Aspects*, vol. 256, no. 2-3, pp. 111–115, 2005.

[18] M. G. M. Guzmán, J. Dille, and S. Godet, "Synthesis of silver nanoparticles by chemical reduction method and their antibacterial activity," *International Journal of Chemical and Biomolecular Engineering*, vol. 2, pp. 104–111, 2009.

[19] S. Ahmed, M. Ahmad, B. L. Swami, and S. Ikram, "A review on plants extract mediated synthesis of silver nanoparticles for antimicrobial applications: a green expertise," *Journal of Advanced Research*, vol. 7, no. 1, pp. 17–28, 2016.

[20] S. Jain and M. S. Mehata, "Medicinal plant leaf extract and pure flavonoid mediated green synthesis of silver nanoparticles and their enhanced antibacterial property," *Scientific Reports*, vol. 7, no. 1, p. 15867, 2017.

[21] V. S. Santosh, K. Kondeti, U. Gangal, S. Yatom, and P. J. Bruggeman, "Ag+reduction and silver nanoparticle synthesis at the plasma–liquid interface by an RF driven atmospheric pressure plasma jet: Mechanisms and the effect of surfactant," *Journal of Vacuum Science and Technology A*, vol. 35, no. 6, article 061302, 2017.

[22] N. M. Thuy, *Research on the Anaerobic Dissociation of the Anode to Generate Silver Nanoparticles Using High Voltage, [Ph.D. thesis]*, Vietnam Academy of Science and Technology, 2015.

Hindawi
Journal of Nanomaterials
Volume 2022, Article ID 6979280, 14 pages
https://doi.org/10.1155/2022/6979280

Research Article

Quantum Beat of Excitons in the Prolate Ellipsoidal Quantum Dots

Le Thi Ngoc Bao,[1] **Duong Dinh Phuoc**,[2] **Le Thi Dieu Hien**,[1,2] **and Dinh Nhu Thao**[2]

[1]*Hue University of Sciences, Hue University, 77 Nguyen Hue Street, Hue City, Vietnam*
[2]*Hue University of Education, Hue University, 34 Le Loi Street, Hue City, Vietnam*

Correspondence should be addressed to Le Thi Ngoc Bao; ltnbao@hueuni.edu.vn and Dinh Nhu Thao; dnthao@hueuni.edu.vn

Received 24 March 2022; Accepted 26 April 2022; Published 1 August 2022

Academic Editor: Nguyen Duc Cuong

In this paper, renormalized wavefunction method was applied to study quantum beats of excitons in the InGaAs/InAlAs prolate ellipsoidal quantum dots (QDs). The obtained results show that, without the pump laser, the exciton absorption intensity is just a smooth curve. In contrast, when the system is illuminated by a strong pump laser resonating with two exciton levels, the oscillation behavior of exciton absorption intensity, which is known as quantum beats of excitons, is observed. That result can be interpreted as an indirect consequence of the Pauli exclusion principle leading to a splitting of the electron levels, which forms two close exciton levels, and if two excitons are excited coherently, the interference of these two excitons will finally form a quantum beat. The study also shows that the geometry shape of the QDs has strong influence on the properties of quantum beats. Changing the period of quantum beats in particular or optical properties in general in QDs thus becomes more flexible through changing their geometry shapes. This is one interested advantage of the ellipsoidal QDs and is expected to increase their applicability more than the spherical QDs.

1. Introduction

Presently, low-dimensional semiconductors attract the attention of several researchers, thanks to their high applicability. In low-dimensional semiconductor systems, particles are confined in one dimension-quantum wells, two dimensions-quantum wires, and three dimensions-quantum dots (QDs). It is this quantum confinement that makes low-dimensional semiconductor systems, especially QDs, offer many effects with considerable potential in the manufacture of new optical devices [1]; in electronic and optoelectronic applications [2, 3]; for quantum-functional and memory devices [4, 5]; and many other research fields such as quantum computing, photovoltaics, infrared photodetectors, medical imaging, and biosensors [6–12].

Recent studies on coupled optical properties in QDs with simple shapes, such as cubic, cylindrical, and spherical QDs have been carried out [13–16]. These works show that optical properties of QDs depend to a great extent on external fields and the size of QDs. Especially, the shape of QDs also makes a notable difference to their optical properties [17, 18]. This suggests that specially shaped QDs like ellipsoidal ones can possess interestingly different optical properties. In ellipsoidal QDs, the quantized energy levels of particles are highly dependent on structural parameters [19–23]. Therefore, the optical properties in these quantum dot structures are said to be easily modifiable by these structural parameters.

Thanks to its high applicability, especially in manufacture of quantum computer, quantum beat in low-dimensional structures has attracted much attention. Using ultrashort laser pulses with various experiments [24–30], scientists have observed quantum beats of excitons in different semiconductor structures. Theoretically, scientists have applied many methods to study the quantum beats of excitons in quantum structures [25, 31–36], of which the most convenient is the renormalized wavefunction method [32, 35, 36].

In this paper, we used the renormalized wavefunction method to study the existence of quantum beats of excitons in $In_{0.53}Ga_{0.47}As/In_{0.52}Al_{0.48}As$ prolate ellipsoidal

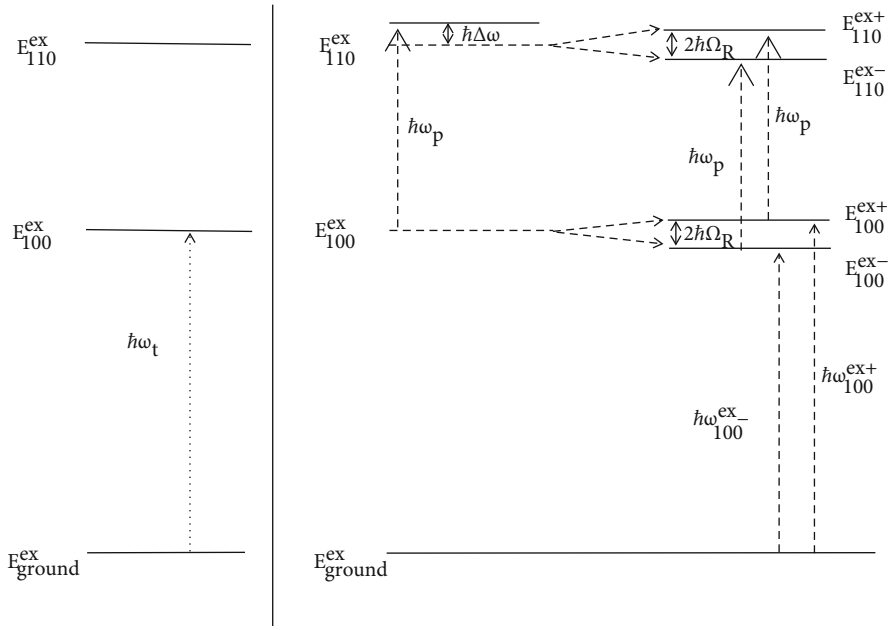

Figure 1: A three-level energy diagram and exciton transitions: (a) without the pump laser, the system contains three levels of exciton: the ground level E^{ex}_{ground} and two excited ones E^{ex}_{100}, E^{ex}_{110}. The probe laser $\hbar\omega_t$ only identifies the transition for the pair of levels $(E^{ex}_{\text{ground}}, E^{ex}_{100})$ (marked by a dotted arrow); (b) under the effect of the resonant strong pump laser coupling to the initial excited levels of exciton, E^{ex}_{100} is split into E^{ex-}_{100} and E^{ex+}_{100}; E^{ex}_{110} is separated to E^{ex-}_{110} and E^{ex+}_{110}. The probe laser $\hbar\omega_t$ identifies two transitions for two pairs of levels $(E^{ex}_{\text{ground}}, E^{ex-}_{100})$ and $(E^{ex}_{\text{ground}}, E^{ex+}_{100})$, obeying the selection rules for interband transitions (marked by thin dashed arrows).

quantum dots. We chose these heterostructures because they have the large conduction-band discontinuity between $In_{0.53}Ga_{0.47}As/In_{0.52}Al_{0.48}As$ layers that is $\Delta E_c = 500$ meV [37]. This can be approximated as the infinite confinement potential for electrons in these quantum structures, which is consistent with our hypothesis. Besides, these heterostructures have many applications [37], as well as create modern infrared devices [38, 39]. This article focuses on investigating the dependence of the exciton absorption intensity on the external fields, sizes, and shapes of quantum dot. The article includes the following main sections: Section 2 is about the model and theory, Section 3 provides the main results and discussion, and Section 4 presents the conclusions.

2. Model and Theory

2.1. Wavefunctions and Energy Levels of Exciton

2.1.1. The Case without the Pump Laser. In this case, we investigate quantum beats of excitons in prolate ellipsoidal QDs. We use a three-level diagram of exciton, including one ground level E^{ex}_{ground} and two excited ones of exciton E^{ex}_{100} and E^{ex}_{110} (Figure 1). These exciton levels are originated from interband transitions between the lowest level of hole E^{h}_{100} and the two lowest ones of electron E^{e}_{100} and E^{e}_{110} in QDs (see Figure 10(a) in Appendix A). For simplicity, we assume the prolate ellipsoidal QDs lied in an infinite potential (see Appendix A).

First, we find the stationary wavefunctions of the exciton and the corresponding energy levels in the absence of the pump laser. The wavefunctions of the exciton in the stationary states, in a strong confinement regime, are the combination of the one-particle total wavefunctions of the electron and the hole (see Equation (A.15)).

$$\begin{cases} \Lambda^{ex}_{100}\left(\vec{r}\right) = \Lambda^{e}_{100}\left(\vec{r}\right).\Lambda^{h}_{100}\left(\vec{r}\right), \\ \Lambda^{ex}_{110}\left(\vec{r}\right) = \Lambda^{e}_{110}\left(\vec{r}\right).\Lambda^{h}_{100}\left(\vec{r}\right). \end{cases} \tag{1}$$

The corresponding exciton energy levels are determined by the sum of the quantized levels of electrons E^{e}_{nlm} and holes E^{h}_{nlm} (see Equation (A.16) and Equation (A.17) in Appendix A), minus the exciton binding energy E_{binding}

$$\begin{cases} E^{ex}_{100} = E^{e}_{100} + E^{h}_{100} - E_{\text{binding}}, \\ E^{ex}_{110} = E^{e}_{110} + E^{h}_{100} - E_{\text{binding}}, \end{cases} \tag{2}$$

where E_{binding} is usually considerable smaller than the energy levels of electrons and holes. To investigate the characteristics of quantum beats with time, we utilize the time-dependent stationary wavefunctions given in the form

$$\begin{cases} \Lambda^{ex}_{100}\left(\vec{r}, t\right) = \Lambda^{ex}_{100}\left(\vec{r}\right)e^{-i/\hbar E^{ex}_{100}t}, \\ \Lambda^{ex}_{110}\left(\vec{r}, t\right) = \Lambda^{ex}_{110}\left(\vec{r}\right)e^{-i/\hbar E^{ex}_{110}t}. \end{cases} \tag{3}$$

2.1.2. The Case with the Pump Laser. In this case, we examine a system subjected to a pump laser resonating with

two exciton excited levels in the initial stationary states E^{ex}_{100} and E^{ex}_{110}. Under the effect of the pump laser, the excitons are now no longer in the initial stationary states but in the nonstationary state which is described by the product of the wavefunctions of the electron in the mixed state $\Lambda^{e}_{\text{mix}}(\vec{r},t)$ (Equation (A.26)) and the initial wavefunction of hole $\Lambda^{h}_{100}(\vec{r},t)$ (see Equation (A.18))

$$\Lambda^{ex}_{\text{mix}}\left(\vec{r},t\right)=\Lambda^{e}_{\text{mix}}\left(\vec{r},t\right).\Lambda^{h}_{100}\left(\vec{r},t\right), \tag{4}$$

The wavefunction in Equation (4) can be written in the explicit form

$$\begin{aligned}\Lambda^{ex}_{\text{mix}}\left(\vec{r},t\right)=&\frac{1}{2\Omega_R}\left(\alpha_1 e^{i\alpha_2 t}+\alpha_2 e^{-i\alpha_1 t}\right)e^{-i/\hbar E^{ex}_{100}t}\Lambda^{ex}_{100}\left(\vec{r}\right)\\&-\frac{V_{21}}{2\Omega_R\hbar}\left(e^{i\alpha_1 t}-e^{-i\alpha_2 t}\right)e^{-i/\hbar E^{ex}_{110}t}\Lambda^{ex}_{110}\left(\vec{r}\right),\end{aligned} \tag{5}$$

or it can be rewritten as

$$\begin{aligned}\Lambda^{ex}_{\text{mix}}\left(\vec{r},t\right)=&\frac{1}{2\Omega_R}\left(\alpha_1 e^{-i/\hbar E^{ex-}_{100}t}+\alpha_2 e^{-i/\hbar E^{ex+}_{100}t}\right)\Lambda^{ex}_{100}\left(\vec{r}\right)\\&-\frac{V_{21}}{2\hbar\Omega_R}\left(e^{-i/\hbar E^{ex-}_{110}t}-e^{-i/\hbar E^{ex+}_{110}t}\right)\Lambda^{ex}_{110}\left(\vec{r}\right),\end{aligned} \tag{6}$$

in which

$$\begin{cases}E^{ex+}_{100}=E^{ex}_{100}+\hbar\alpha_1,\\E^{ex-}_{100}=E^{ex}_{100}-\hbar\alpha_2,\end{cases} \tag{7}$$

and

$$\begin{cases}E^{ex+}_{110}=E^{ex}_{110}+\hbar\alpha_2,\\E^{ex-}_{110}=E^{ex}_{110}-\hbar\alpha_1,\end{cases} \tag{8}$$

and $\Lambda^{ex}_{100}(\vec{r})$ and $\Lambda^{ex}_{110}(\vec{r})$ are the stationary exciton wavefunctions when the pump laser does not turn on (Equation (1)). Equation (8) can be written as

$$\begin{cases}E^{ex+}_{110}=E^{ex+}_{100}+\hbar\omega_p,\\E^{ex-}_{110}=E^{ex-}_{100}+\hbar\omega_p.\end{cases} \tag{9}$$

From Equations (7) and (8), we have

$$\begin{cases}E^{ex+}_{100}-E^{ex-}_{100}=2\hbar\Omega_R,\\E^{ex+}_{110}-E^{ex-}_{110}=2\hbar\Omega_R.\end{cases} \tag{10}$$

Under the effect of the pump laser, the two initial excited levels of exciton split into four new energy levels in which two levels E^{ex-}_{100} and E^{ex+}_{100} are separated from level E^{ex}_{100}, and two levels E^{ex-}_{110} and E^{ex+}_{110} are separated from level E^{ex}_{110} (see Figure 1(b)). We see that the energy difference between two splitting levels E^{ex-}_{100} and E^{ex+}_{100} or between two splitting ones E^{ex-}_{110} and E^{ex+}_{110} is equal to $2\hbar\Omega_R$ (Equation (10)), which is much smaller than the photon energy of the pump laser $\hbar\omega_p$. This photon energy is also the energy distance between two pairs of levels $(E^{ex-}_{100},E^{ex+}_{100})$ and $(E^{ex-}_{110},E^{ex+}_{110})$ (Equation (9)). The Rabi frequency Ω_R is proportional to the detuning of the pump laser as well as the transition matrix element for the intersubband transition and has the following form

$$\Omega_R=\sqrt{\left(\frac{\Delta\omega}{2}\right)^2+\frac{|V_{21}|^2}{\hbar^2}}, \tag{11}$$

where $\hbar\Delta\omega$ is the detuning of the pump laser with two levels of electron E^{e}_{100} and E^{e}_{110}, and V_{21} is the matrix element for the intersubband transition between electron levels (see Equation (A.25) in Appendix A).

2.2. Absorption Intensity of Excitons

2.2.1. The Case without the Pump Laser. The existence of the quantum beats of excitons is determined through the oscillatory behavior of the absorption intensity of excitons. On the other hand, the absorption intensity is a function of the transition matrix element among the levels of exciton. Therefore, we need to compute the dipole transition matrix element among the states of exciton, first among levels of exciton in the stationary states (Figure 1(a)). Since there are two excited states of exciton in the system, when the system is illuminated by a probe laser, we would expect to obtain two transitions of exciton from the ground state $|0\rangle$ corresponding to level E^{ex}_{ground} to two initial excited states of exciton corresponding to two exciton levels E^{ex}_{100} and E^{ex}_{110}. However, according to the selection rule for the interband transition in QDs, only the exciton transition from the ground level E^{ex}_{ground} to the lowest excited level of exciton E^{ex}_{100} exists as described by the dotted arrow in Figure 1(a). Thus, in the absence of the effect of the pump laser, the permitted transition matrix element between levels E^{ex}_{ground} and E^{ex}_{100} under the action of a probe laser has the form

$$\begin{aligned}T^{ex}_{100}&=\left\langle\Lambda^{ex}_{100}\left(\vec{r},t\right)\left|\hat{H}_{\text{int}}\right|0\right\rangle\\&=-\frac{eA_t e^{-i\omega_t t}}{m_0 i\omega_t}\left\langle\Lambda^{ex}_{100}\left(\vec{r},t\right)\left|\vec{n}.\hat{\vec{p}}\right|0\right\rangle,\end{aligned} \tag{12}$$

where A_t and ω_t are, respectively, the amplitude and the frequency of the probe laser. Replace Equations (3) and (1) into Equation (12); we have

$$T^{ex}_{100}=-\frac{eA_t p_{cv}}{m_0 i\omega_t}e^{i/\hbar\left(E^{e}_{100}+E^{h}_{100}-\hbar\omega_t\right)t}\left\langle\Psi^{e}_{100}\left(\vec{r}\right)\Psi^{h}_{100}\left(\vec{r}\right)|0\right\rangle,, \tag{13}$$

where p_{cv} is the polarization matrix element between conduction and valence bands

$$p_{cv}=\left\langle u_c\left|\vec{n}.\hat{\vec{p}}\right|u_v\right\rangle. \tag{14}$$

From that, we find the expression for the exciton absorption intensity when the pump laser does not turn on as

$$I_{100}^{ex}(t) \propto |T_{100}^{ex}|^2 = \left(\frac{eA_t p_{cv}}{m_0 \omega_t}\right)^2. \tag{15}$$

Because the exciton lifetime on the excited levels is finite, the excited states of exciton will fade over time. To account for the decay of $I_{100}^{ex}(t)$, we phenomenologically provide a decay parameter $\gamma = 1/T_1$ in Equation (15). From that, we obtain the expression of the absorption intensity of excitons in the absence of the pump laser as follows

$$I_{100}^{ex}(t) \propto \left(\frac{eA_t p_{cv}}{m_0 \omega_t}\right)^2 \exp(-\gamma t), \tag{16}$$

where T_1 is the lifetime of exciton on the energy level E_{100}^{ex}.

2.2.2. The Case with the Pump Laser. From Section 2.1.2, we see that exciton will stay in the nonstationary state $\Lambda_{\text{mix}}^{ex}(\vec{r}, t)$ when QDs are irradiated by a strong pump laser resonant with two initial exciton levels E_{100}^{ex} and E_{110}^{ex}. Now, to find the absorption intensity of excitons, we need to calculate the dipole transition matrix element between the ground state $|0\rangle$ and the nonstationary exciton one $\Lambda_{\text{mix}}^{ex}(\vec{r}, t)$. The matrix element in this case has the form

$$\begin{aligned} T_{\text{mix}}^{ex} &= \left\langle \Lambda_{\text{mix}}^{ex}\left(\vec{r}, t\right) \middle| \hat{\text{H}}_{\text{int}} \middle| 0 \right\rangle \\ &= -\frac{eA_t e^{-i\omega_t t}}{m_0 i \omega_t} \left\langle \Lambda_{\text{mix}}^{ex}\left(\vec{r}, t\right) \middle| \vec{n}.\widehat{\vec{p}} \middle| 0 \right\rangle. \end{aligned} \tag{17}$$

Combining Equations (6) and (17), we get the following matrix element

$$\begin{aligned} T_{\text{mix}}^{ex} = -\frac{eA_t e^{-i\omega_t t}}{m_0 i \omega_t} &\left[\frac{1}{2\Omega_R}\left(\alpha_1 e^{-i/\hbar E_{100}^{ex-} t} + \alpha_2 e^{-i/\hbar E_{100}^{ex+} t}\right)^* \right. \\ &\times \left\langle \Lambda_{100}^{ex}\left(\vec{r}\right) \middle| \vec{n}.\widehat{\vec{p}} \middle| 0 \right\rangle - \frac{V_{21}^*}{2\Omega_R \hbar}\left(e^{-i/\hbar E_{110}^{ex-} t} - e^{-i/\hbar E_{110}^{ex+} t}\right)^* \\ &\left. \times \left\langle \Lambda_{110}^{ex}\left(\vec{r}\right) \middle| \vec{n}.\widehat{\vec{p}} \middle| 0 \right\rangle \right]. \end{aligned} \tag{18}$$

Because of the selection rule for the interband transition in QDs, there are only the dipole transitions from the ground state to the pair of the lowest splitting levels of exciton $(E_{100}^{ex-}, E_{100}^{ex+})$ that are split from the initial exciton level E_{100}^{ex}. So, we have

$$\begin{aligned} T_{\text{mix}}^{ex} = -\frac{eA_t e^{-i\omega_t t}}{m_0 i \omega_t} &\left[\frac{1}{2\Omega_R}\left(\alpha_1 e^{-i/\hbar E_{100}^{ex-} t} + \alpha_2 e^{-i/\hbar E_{100}^{ex+} t}\right)^* \right. \\ &\left. \times \left\langle \Lambda_{100}^{ex}\left(\vec{r}\right) \middle| \vec{n}.\widehat{\vec{p}} \middle| 0 \right\rangle \right], \end{aligned} \tag{19}$$

or

$$\begin{aligned} T_{\text{mix}}^{ex} = -\frac{eA_t e^{-i\omega_t t}}{m_0 i \omega_t} &\left[\frac{1}{2\Omega_R}\left(\alpha_1 e^{-i/\hbar E_{100}^{ex-} t} + \alpha_2 e^{-i/\hbar E_{100}^{ex+} t}\right)^* \right] \\ &\times \left\langle \Lambda_{100}^{e}\left(\vec{r}\right) \Lambda_{100}^{h}\left(\vec{r}\right) \middle| \vec{n}.\widehat{\vec{p}} \middle| 0 \right\rangle. \end{aligned} \tag{20}$$

Equation (20) clearly shows that, after the effect of a strong pump laser resonating with two exciton excited levels in stationary state E_{100}^{ex} and E_{110}^{ex}, then in the system, there are two optical transitions from the ground state E_{ground}^{ex} to two lowest splitting level of exciton E_{100}^{ex-} and E_{100}^{ex+} (illustrated by two thin dashed arrows in Figure 1(b)). Combining Equation (A.15) into Equation (20), we get the matrix element for the dipole transition between the ground level $|0\rangle$ and the nonstationary exciton one $\Lambda_{\text{mix}}^{ex}(\vec{r}, t)$ as follows:

$$\begin{aligned} T_{\text{mix}}^{ex} = -\frac{eA_t e^{-i\omega_t t} p_{cv}}{m_0 i \omega_t} &\left[\frac{1}{2\Omega_R}\left(\alpha_1 e^{-i/\hbar E_{100}^{ex-} t} + \alpha_2 e^{-i/\hbar E_{100}^{ex+} t}\right)^* \right] \\ &\times \left\langle \Psi_{100}^{e}\left(\vec{r}\right) \Psi_{100}^{h}\left(\vec{r}\right) \middle| 0 \right\rangle, \end{aligned} \tag{21}$$

or

$$T_{\text{mix}}^{ex} = -\frac{eA_t e^{-i\omega_t t} p_{cv}}{m_0 i \omega_t}\left[\frac{1}{2\Omega_R}\left(\alpha_1 e^{-i/\hbar E_{100}^{ex-} t} + \alpha_2 e^{-i/\hbar E_{100}^{ex+} t}\right)^*\right]. \tag{22}$$

Next, we investigate the time-resolved intensity of absorption under the effect of the resonant pump laser $I_{\text{mix}}^{ex}(t)$. From Equation (10), we see that the probe laser needs a spectral width larger than $2\hbar\Omega_R$, which is energy separation between two levels E_{100}^{ex-} and E_{100}^{ex+}, in order to excite coherently two excitons in the pair $(E_{100}^{ex-}, E_{100}^{ex+})$. In order to fully observe at least a quantum beat oscillation, the period of the quantum beat needs to be less than or equal to coherence time T_2, the time it takes for two excitons in the pair $(E_{100}^{ex-}, E_{100}^{ex+})$ to oscillate in phase. Of course, the coherence time T_2 is always less than or equal to the lifetime T_1 of exciton in the state $\Lambda_{100}^{ex}(\vec{r}, t)$ (Equation (3)). Therefore, at any given time $t < T_2$, the absorption intensity of excitons under the effect of the pump laser has the following form.

$$\begin{aligned} I_{\text{mix}}^{ex}(t) &\propto |T_{\text{mix}}^{ex}|^2 \\ &= \left(\frac{eA_t p_{cv}}{m_0 \omega_t}\right)^2 \left|\frac{1}{2\Omega_R}\left(\alpha_1 e^{-i/\hbar E_{100}^{ex-} t} + \alpha_2 e^{-i/\hbar E_{100}^{ex+} t}\right)^*\right|^2, \end{aligned} \tag{23}$$

or

$$\begin{aligned} I_{\text{mix}}^{ex}(t) \propto \left(\frac{eA_t p_{cv}}{m_0 \omega_t}\right)^2 &\left[\left(\frac{\alpha_1}{2\Omega_R}\right)^2 + \left(\frac{\alpha_2}{2\Omega_R}\right)^2 \right. \\ &\left. + 2\frac{\alpha_1}{2\Omega_R}\frac{\alpha_2}{2\Omega_R}\cos\left(\frac{E_{100}^{ex+} - E_{100}^{ex-}}{\hbar}\right)t\right]. \end{aligned} \tag{24}$$

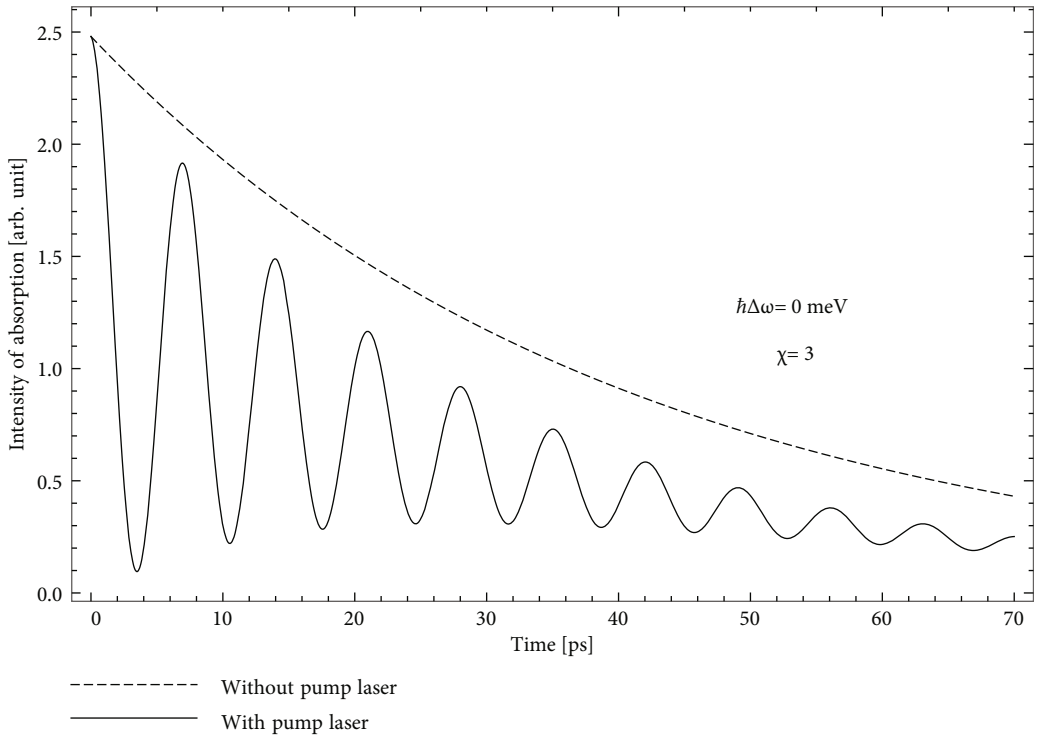

FIGURE 2: The time-dependent absorption intensity in prolate ellipsoidal QDs of the ellipsoid aspect ratio $\chi = 3$ (in consistent with the length of the semi-major axis $c = 75$ Å, satisfying the condition $2c < a_B^{ex}$) in two cases: in the absence (dashed line) and in the presence of the pump laser (solid lines) with the detuning $\hbar\Delta\omega = 0$ meV.

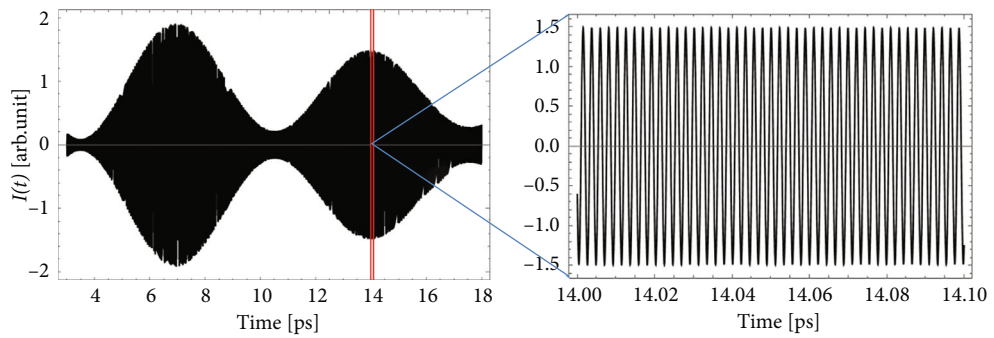

FIGURE 3: (a) The dependence of the total absorption intensity on time in the case of the ellipsoid aspect ratio $\chi = 3$. (b) An enlarged version of the curve limited by red lines.

We put

$$\begin{cases} \beta_1 = \dfrac{\alpha_1}{2\Omega_R}, \\ \beta_2 = \dfrac{\alpha_2}{2\Omega_R}, \end{cases} \tag{25}$$

and combined with Equation (10), we can rewrite the expression for the absorption intensity of excitons as

$$I_{\text{mix}}^{ex}(t) \propto \left(\frac{eA_t p_{cv}}{m_0 \omega_t}\right)^2 \left[\beta_1^2 + \beta_2^2 + 2\beta_1\beta_2 \cos\left(2\Omega_R t\right)\right]. \tag{26}$$

As mentioned in Section 2.2.1, in fact, the exciton lifetime on the excited states is finite, so the oscillation in Equation (6) decays with time. To account for damping in $I_{mix}^{ex}(t)$, we add phenomenologically the damped factors $\gamma = 1/T_1$ and $\tau = 1/T_2$ in Equation (26). From this, we obtain the final expression of the absorption intensity of excitons in the presence of the resonant pump laser as follows

$$I_{\text{mix}}^{ex}(t) \propto \left(\frac{eA_t p_{cv}}{m_0 \omega_t}\right)^2 \left[\left(\beta_1^2 + \beta_2^2\right) \exp\left(-\gamma t\right) + 2\beta_1\beta_2 \exp\left(-\tau t\right) \cos\left(2\Omega_R t\right)\right], \tag{27}$$

where T_2 is the coherent time of the state described in Equation (6).

Equation (27) shows that in the case QDs are illuminated by a probe laser in the presence of a resonant strong pump laser, the absorption intensity has the form of a

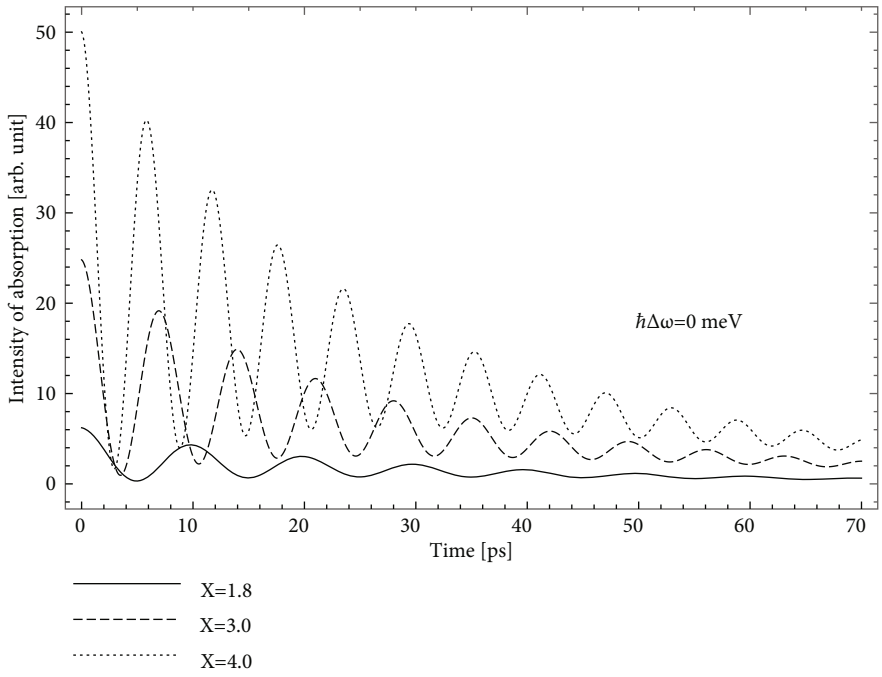

FIGURE 4: The time dependence of the absorption intensity in the prolate ellipsoidal quantum dot with different values χ: $\chi = 1.8$ (corresponding to $c = 45$ Å) is denoted by solid line, $\chi = 3$ (corresponding to $c = 75$ Å) is denoted by dashed line, and $\chi = 4$ (corresponding to $c = 100$ Å) is denoted by dotted line in the case of the effect of the pump laser with the detuning $\hbar\Delta\omega = 0$ meV.

damped periodic oscillation that owns a frequency of twice the Rabi frequency of the electron $2\Omega_R$. This oscillation indicates the existence of the quantum beats of excitons in the quantum dot structure, which we will examine and explain in detail in the next section.

As we know, when there are two oscillations of similar frequencies in the system, they will interfere with each other to form a superposition wave of the frequency that is the average of two initial frequencies (i.e., exciton ones ω_{ex}^{+} and ω_{ex}^{-}) and its amplitude oscillates with the frequency equal to one half of the difference of two initial frequencies. Thence, the beat frequency is equal to the difference of two initial frequencies. Hence, from Equation (24) or Equation (27), we can formally deduce the expression of the total absorption intensity that oscillates with the effective frequency that equal to the sum of the two initial frequencies and have the following form

$$I(t) \propto \left(\frac{eA_t p_{cv}}{m_0 \omega_t}\right)^2 \left[\left(\beta_1^2 + \beta_2^2\right) \exp\left(-\gamma t\right) + 2\beta_1\beta_2 \exp\left(-\tau t\right) \cos\left(\frac{E_{100}^{ex+} - E_{100}^{ex-}}{\hbar}\right) t\right] \cdot \cos\left(\frac{E_{100}^{ex+} + E_{100}^{ex-}}{\hbar}\right) t. \quad (28)$$

We can rewrite Equation (28) as follows

$$I(t) \propto I_{\text{mix}}^{ex}(t) \cdot \cos\left(\frac{E_{100}^{ex+} + E_{100}^{ex-}}{\hbar}\right) t. \quad (29)$$

3. Results and Discussion

To further study and demonstrate the obtained results, in this part, we perform numerical calculations for the time-resolved intensity of absorption in $In_{0.53}Ga_{0.47}As/In_{0.52}Al_{0.48}As$ prolate ellipsoidal QDs. We utilize those parameters for the calculation: the effective mass of the electron and the hole in the dot material $In_{0.53}Ga_{0.47}As$ is $m_e = 0.042m_0$ and $m_h = 0.052m_0$; the bandgap of the dot material is $E_g = 750$ meV [37, 40]; the linewidth and the amplitude of pump laser are $\Gamma = 0.1$ meV and $A_p = 4 \times 10^4$ V/cm, respectively; the lifetime of excitons is chosen as $T_1 = 40$ ps; and the coherent time T_2 is assumed to be less than the lifetime T_1 as discussed above and is chosen as $T_2 = 20$ ps.

In order to clearly study the properties of the quantum beat before the decoherence of excitons happens, laser pulses must have the pulse duration less than the decoherence time of excitons. In addition, the paper studies the prolate ellipsoidal QDs, which is a quantum structure so the major axis $2c$ and the minor axis $2a$ must have the length smaller than the bulk exciton Bohr radius in the dot material $In_{0.53}Ga_{0.47}As$, which has a value $a_B^{ex} \simeq 308$ Å. Therefore, in order to calculate, we have chosen the length of the semi-minor axis to be $a = 25$ Å; and the length of the semi-major axis will vary depending on the ellipsoid aspect ratio χ ($c = \chi \cdot a$).

First, we plot the dependence of the absorption intensity on time when the value of the ellipsoid aspect ratio of QDs is $\chi = 3$ in two cases without and with the effect of the pump laser (Figure 2). From the figure, we realize that, without the pump laser, the absorption intensity of excitons is just

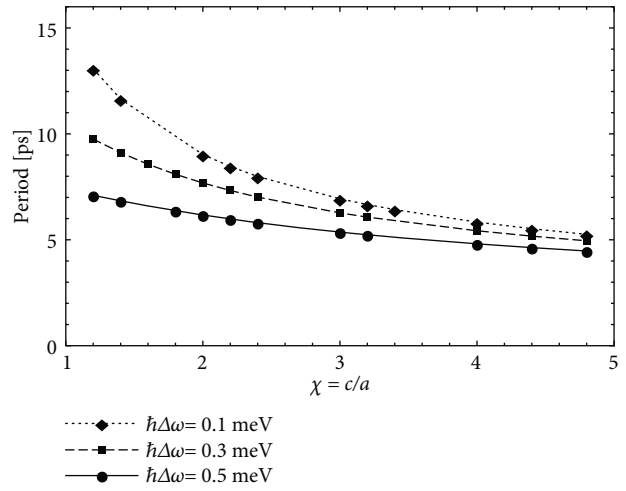

Figure 5: The period of quantum beat versus the ellipsoid aspect ratio χ with various detuning values: $\hbar\Delta\omega = 0.1$ meV (dotted line), $\hbar\Delta\omega = 0.3$ meV (dashed line), and $\hbar\Delta\omega = 0.5$ meV (solid line).

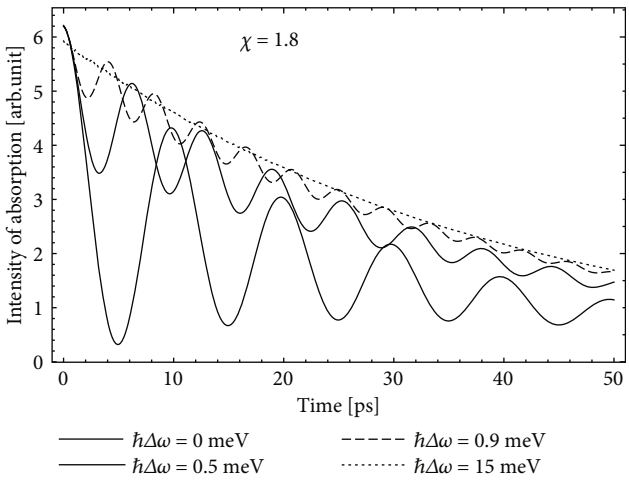

Figure 6: The time dependence of the absorption intensity in the prolate ellipsoidal quantum dot in the case of the ellipsoid aspect ratio χ =1.8 with various detuning values: $\hbar\Delta\omega = 0$ meV (thick solid line), $\hbar\Delta\omega = 0.5$ meV (thin solid line), $\hbar\Delta\omega = 0.9$ meV (dashed line), and $\hbar\Delta\omega = 15$ meV (dotted line).

a smooth curve gradually going to zero in time (dashed line), that is, there is no quantum beat of excitons. However, if we irradiate a resonant strong pump laser to connect two initial exciton levels ($\hbar\Delta\omega = 0$meV), we find the absorption intensity oscillating with the constant frequency, which is equal to twice the electron Rabi frequency $2\Omega_R$, and fading over time (the solid line). This is the quantum beat of excitons in prolate ellipsoidal QDs, like the similar to quantum beat of excitons obtained in the previously studied spherical quantum dot, quantum well, and quantum wire structures [35, 36, 41]. We find that the results obtained in prolate ellipsoidal QDs are similar to ones of spherical QDs [35], it is explained as both spherical and prolate ellipsoidal QDs belong to quasi-zero-dimensional systems.

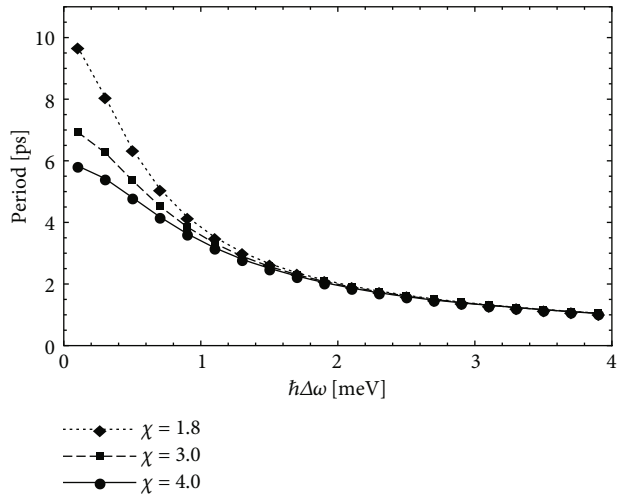

Figure 7: The period of quantum beat versus the laser detuning for various χ values: $\chi = 1.8$ (dotted line), $\chi = 3$ (dashed line), and $\chi = 4$ (solid line).

The existence of the quantum beat can be interpreted as follows. Initially, when the system is not irradiated by the pump laser, in the system, there existed two electron quantization energy levels, and according to the Pauli exclusion principle, these energy levels existed four permitted states of electron. Afterward, if the system is subjected to a strong pump laser resonant with two electron-quantized levels, those levels couple to each other and form a unique level. That new one, to obey the Pauli exclusion principle, allows only two electron states while the system needs four ones, leading to the lack of allowed electron states. To have enough number of the allowed states, each initial electron level must separate into two splitting levels as illustrated in Figure 1(b). Consequently, under the influence of the probe laser, in the absorption spectrum, we observed two interband transitions between the hole level and two splitting levels of electron (marked by thin dashed arrows in Figure 1(b)). Those transitions result in two closely spaced exciton levels, similar to the results obtained before in other quantum structures [16, 18]. Since these two exciton levels have roughly the same frequency, when they oscillate in phase, they will interfere with each other to form a quantum beat [35, 36], as showed in Figure 3 below.

Starting from Equation (28), we plot the total absorption intensity with the effective frequency that equal to the sum of the two exciton frequencies ω_{ex}^{+} and ω_{ex}^{-} as shown in Figure 3. Here, we add the absorption intensity of quantum beat to the total absorption intensity as described by Equation (29). In addition, the absorption intensity of quantum beat changes with time and oscillates with the frequency being twice the electron Rabi frequency, as described by the solid lines ὁ Figure 2.

Next, to find out the characteristics of the quantum beat of excitons, we examine the dependence of the absorption intensity of excitons on the ellipsoid aspect ratio. Figure 4 shows the dependence of the absorption intensity over time for different values of the ellipsoid aspect ratio χ. In all three cases, we observe a damped oscillation of the absorption

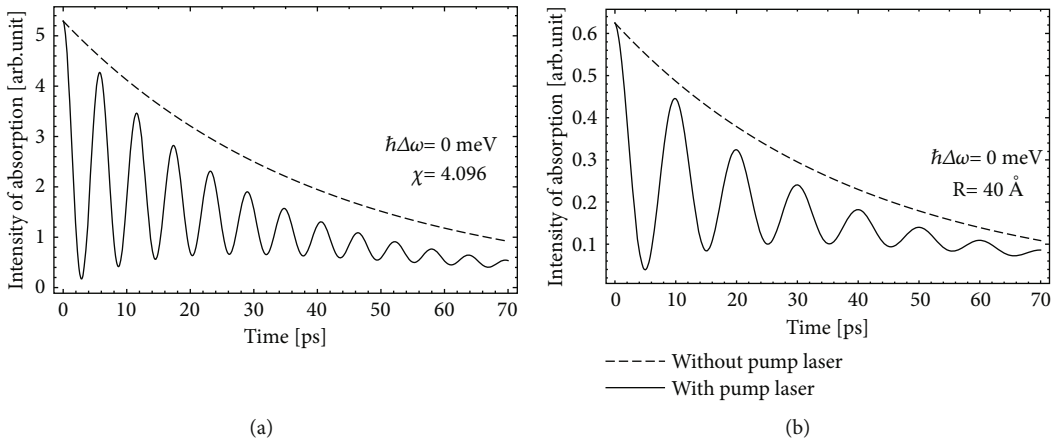

Figure 8: The dependence of the absorption intensity of excitons over time: (a) in the prolate ellipsoidal QD with the length of the semi-minor axis $a = 25$ Å, $\chi = 4.096$ (in consistent with the length of the semi-major axis $c = 102.4$ Å) and (b) in the spherical QD with radius $R = 40$ Å of the same volume.

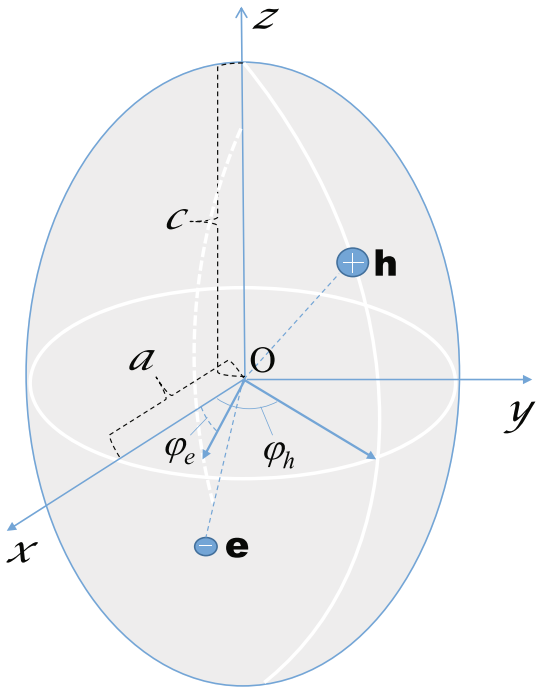

Figure 9: Electron-hole pair in a prolate ellipsoidal QD.

intensity, confirming the existence of the quantum beat of excitons. Besides, investigation shows that the oscillation of the absorption intensity strongly depends on the ellipsoid aspect ratio χ. As the value of the ellipsoid aspect ratio χ increases, so does the amplitude and frequency of the oscillation. This means that as the value χ increases, the stronger quantum beat phenomenon appears, and the greater oscillation frequency is. This can be explained as follows.

According to Equation (A.16) and Equations (A.6), (A.8), and (A.11), electron quantization energy levels E^e_{100} and E^e_{110} are inversely proportional to the ellipsoid aspect ratio χ. Therefore, when we increase the value of the ellipsoid aspect ratio χ, then the separation between the two electron levels becomes smaller or, in other words, the electron energy levels shift closer, that is, the transition probability between these two levels will increase (or V_{21} increases). Therefore, when a resonant pump laser is turned on, each initial electron level must immediately split into two new levels in order to comply with the Pauli exclusion principle. Then, if we irradiate a suitable probe laser into the system, we will see the transitions from the hole energy level to these new energy levels of the electron. As a result, excitons are rapidly generated, and since they are at roughly equal levels, a quantum beat of excitons is quickly formed. Otherwise, according to the quantum size effects, we have ω_t being a decreasing function of χ, and from Equation (27), we again have the beat amplitude inversely proportional with frequency of the probe photon ω_t. Therefore, as the ellipsoid aspect ratio χ increases, so does the beat amplitude. In brief, the more we increase the value of χ, the closer the initial energy levels of the electron are to each other and the easier it is for the corresponding states to couple to each other. Consequently, the more likely the splitting of the electron levels is to occur, and the more rapidly the quantum beat of excitons forms, the higher the amplitude of quantum beat as a result. Besides, according to Equation (11), the electron Rabi frequency is proportional to the transition matrix element V_{21}. Also, as mentioned above, as we increase the value of χ, the transition probability between two electron quantized levels increases (or V_{21} increases). As a result, when we increase the value of χ, the electron Rabi frequency increases, so the oscillatory frequency of quantum beat also increases because the oscillatory frequency of beat is twice the electron Rabi frequency.

To study more clearly the feature of the quantum beat period, in Figure 5, we plot the quantum beat period versus the ellipsoid aspect ratio χ with different detuning values. We see that in all three cases when increasing χ, the quantum beat period decreases (or the quantum beat frequency increases as argued above) and approaches the same value which is said to be the period of quantum beat in the bulk semiconductor. In addition, we see that as the detuning increases, the quantum beat period decreases accordingly.

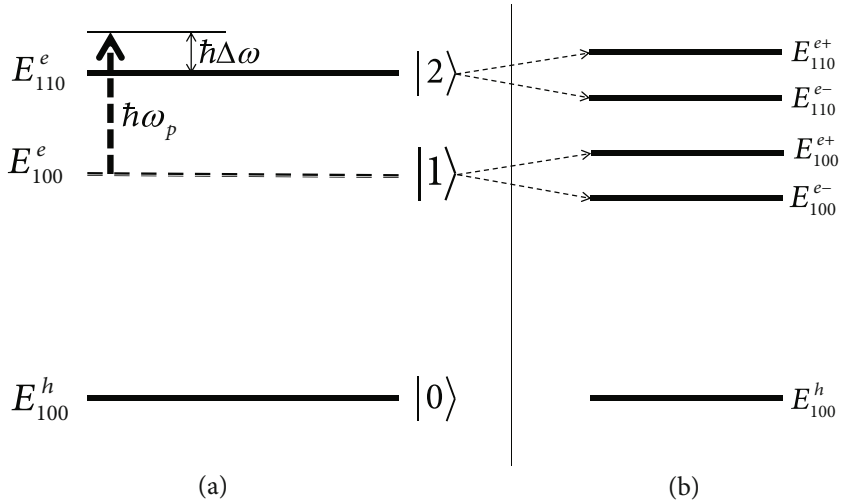

FIGURE 10: Three-level energy diagram of electron and hole: (a) before the effect of the pump laser. E^h_{100} is the lowest quantized energy level of the hole corresponding to the state $|0\rangle$; E^e_{100} and E^e_{110} are the first quantized levels of the electron corresponding to the states $|1\rangle$ and $|2\rangle$. (b) After the system is illuminated by a strong resonant pump laser with the photon energy $\hbar\omega_p \simeq E^e_{110} - E^e_{100}$, electron energy levels are split: E^e_{100} is split into E^{e-}_{100} and E^{e+}_{100}, E^e_{110} is split into E^{e-}_{110} and E^{e+}_{110}; $\hbar\Delta\omega$ is the detuning of the pump wave and the two quantized levels of the electron.

This relationship will be discussed in detail in the scenario of Figure 6.

Figure 6 examines the dependence of the feature of quantum beat of excitons on the pump field detuning. We see that as the detuning increases, both the period and the amplitude of quantum beat decrease. It is clear that as the detuning increases, the coupling probability of two electron energy level lowers, leading to a decrease in the splitting of the electron energy levels as well as a decrease in the ability to generate two closely spaced excitons. As a result, the probability of generating quantum beats decreases, leading to a smaller amplitude of quantum beat. Besides, according to Equation (11), the oscillation frequency of beat is proportional to the detuning so when we increase the detuning, the oscillation frequency of beat increases, or the oscillatory period of quantum beat decreases. Notably, when the detuning is too large, we cannot observe the oscillation of the absorption intensity over time, that is, the quantum beat of excitons does not appear (corresponding to $\hbar\Delta\omega = 15$ meV represented by the dotted line in Figure 7).

Next, we examine the relation between the period of quantum beat and the detuning of the pump wave (Figure 7). The graph in Figure 7 reveals that when the detuning increases, the period of quantum beat decreases as mentioned above and that periods of various detuning values approach the same value that is said to be the oscillatory period of the initial excitons. In addition, we see that the period of quantum beat decreases with the increasing value of the ellipsoid aspect ratio χ as explained in the discussion of Figure 6. Compared to spherical quantum dots, which have only radius to work with, ellipsoidal QDs have more adjustable geometrical parameters such as semi-minor axis and semi-major axis. It makes easier for one to adjust and obtain desired optical properties in more detailed exciton energy spectrum [42, 43].

Finally, we compare the absorption intensity of excitons in the prolate ellipsoidal QD Figure 8(a)) and the spherical one (Figure 8(b)) [35] with the same volume. Starting from Equation (A.14), we consider the prolate ellipsoidal QD with $a = 25$ Å and $\chi = 4.096$ that has the same volume as the spherical one with radius $R = 40$ Å. The graph in Figure 8 shows that the characteristics of the quantum beat of excitons in two QDs of different shapes but having the same volume are completely different. This means that the quantum beat of excitons depends not only on the pump laser detuning, size of QDs but also on their geometric shapes. The reason for the difference between the feature of the quantum beat in those two kinds of QDs can be explained as follows. As we know, the shape of the QDs strongly influences the wavefunctions as well as the energy spectrum of particles. So, for two QDs with different shapes, the wavefunctions and the corresponding energy spectra are completely different, even though the QDs have the same volume. This results in the photon energy of the probe laser necessary to excite interband transitions in the prolate ellipsoidal QDs being different from that in the spherical ones, that is, the absorption intensity of excitons in these QDs is different. In addition, in this paper, we use the renormalized wavefunction method based on the theory of quantum mechanics, so our formulation can be applied to other quantum structures as long as we can define the wavefunctions and energy spectrum of particles. In fact, we have applied our theory to similar problems in the spherical QDs as well as in quantum wires and quantum wells [16, 18, 35, 36, 41].

4. Conclusion

In this work, we have studied quantum beats of excitons in InGaAs/InAlAs prolate ellipsoidal QDs using a three-level model by the renormalized wavefunctions method. We have

found the form of the renormalized wavefunction of exciton and calculated the absorption intensity of excitons in two cases without and with the effect of the pump laser. In the presence of a resonant pump laser, the time-dependent spectrum of the exciton absorption intensity has the form of a damped periodic oscillation with a frequency being twice the electron Rabi frequency. That oscillatory behavior of the exciton absorption intensity reveals the existence of quantum beats in these QDs. The amplitude and frequency (or period) of quantum beats depend very sensitively on the detuning as well as the ellipsoid aspect ratio. The semi-minor axis and semi-major one have made controlling optical properties in ellipsoidal QDs easier and more flexible than in the spherical QDs. This is one interesting advantage of the ellipsoidal QDs over spherical ones. Moreover, the features of quantum beats of excitons also depend sensitively on geometric shapes of QDs. Specifically, with the same volume, the frequency and amplitude of quantum beats in the two spherical and prolate ellipsoidal QDs are completely different. We believe that the interesting features in optical absorption of QDs when the quantum beat of excitons occurs will have great potential for application in manufacturing quantum-computing devices. We expect our findings to be confirmed by further appropriate experiments.

Appendix

For the sake of convenience, we recall here the wavefunctions and the energy spectra of electron and hole in prolate ellipsoidal quantum dots (QDs) [18–22]. Consider the prolate ellipsoidal QD with rotational symmetry around the z axis. Let a and c be the length of semi-axes of the ellipse in the xOy plane and z-direction, respectively, where x, y, z are the coordinates in Cartesian coordinate system with its origin at the ellipsoid symmetry center. For simplicity, we have assumed the prolate ellipsoidal QD is in an infinite potential and has the form [18–22]

$$U\left(\vec{r}\right) = \begin{cases} 0, & 0 < S\left(\vec{r}_i\right) < 1, \\ \infty, & S\left(\vec{r}_i\right) \geq 1, \end{cases} \tag{A.1}$$

where $S(\vec{r}_i)$ depends on parameters a and c which are the semi-axes of the ellipsoidal QD; we have

$$S\left(\vec{r}_i\right) = \frac{x^2 + y^2}{a^2} + \frac{z^2}{c^2}, \tag{A.2}$$

with $c > a$, we have the prolate ellipsoidal QD as shown in Figure 9.

The envelope wavefunctions of electron (hole) in prolate ellipsoidal QD have the form [19–23]

$$\Psi_{nlm}^{e,h}(\xi, \eta, \varphi) = A_{nlm} J_{lm}^{(1)}(h, \xi) S_{lm}^{(1)}(h, \eta) e^{im\varphi}, \tag{A.3}$$

where $n = 1, 2, 3, \cdots$; $l = 0, 1, 2, 3, \cdots$; $m = -l, \cdots, 0, \cdots, +l$; $J_{lm}^{(1)}(h, \xi)$ and $S_{lm}^{(1)}(h, \xi)$ are prolate radial and prolate angular spheroidal functions of the first kind, respectively; A_{nlm} is the normalization coefficient

$$A_{nlm} = \sqrt{\frac{\chi^3}{2\pi c^3 e^3 \int_1^{\bar{\xi}} \int_{-1}^{+1} \left(\xi^2 + \eta^2\right) J_{lm}^{(1)*}(h, \xi) S_{lm}^{(1)*}(h, \eta) J_{lm}^{(1)}(h, \xi) S_{lm}^{(1)}(h, \eta) d\xi d\eta}}, \tag{A.4}$$

where

$$\chi = \frac{c}{a}, \tag{A.5}$$

and e is the ellipsoid eccentricity

$$e = \sqrt{1 - \frac{1}{\chi^2}}. \tag{A.6}$$

The energy of electron (hole) is given as

$$\varepsilon_{nlm}^{e,h} = \frac{\hbar^2 k_{nlm}}{2m_{e,h}^*}, \tag{A.7}$$

where

$$k_{nlm} = \frac{h^2}{f^2}. \tag{A.8}$$

The values of h are found from the boundary condition

$$J_{lm}^{(1)}\left(h, \bar{\xi}\right) = 0, \tag{A.9}$$

where

$$\bar{\xi} = \frac{1}{\sqrt{1 - 1/\chi^2}} = \frac{1}{e}, \tag{A.10}$$

$$f = \frac{c}{\bar{\xi}} = c \cdot e. \tag{A.11}$$

The values of the parameter h depend on the values of the indices n, l, m. When $h \longrightarrow 0$ (or $f \longrightarrow 0$, the prolate ellipsoidal QD will become the spherical one and $\chi \longrightarrow 1$. Then, the wavefunctions of electron (hole) in QD will have the following form [44]

$$\Psi_{nlm}^{S(e,h)}(r,\theta,\varphi) = \sqrt{\frac{2}{R^3}} \frac{j_l(\chi_{nl}(r/R))}{j_{l+1}(\chi_{nl})} Y_{lm}(\theta,\varphi), \tag{A.12}$$

where $Y_{lm}(\theta,\varphi)$ is the spherical harmonic function; $j_l(r)$ is the spherical Bessel function with χ_{nl} is its zeros. The energy levels of electron (hole) being consistent with wavefunctions in Equation (A.12) are determined by

$$E_{nl}^{S(e,h)} = \frac{\hbar^2 \chi_{nl}^2}{2m_{e,h}R^2}. \tag{A.13}$$

In Equations. (A.12) and (A.13), indices n, l, m are principle, orbital, and azimuthal quantum numbers, respectively. Since the spherical symmetry has been lost, for the ellipsoidal QDs, the index l in the wavefunctions and energy expressions of the particle in Equations (A.3) and (A.7) no longer means the orbital quantum numbers. However, here, we still use indices n, l, m in Equations (A.3) and (A.7) to get one-to-one correspondence between the prolate ellipsoidal and spherical QD when $\chi \longrightarrow 1$. The volume of prolate ellipsoidal QD of semi-axes a and c is defined as

$$V = \frac{4}{3}\pi a^2 c = \frac{4}{3}\pi a^3 \chi = \frac{4}{3}\pi R_S^3, \tag{A.14}$$

with $R_s = a\sqrt[3]{\chi}$ being the radius of a sphere with the same volume.

A. The Case without the Pump Laser

In the effective mass envelope-function approximation, the total wavefunction of electron (hole) in a prolate ellipsoidal QD with infinite potential is given as

$$\Lambda_{nlm}^{e,h}\left(\vec{r}\right) = u_{c,v}\left(\vec{r}\right)\Psi_{nlm}^{e,h}(\xi,\eta,\varphi), \tag{A.15}$$

where $\vec{r} = (\xi,\eta,\varphi)$ and $u_{c,v}(\vec{r})$ are the periodic Bloch functions in conduction and valence band. Choosing zero energy at the top of the valence band, the energy expression of electron and hole (in Equation (A.7)) is rewritten as follows, respectively

$$E_{nlm}^{e} = E_g + \frac{\hbar^2 k_{nlm}}{2m_e^*}, \tag{A.16}$$

$$E_{nlm}^{h} = \frac{\hbar^2 k_{nlm}}{2m_h^*}, \tag{A.17}$$

where E_g is the bandgap of the semiconductor.

We examine a three-level energy model where E_{100}^h is the lowest quantized energy level of the hole corresponding to the state $|0\rangle$; E_{100}^e and E_{110}^e are the first quantized levels of the electron corresponding to the states $|1\rangle$ and $|2\rangle$, see Figure 10(a).

Here, we need to use the time-dependent wavefunctions of the particles to find the time-dependent properties of the quantum beats. The time-dependent wavefunctions of the particles are now defined with

$$\begin{cases} \Lambda_{100}^{h}\left(\vec{r},t\right) = \Lambda_{100}^{h}\left(\vec{r}\right)e^{-i/\hbar E_{100}^{h}t}, \\ \Lambda_{100}^{e}\left(\vec{r},t\right) = \Lambda_{100}^{e}\left(\vec{r}\right)e^{-i/\hbar E_{100}^{e}t}, \\ \Lambda_{110}^{e}\left(\vec{r},t\right) = \Lambda_{110}^{e}\left(\vec{r}\right)e^{-i/\hbar E_{110}^{e}t}. \end{cases} \tag{A.18}$$

B. The Case with the Pump Laser

To search for the quantum beats in three-level model, we used two different laser beams concurrently. A strong pump laser resonant with two electron energy levels is irradiated to support the intersubband transition between these levels. A weak probe laser is utilized to search for the excitonic transitions between ground state and excited ones of exciton. The lasers can be described as follows:

$$\vec{E}(t) = \vec{n}A_x e^{-i\omega_x t}, \tag{A.19}$$

where $\vec{n}$ is the unit vector along the wave propagation direction; A_x and ω_x are the amplitude and frequency of lasers with x indicating which laser is pump or probe laser.

In case the electromagnetic field is not too strong, we can omit the higher-order term, and by applying some gauges and approximations, the expression for the Hamiltonian interaction between the electron and the electromagnetic field can be written as follows [44, 45].

$$\widehat{H}_{\text{int}} = -\frac{q}{m_0}\frac{A_x e^{-i\omega_x t}}{i\omega_x}\vec{n}\cdot\widehat{\vec{p}}, \tag{A.20}$$

where q, m_0, and $\vec{p}$ are the charge, the bare mass, and the momentum of the electron, respectively.

When there is the effect of strong pump laser resonating with the energy distance between the two quantized levels of the electron, the wavefunctions of the electron are renormalized under the effect of the pump laser and have the form

$$\Lambda_{\text{mix}}^{e}\left(\vec{r},t\right) = \sum_{l=0}^{1} c_l(t)\Lambda_{1l0}^{e}\left(\vec{r}\right)\exp\left(-\frac{i}{\hbar}E_{1l0}^{e}t\right), \tag{A.21}$$

where coefficients $c_l(t)$ $(l = \overline{0,1})$ are determined from the time-dependent Schrödinger equation and has the following expression [16]:

$$\begin{cases} c_0(t) = \dfrac{1}{2\Omega_R}\left(\alpha_1 e^{i\alpha_2 t} + \alpha_2 e^{-i\alpha_1 t}\right), \\ c_1(t) = -\dfrac{V_{21}}{2\Omega_R}\left(e^{i\alpha_1 t} - e^{-i\alpha_2 t}\right), \end{cases} \tag{A.22}$$

where

$$\begin{cases} \alpha_1 = \Omega_R - \dfrac{\Delta\omega}{2}, \\ \alpha_2 = \Omega_R + \dfrac{\Delta\omega}{2}, \\ \Omega_R = \left[\left(\dfrac{\Delta\omega}{2}\right)^2 + \dfrac{|V_{21}|^2}{\hbar^2}\right]^{1/2}, \end{cases} \tag{A.23}$$

$$\begin{cases} \Delta\omega = \omega_p - \omega_{21}, \\ \hbar\omega_{21} = E^e_{110} - E^e_{100}, \end{cases} \tag{A.24}$$

and V_{21} is the matrix element for an intersubband transition and has the form

$$\begin{aligned} V_{21} = {} & \frac{qA_p}{m_0 i\omega_p}\frac{m^*_e}{i\hbar}(E_2 - E_1)2\pi f^4 \times \\ & \times \int_1^{\bar{\xi}}\int_{-1}^{+1} \xi\eta\left(\xi^2 - \eta^2\right) J^{(1)*}_{10}(h,\xi) S^{(1)*}_{10} \\ & \cdot (h,\eta) J^{(1)}_{00}(h,\xi) S^{(1)}_{00}(h,\eta) d\xi d\eta, \end{aligned} \tag{A.25}$$

with q and m_e are the charge and the effective electron mass, $\hbar$ is Planck's constant, $f = c/\bar{\xi} = ce$; A_p, ω_p are the magnitude and the frequency of the pump laser, respectively.

Substituting coefficients $c_0(t)$ and $c_1(t)$ in Equation (A.22) into Equation (A.21), we obtain the formula for the renormalized wavefunction of electron under the effect of the pump laser as

$$\begin{aligned} \Lambda^e_{\text{mix}}\left(\vec{r}, t\right) = {} & \frac{1}{2\Omega_R}\left(\alpha_1 e^{i\alpha_2 t} + \alpha_2 e^{-i\alpha_1 t}\right) e^{-i/\hbar E^e_{100} t} \Lambda^e_{100}\left(\vec{r}\right) \\ & - \frac{V_{21}}{2\hbar\Omega_R}\left(e^{i\alpha_1 t} - e^{-i\alpha_2 t}\right) e^{-i/\hbar E^e_{110} t} \Lambda^e_{110}\left(\vec{r}\right). \end{aligned} \tag{A.26}$$

Put

$$\begin{cases} E^{e+}_{100} = E^e_{100} + \hbar\alpha_1, \\ E^{e-}_{100} = E^e_{100} - \hbar\alpha_2, \end{cases} \tag{A.27}$$

$$\begin{cases} E^{e+}_{110} = E^e_{110} + \hbar\alpha_2, \\ E^{e-}_{110} = E^e_{110} - \hbar\alpha_1. \end{cases} \tag{A.28}$$

From Equations (A.27) and (A.28), we can rewrite the renormalized wavefunctions of the electron under the effect of the pump laser in expression (A.26) as follows:

$$\begin{aligned} \Lambda^e_{\text{mix}}\left(\vec{r}, t\right) = {} & \frac{1}{2\Omega_R}\left(\alpha_1 e^{-i/\hbar E^{e-}_{100} t} + \alpha_2 e^{-i/\hbar E^{e+}_{100} t}\right) \Lambda^e_{100}\left(\vec{r}\right) \\ & - \frac{V_{21}}{2\hbar\Omega_R}\left(e^{-i/\hbar E^{e-}_{110} t} - e^{-i/\hbar E^{e+}_{110} t}\right) \Lambda^e_{110}\left(\vec{r}\right). \end{aligned} \tag{A.29}$$

It should also note that $\hbar\Delta\omega = \hbar\omega_p - \hbar\omega_{21}$ is the detuning between the pump laser and two initial levels of electron E^e_{100} and E^e_{110}. We find that those two initial levels are all split under the effect of a resonant strong pump laser, Figure 10(b). The quasienergy spectrum of electron now includes four splitting levels, where two levels are split from the first original level E^e_{100} defined in Equation (A.27), and two levels are split from the second original level E^e_{110} defined in Equation (A.28).

Data Availability

The material data used to support the findings of this study are included within the article.

Conflicts of Interest

The authors declare that they have no conflicts of interest.

Acknowledgments

This research is funded by the Vietnam's Ministry of Education and Training (MOET) under grant number B-2020-DHH-06. We would like to thank Dr. Tran Quang Ngoc Thuy, University of Foreign Languages, Hue University, Vietnam, for her kind assistance in manuscript preparation.

References

[1] K. Li, K. Guo, and L. Liang, "Effect of the shape of quantum dots on the refractive index changes," *Physica B*, vol. 502, pp. 146–150, 2016.

[2] J. Fang, Z. Zhou, M. Xiao, Z. Lou, Z. Wei, and G. Shen, "Recent advances in low-dimensional semiconductor nanomaterials and their applications in high-performance photodetectors," *InfoMat*, vol. 2, no. 2, pp. 291–317, 2020.

[3] J. Wu, S. Chen, A. Seeds, and H. Liu, "Quantum dot optoelectronic devices: lasers, photodetectors and solar cells," *Journal of Physics D: Applied Physics*, vol. 48, article 363001, pp. 1–28, 2015.

[4] L. Aderras, E. Feddi, A. Bah, F. Dujardin, and C. A. Duque, "On the electronic states in lens-shaped quantum dots," *Physica Status Solidi (b)*, vol. 254, no. 10, article 1700144, pp. 1–8, 2017.

[5] P. Dimitrakis, P. Normand, V. Ioannou-Sougleridis et al., "Quantum dots for memory applications," *Physica Status Solidi (A)*, vol. 210, no. 8, pp. 1490–1504, 2013.

[6] B. Talluri, E. Prasad, and T. Thomas, "Critical role of surfactants in the formation of digestively-ripened, ultra-small (r<2 nm) copper oxide quantum dots," *Superlattices and Microstructures*, vol. 116, pp. 122–130, 2018.

[7] S. Kaur, S. Sharma, A. Umar, S. Singh, S. K. Mehta, and S. K. Kansal, "Solar light driven enhanced photocatalytic

degradation of brilliant green dye based on ZnS quantum dots," *Superlattices and Microstructures*, vol. 103, pp. 365–375, 2017.

[8] A. Mehramiz, J. Mahmoodi, and S. Sobhanian, "Approximation method for a spherical bound system in the quantum plasma," *Physics of Plasmas*, vol. 17, article 082110, pp. 1–6, 2010.

[9] D. Kandi, S. Martha, and K. M. Parida, "Quantum dots as enhancer in photocatalytic hydrogen evolution: a review," *International Journal of Hydrogen Energy*, vol. 42, no. 15, pp. 9467–9481, 2017.

[10] M. F. Frasco and N. Chaniotakis, "Semiconductor quantum dots in chemical sensors and biosensors," *Sensors*, vol. 9, no. 9, pp. 7266–7286, 2009.

[11] K. D. Wegner and N. Hildebrandt, "Quantum dots: bright and versatile in vitro and in vivo fluorescence imaging biosensors," *Chemical Society Reviews*, vol. 44, no. 14, pp. 4792–4834, 2015.

[12] N. Hildebrandt, "Biofunctional quantum dots: controlled conjugation for multiplexed biosensors," *Acs Nano*, vol. 5, pp. 5286–5290, 2011.

[13] Q.-Y. Ye, R. Tsu, and E. H. Nicollian, "Resonant tunneling via microcrystalline-silicon quantum confinement," *Physical Review B*, vol. 44, pp. 1806–1811, 1991.

[14] V. A. Harutyunyan, E. M. Kazaryan, A. A. Kostanyan, and H. A. Sarkisyan, "Interband transitions in cylindrical layer quantum dot: influence of magnetic and electric fields," *Physica E*, vol. 36, no. 1, pp. 114–118, 2007.

[15] C.-H. Liu and B.-R. Xu, "Theoretical study of the optical absorption and refraction index change in a cylindrical quantum dot," *Physics Letters A*, vol. 372, no. 6, pp. 888–892, 2008.

[16] D. N. Thao, L. T. N. Bao, D. D. Phuoc, and N. H. Quang, "A theoretical study of the optical Stark effect in InGaAs/InAlAs quantum dots," *Semiconductor Science and Technology*, vol. 32, article 025014, pp. 1–8, 2017.

[17] L. Liang and W. Xie, "Influence of the shape of quantum dots on their optical absorptions," *Physica B*, vol. 462, pp. 15–17, 2015.

[18] L. T. N. Bao, D. D. Phuoc, L. T. D. Hien, and D. N. Thao, "On the optical stark effect of excitons in InGaAs prolate ellipsoidal quantum dots," *Journal of Nanomaterials*, vol. 2021, Article ID 5586622, 12 pages, 2021.

[19] G. Cantele, D. Ninno, and G. Iadonisi, "Confined states in ellipsoidal quantum dots," *Journal of Physics: Condensed Matter*, vol. 12, pp. 9019–9036, 2000.

[20] G. Cantele, D. Ninno, and G. Iadonisi, "Calculation of the infrared optical transitions in semiconductor ellipsoidal quantum dots," *Nano Letters*, vol. 1, no. 3, pp. 121–124, 2001.

[21] G. Cantele, G. Piacente, D. Ninno, and G. Iadonisi, "Optical anisotropy of ellipsoidal quantum dots," *Physical Review B*, vol. 66, article 113308, pp. 1–4, 2002.

[22] G. Iadonisi, G. Cantele, V. M. Ramaglia, and D. Ninno, "Electronic and optical properties of semiconductor nanostructures," *Physica Status Solidi (b)*, vol. 237, no. 1, pp. 320–340, 2003.

[23] V. I. Boichuk, V. B. Hol'skyi, R. Y. Kubay, and R. I. Lukin, "The electron energy spectrum in an ellipsoidal quantum dot with regard for finite band gap at the interface," *Ukrainian Journal of Physics*, vol. 53, pp. 574–578, 2008.

[24] E. Perfetto, D. Sangalli, A. Marini, and G. Stefanucci, "First-principles approach to excitons in time-resolved and angle-resolved photoemission spectra," *Physical Review B*, vol. 94, article 245303, pp. 1–15, 2016.

[25] A. Rustagi and A. F. Kemper, "Coherent excitonic quantum beats in time-resolved photoemission measurements," *Physical Review B*, vol. 99, article 125303, pp. 1–7, 2019.

[26] V. Trifonov, I. Ya, I. Gerlovin et al., "Multiple-frequency quantum beats of quantum confined exciton states," *Physical Review B*, vol. 92, article 201301, pp. 1–5, 2015.

[27] S. Ohta, O. Kojima, T. Kita, and T. Isu, "Observation of quantum beat oscillations and ultrafast relaxation of excitons confined in GaAs thin films by controlling probe laser pulses," *Journal of Applied Physics*, vol. 111, article 023505, pp. 1–4, 2012.

[28] K. Leo, J. Shah, E. O. Göbel et al., "Coherent oscillations of a wave packet in a semiconductor double-quantum-well structure," *Physical Review Letters*, vol. 66, no. 2, pp. 201–204, 1991.

[29] M. Koch, J. Feldmann, G. V. Plessen, E. O. Göbel, P. Thomas, and K. Köhler, "Quantum beats versus polarization interference: an experimental distinction," *Physical Review Letters*, vol. 69, no. 25, pp. 3631–3634, 1992.

[30] J. Erland and I. Balslev, "Theory of quantum beat and polarization interference in four-wave mixing," *Physical Review A*, vol. 48, no. 3, pp. R1765–R1768, 1993.

[31] M. S. C. Luo, S. L. Chuang, P. C. M. Planken, I. Brener, and M. C. Nuss, "Coherent double-pulse control of quantum beats in a coupled quantum well," *Physical Review B*, vol. 48, no. 15, pp. 11043–11050, 1993.

[32] A. I. Bobrysheva, M. I. Shmiglyuk, and V. G. Pavlov, "Optical exciton Stark effect and quantum beats at exciton quasienergy levels in quantum wells," *Physics of the Solid State*, vol. 39, no. 7, pp. 1147–1149, 1997.

[33] S. Schmitt-Rink, D. Bennhardt, V. Heuckeroth et al., "Polarization dependence of heavy- and light-hole quantum beats," *Physical Review B*, vol. 46, no. 16, pp. 10460–10463, 1992.

[34] K.-H. Pantke, P. Schillak, J. Erland, V. G. Lyssenko, B. S. Razblrin, and J. M. Hvam, "Nonlinear quantum beats of excitons in CdSe," *Physica Status Solidi (b)*, vol. 173, no. 1, pp. 91–98, 1992.

[35] D. N. Thao and L. T. N. Bao, "Quantum beat of excitons in spherical semiconductor quantum dots," *Superlattices and Microstructures*, vol. 146, article 106675, pp. 1–12, 2020.

[36] D. D. Phuoc, L. T. N. Bao, L. T. D. Hien, H. K. Hieu, and D. N. Thao, "A study on quantum beats of excitons in GaAs/AlGaAs circular cylindrical quantum wires," *Japanese Journal of Applied Physics*, vol. 59, article 125003, pp. 1–10, 2020.

[37] H. Asai and Y. Kawamura, "Intersubband absorption in $In_{0.53}Ga_{0.47}As/In_{0.52}Al_{0.48}As$ multiple quantum wells," *Physical Review B*, vol. 43, no. 6, pp. 4748–4759, 1991.

[38] K. F. Renk, *Basics of Laser Physics: For Students of Science and Engineering*, Springer, Berlin, 2nd ed. edition, 2017.

[39] M. A. Ladugin, I. V. Yarotskaya, T. A. Bagaev et al., "Advanced AlGaAs/GaAs heterostructures grown by MOVPE," *Crystals*, vol. 9, p. 305, 2019.

[40] S. Cao, Y. Zhao, S. Feng et al., "Theoretical analysis of InGaAs/InAlAs single-photon avalanche photodiodes," *Nanoscale Research Letters*, vol. 14, no. 1, pp. 2–8, 2019.

[41] L. T. N. Bao and D. N. Thao, "Theoretical investigation of quantum beat of excitons in GaAs/AlGaAs quantum wells," in *The 42nd Vietnam National Conf. on Theoretical Physics (NCTP-42)*, Cantho, Vietnam, 2017.

[42] G. Rezaei, M. R. K. Vahdani, and B. Vaseghi, "Nonlinear optical properties of a hydrogenic impurity in an ellipsoidal finite

potential quantum dot," *Current Applied Physics*, vol. 11, no. 2, pp. 176–181, 2011.

[43] T. Chen, W. Xie, and S. Liang, "The nonlinear optical rectification of an ellipsoidal quantum dot with impurity in the presence of an electric field," *Physica E*, vol. 44, no. 4, pp. 786–790, 2012.

[44] L. Bányai and S. W. Koch, *Semiconductor Quantum Dots*, World Scientific, Singapore, 1st ed. edition, 1993.

[45] R. Jorio, G. D. Saito, M. S. Dresselhaus, and M. S. Dresselhaus, *Raman spectroscopy in graphene related systems*, John Wiley & Sons, 2011.

Hindawi
Journal of Nanomaterials
Volume 2022, Article ID 5791922, 10 pages
https://doi.org/10.1155/2022/5791922

Research Article

Novel Integrated Nanofertilizers for Improving the Growth of *Polyscias fruticosa* and *Asparagus officinalis*

Thi Thu Huong Le,[1,2] **Thi Thu Trang Mai**,[1] **Ke Son Phan**,[1] **Thi Minh Nguyen**,[3] **Thi Lan Anh Tran**,[1] **Thi Nham Dong**,[1] **Huu Chung Tran**,[4] **Thi Thanh Hang Ngo**,[4] **Phuong Ha Hoang**,[3] **and Phuong Thu Ha**[1]

[1]*Institute of Materials Science, Vietnam Academy of Science and Technology, 18 Hoang Quoc Viet Road, Cau Giay District, Hanoi, Vietnam*
[2]*Department of Chemitry, Faculty of Natural Resources & Environment, Vietnam National University of Agriculture, Trau Quy, Gia Lam District, Hanoi, Vietnam*
[3]*Institute of Biotechnology, Vietnam Academy of Science and Technology, 18 Hoang Quoc Viet Road, Cau Giay District, Hanoi, Vietnam*
[4]*Evergreen Agricoop Truong Xuan, Nam Dinh, Vietnam*

Correspondence should be addressed to Thi Thu Trang Mai; trangmt23@gmail.com and Phuong Thu Ha; hpthu74@gmail.com

Received 31 January 2022; Revised 25 March 2022; Accepted 4 April 2022; Published 28 April 2022

Academic Editor: Nguyen Duc Cuong

The study of nanotechnology has been focused in recent years on the application in various fields including agriculture. Nanofertilizers were suggested to have the ability to supply plants with nutrients more effectively and thus significantly improve crop productivity. Previous studies reported the fabrication of nanofertilizers that contained only one or two essential elements. The addition of other nutrients is necessary for promoting plant development. Therefore, in this study, a novel integrated nanofertilizer containing both macro- and micronutritional elements was synthesized and characterized. The results showed that the prepared fertilizer had the rod shape and nanosize of 20-30 nm in width and 80 nm in length. Treatment of *Polyscias fruticosa* and *Asparagus officinalis* crops with the integrated nanofertilizer increased the number of branches, leaf area, dry matter production, and total biomass up to 50% at using level of 5% compared to nontreatment groups.

1. Introduction

For decades, the use of fertilizers in agriculture has doubled the world food production. However, the common drawback of using fertilizers is that a major part of the nutrient contents, such as nitrogen, phosphorus, and potassium, are often dissolved in soil that is over the amount of plant requirement. These contents are then washed away from the soil (50-70%) before being used [1]. Consequently, fertilizers must be applied many times throughout the plant development process. The overuse of these chemicals resulted in residue in agricultural products and serious environmental pollution as well as the disruption of the agricultural ecosystem and soil quality depression [2].

Many studies have proven the effectiveness and cost savings of nanotechnology in providing nutrients to plants. The nanofertilizer allows incorporating nutrients onto a nanodimensional adsorbent. Therefore, this approach leads to the controlled release of active ingredients for a long time and prevents the leaching of nutrients into groundwater, thus reducing the amount of fertilizer used. It is estimated that the amount of nanoformulations needed for plants is only equivalent to 20% of conventional fertilizers [3]. For example, urea (N fertilizer) was incorporated into slow release nanohybrids, and the nanohybrids demonstrated a higher rice crop yield at a 50% lower concentration of urea [4]. Research by Tarafdar et al. [5] showed that soybean growth rate increased by 33% and grain yield improved by 20%

when used nano-P fertilizer instead of conventional phosphate fertilizer [5]. Another study showed the effect of nanozeolite/nanohydroxyapatite as nanofertilizer to increase the P availability in the soil and chamomile yield compared to natural zeolite/hydroxyapatite or normal fertilizer [6].

Besides the need for NPK, a lot of other nutritional elements with less quantity such as Fe, B, and Zn are important factors to ensure the productivity and quality of agricultural products [7]. They serve as a cofactor for various enzymes associated with carbohydrates, nucleic acids, proteins, and lipids. The concentration requirement of these traces is narrow in the ranges from 0.1 mg/kg dry mass (e.g., Mo and Ni) to 100 mg/kg (e.g., Cl and Fe) (Plant [8]). The insufficient amount of micronutrients can slow down the plant growth rate and force the plant to switch to alternative metabolic pathways that less depend on the limiting micronutrients. In those cases, these elements can be supplied in the soil or sprayed onto leaves in the form of fertilizer solution [9]. However, the dynamics and transformation of these elements are greatly affected by even small changes in environmental factors such as pH and organic composition as well as microbial activity in the soil. Therefore, investigating an alternative way to effectively provide these elements to plants is necessary [3].

A study reported that the addition of Zn micronutrients containing foliar fertilizer in the form of ZnO nanoparticles at the concentration of 20 mg/l increased 42%, 41%, 98%, and 76% of root length, root biomass, stem length, and stem mass of soybean, respectively [10]. These superior characteristics make nanofertilizers be an outstanding choice compared to traditional fertilizers. Despite their potential, studies on the application of nutrient nanoformulation are generally at a small scale of testing [4, 11]. Therefore, the research and development of commercially integrated nanoformulations is an urgent requirement.

There are several types of nanofertilizers in terms of their compositions. First, nanofertilizers can be particles in nanosize of elements such as Fe [12], Cu, Ag [13] and nano ZnO [14]. Second, nanofertilizers can also be in the slow release formulations formed by various polymers. For example, hydroxypropyl methylcellulose modified with xanthan or chitosan was used for fabrication of KNO_3 nanofertilizer [15]. Chitosan and poly(vinyl alcohol) were the coated material for NPK fertilizer. The hydrophilic coating layer provided the fertilizer with slow-release activity [16]. Third, several minerals can act as nutrient sources or nutrient carriers. Nanohydroxyapatite and nanozeolite were used as nano-phosphorous sources [6, 17] or as urea carrier [4]. Some nanofertiliezers were reported to be the hybrids of the minerals and polymers such as montmorillonite clay-polycaprolacton/polyacrylamine [18] or nanohydroxyapatite encapsulated wood [19]. While some studies showed only the material properties of the nanofertilizer without their effects on any crops [15, 16, 18, 19], some others only provided the influences of the fertilizers on plants without details on the fertilizer characteristics [20–22].

Recently, we have reported the positive effects of micronutrient nanoformulation on *Asparagus officinalis* seeds [23]. In this study, we synthesized novel integrated nanoformulas of nutrients that contained both the macronutrients of N, P, and K as well as the trace elements of Zn^{2+}, Cu^{2+}, Co^{2+}, Fe^{3+}, and Ag^{+} (in nanoparticle form) to stimulate the growth of *Polyscias fruticose* and *Asparagus officinalis*. *Polyscias fruticosa* and *Asparagus officinallis* were chosen for this study because of their high value in nutrition in medicine [24, 25]. To the best of our knowledge, this is the first time such an integrated nanofertilizer has been fully characterized and investigated to apply to these plants. Besides, the second novelty of the manuscript in the required amount of our nanofertilizer was only 5% in comparison with conventional fertilizer to provide up to 50% increase in growth and production parameters on *Polyscias fruticosa* and *Asparagus officinalis*.

2. Materials and Methods

2.1. Materials and Methods

2.1.1. Materials. Hydroxyapatite, alginate, carboxyl methyl cellulose, sodium borohydride ($NaBH_4$), and silver nitrate ($AgNO_3$) were purchased from Merck. Iron(III) chloride hexahydrate ($FeCl_3.6H_2O$), copper sulfate pentahydrate ($CuSO_4.5H_2O$), cobalt (II) sulfate ($CoSO_4$), magnesium sulfate ($MgSO_4$), zinc oxide (ZnO), and commercial NPK fertilizer and commercial NPK + trace element (TE) fertilizer (NPK-15-15-15 and NPK-15-15-15 + TE, provided by Binh Dien Fertilizer Joint Stock Company, composition: total N: 15%, available P (P_2O_5): 15%; available potassium (K_2O): 15%, SiO_2: 1%, Zn: 100 ppm, Cu: 100 ppm, Fe: 100 ppm, B: 200 ppm) were purchased in Vietnam.

2.1.2. Synthesis of Integrated Nanofertilizer. The nanofertilizer synthesis consisted of 3 steps. First, the mixture of commercial NPK and hydroxyapatite (at a specified ratio) was used to fabricate the NPK-hydroxyapatite nanohybrid structure by chemical method. Then, microelement solutions containing Ag, Fe, Cu, Co, and Zn in the form of nanoparticles were synthesized by chemical reduction method using $NaBH_4$ as a reducing agent. Finally, the microelement solution and NPK nanostructures were integrated into water-retaining materials like alginate.

In details, 75 g of hydroxyapatite was dispersed in 3 liters of distilled water for 30 min. Then, 1 liter of alginate solution (150 g/l) was slowly added to the above suspension and stirred for 30 minutes. 400 g of commercial NPK fertilizer was suspended in 0.5 liters of distilled water for 30 minutes and then slowly added to the above suspension. Microelements were dissolved or dispersed in distill water as follows: 2 g $AgNO_3$ in 1.18 liters of water, each of $CuSO_4.5H_2O$ (7.20 g), $FeCl_3.6H_2O$ (9.60 g), $CoCl_2.6H_2O$ (8.00 g), and ZnO (2.50 g) in 250 mL of water. The microelement solutions or suspension were slowly added to the above hydroxyapatite solutions in the order of $AgNO_3$, $FeCl_3$, $CuSO_4.5H_2O$, $CoCl_2.6H_2O$, and ZnO suspension into the reaction mixture, while continuously stirring for 30 minutes. 47.5 g of $NaBH_4$ was dissolved in 1 liter of distilled water and then slowly added to the obtained solution and stirred for 30 minutes. Then, 5 g/l carboxylmethyl cellulose solution was slowly added until the viscosity of the reaction mixture reached 20 cP. This polymer helped to

Table 1: Chemical properties of the soil at the start and at the end of the experiment.

No.	Chemical properties	Unit	Methods	Result		
				Before experiment	Control	Nanofertilizer
1.	Available P	mg/kg	TCVN 6499 : 1999*	120	113	172
2.	Total P	mg/kg	TCVN 8559 : 2010*	242	254	281
3.	S	mg/kg	TCVN 175 : 2015*	—	20.16	13.28
4.	Available K	mg/kg	TCVN 8662 : 2011*	59.4	73.2	81.3
5.	Si	mg/kg	US EPA method 3051: 2007 + SMEWW 3125 : 2017	374896	381569	400787
6.	Total organic C	mg/kg	TCVN 6634 : 2000*	8000	12000	10400
7.	Total N	mg/kg	TCVN 6498 : 1999*	2487	3357	2835
8.	Mg	mg/kg		3989	3701	3208
9.	Ca	mg/kg		13795	9522	10973
10.	Cu	mg/kg		22.71	19.36	19.77
11.	Fe	mg/kg	US EPA method 3051: 2007 + SMEWW 3125 : 2017	22576	18247	17384
12.	Zn	mg/kg		104.7	134.7	51.15
13.	Co	mg/kg		9.06	8.29	7.54
14.	Ag	mg/kg		0.66	0.32	0.42

*TCVN: Vietnam National Standards.

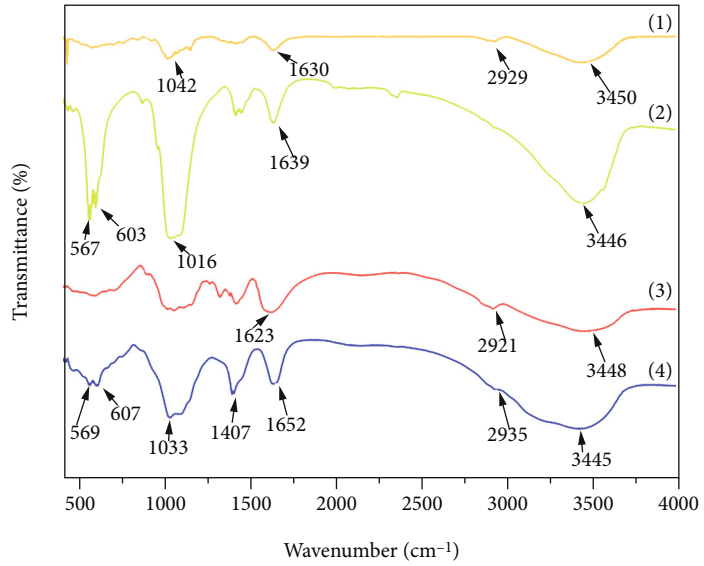

Figure 1: FTIR spectra of alginate (1), hydroxyapatite (2), carboxyl methyl cellulose (3), and the integrated nanofertilizer (4).

stabilize the obtained mixture [26]. The mixture was then further stirred for 24 h to obtain the integrated nanofertilizer.

The liquid nanofertilizer was diluted to use in field experiments. Dry samples of the nanofertilizer were obtained by free-drying method for characterization.

2.1.3. Characterization. Physicochemical characteristics of the obtained nanofertilizer were determined using various methods. The field emission scanning electron microscopy (FESEM) images were obtained by a Hitachi S-4800 instrument. The energy dispersive X-ray spectroscopic (EDX) technique was used to validate the elemental compositions and distribution of the samples in the same instrument. The high-resolution transmission (HR-TEM) images were obtained in a JEM 1010 system, while the Fourier Transformation Infrared spectra (FTIR) were recorded on a Shimadzu spectrophotometer using KBr pellets at 400–4000 cm^{-1} wavenumber range. The size distribution and Zeta potential of the fertilizer were measured in a Dynamic Light Scattering (DLS) system (Nano Zetasizer, Malvern UK).

2.1.4. Evaluation of the Effect of Nanoformulation on Plants. In this study, the growth indices such as plant height, leaf area, total dry production, and total biomass of *Polyscias fruticose* and *Asparagus officinalis* were used to prove the enhanced effects of nanofertilizer on supporting plant growth in comparison with control groups that were fertilized with commercial NPK and micronutrient fertilizers (NPK-15-15-15 + TE,

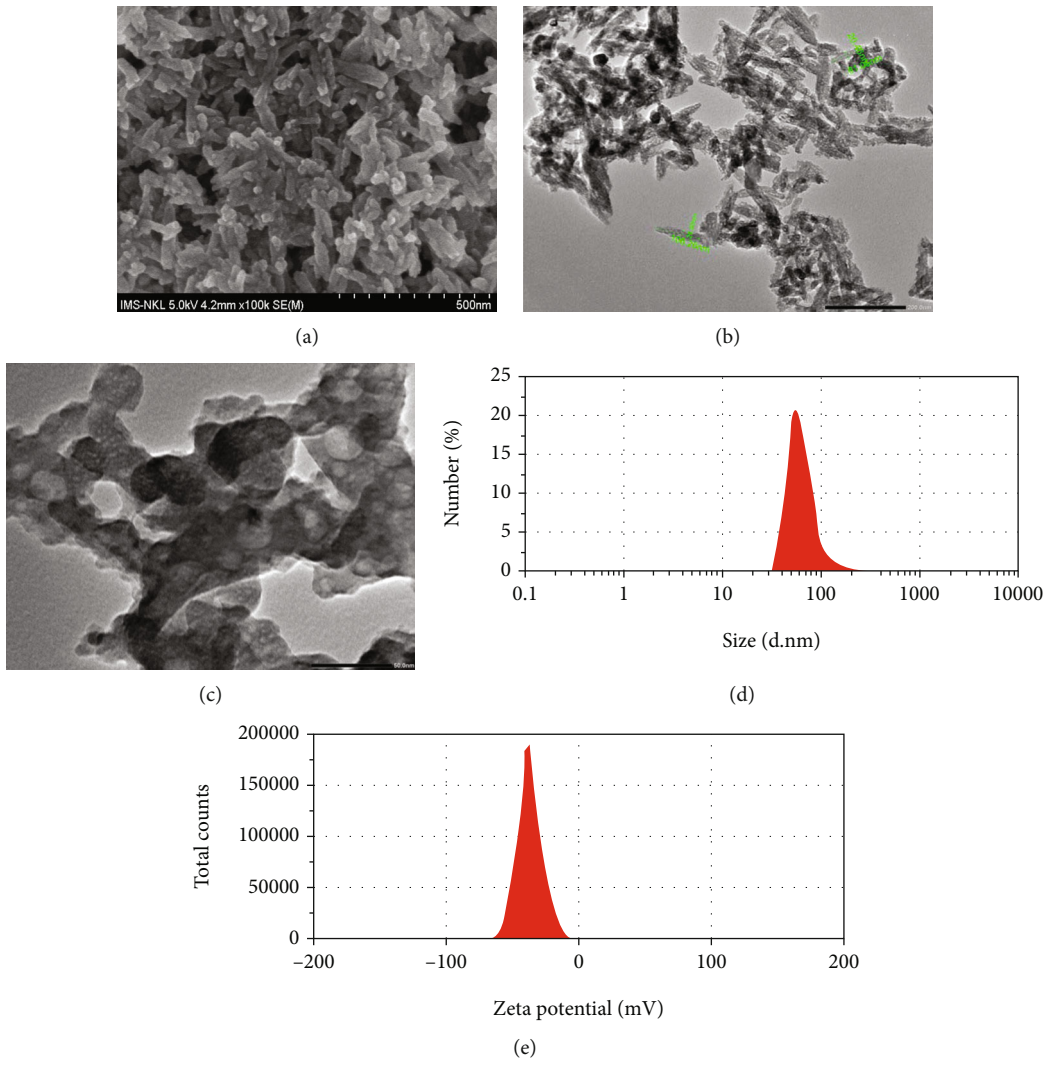

FIGURE 2: FESEM image (a) and HR-TEM image (scale bar: 200 nm) (b) of hydroxyapatite; HR-TEM image (scale bar: 50 nm) (c), size distribution (d), and Zeta potential (e) of the integrated nanofertilizer.

provided by Binh Dien Fertilizer Joint Stock Company, composition: total N: 15%, available P (P_2O_5): 15%; available potassium (K_2O): 15%, SiO_2: 1%, Zn: 100 ppm, Cu: 100 ppm, Fe: 100 ppm, and B: 200 ppm). The control groups were treated with 160 kg of NPK 15-15-15 + TE commercial fertilizer, 200 kg lime powder/ha twice a month. On the other hand, a diluted suspension (0.2% in irrigation water) of 10 L of the nanofertilizer was sprayed to the leaves and soil around the plant twice a month in nanofertilizer applied group that was approximately equal to only 5% of the NPK amount used in the control group.

The cultivation of *Polyscias fruticosa* and *Asparagus officinalis* was carried out by the Evergreen Agricoop Truong Xuan, Nam Dinh staff, with the assessed area of each experimental group which was 1 ha that were divided into 3 plots for triplicate measurement. The experiment lasted for 12 months for both *Polyscias fruticosa* and *Asparagus officinalis* in 2019-2020.

2.1.5. Soil Property Determination. Soil samples before and after the experiments were collected and analyzed for their properties. The analysis methods and obtained results are shown in Table 1.

2.1.6. Statistical Analysis. The obtained data are expressed as *mean* ± *SD*. The One-way analysis of variance (ANOVA) was performed to determine the statistical difference between the control and nanofertilizer groups.

3. Results and Discussions

3.1. Characteristics of the Integrated Nanofertilizer. In the Fourier–transform infrared (FTIR) spectrum (Figure 1) of hydroxyapatite, the strong band at 3446 cm^{-1} belonged to the valence vibration of the –OH group, while the weak absorption band at 1639 cm^{-1} represented the vibration of the CO_3^{2-} group. The strong absorption band at 1016 cm^{-1} belonged to the valence vibrations of the PO_4^{3-} group. The two bands at 567 cm^{-1} and 603 cm^{-1} could be assigned to the oscillations of the P-O bond. There were several shifts in the infrared spectrum of hydroxyapatite compared to that of the integrated nanofertilizer. These shifts included the changes in wave

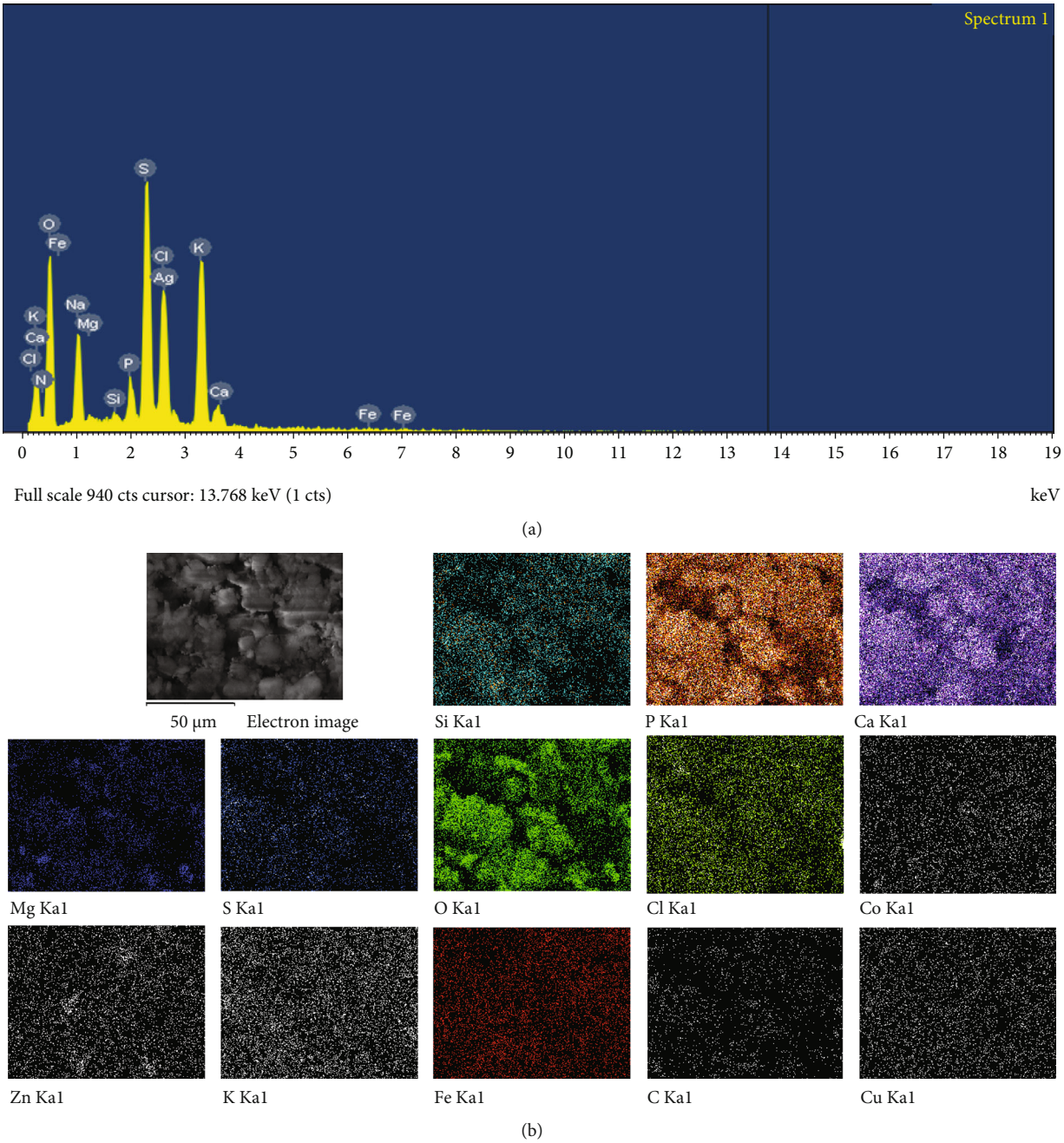

Figure 3: EDX spectrum (a) and EDX mapping (b) of the integrated nanofertilizer.

Table 2: Composition of the integrated nanofertilizer.

Element	N	P	K	Mg	S	Si	Ca	Fe	Cu	Zn	Co	Ag
% w/w	12.00	3.46	5.50	1.36	6.30	2.82	10.8	0.69	0.34	0.56	0.23	0.22

number from 3446 cm^{-1} to 3445 cm^{-1}; 1639 cm^{-1} to 1652 cm^{-1}; 567 cm^{-1} and 603 cm^{-1} to 569 and 607 cm^{-1}; and 1016 cm^{-1} to 1033 cm^{-1}. Besides, the moderate absorption bands at 2935 cm^{-1} in the integrated nanofertilizer corresponded to C-H (sp^3) valence vibration of alginate (2929 cm^{-1}) and carboxyl methyl cellulose (2921 cm^{-1}). For the synthesized nanofertilizer, a strong peak at 3445 cm^{-1} was assigned to the presence of -OH stretching vibration, while this absorption band also appeared at 3448, 3446, and 3450 cm^{-1} in the spectrum of carboxyl methyl cellulose, hydroxyapatite, and alginate polymer. In detail, the carbonyl bands (-C=O ester stretch) of alginate and carboxyl methyl cellulose appeared at 1630 and 1623 cm^{-}

Table 3: Effect of the integrated nanofertilizer on the number of secondary shoots, shoot length, dry matter production, leaf area, and leaf length of *Polyscias fruticosa*.

Sample	Number of branches/plant	Branch length (cm)	Dry matter production (g/plant)	Leaf area (m^2/plant)	Leaf length (cm)
Integrated nanofertilizer	7.8 ± 0.08^a	18.4 ± 0.2^a	126.48 ± 0.35^a	0.32 ± 0.05^a	23.2 ± 0.15^a
Control	5.2 ± 0.1^b	13.6 ± 0.4^b	88.57 ± 0.5^b	0.21 ± 0.07^b	18.5 ± 0.2^b

[a,b]Means in each column with the different letter are significantly different at $P = 0.05$.

Table 4: Effect of the integrated nanofertilizer on the number of roots, the total mass of roots, primary root length, and total biomass of *Polyscias fruticosa*.

Sample	Number of root branches	Total root mass (g/plant)	Primary root length (mm)	Total biomass (g/plant)
Integrated nanofertilizer	21.35 ± 0.12^a	23.5 ± 0.4^a	18.5 ± 0.2^a	149.8 ± 0.5^a
Control	14.44 ± 0.35^b	15.8 ± 0.5^b	13.2 ± 0.1^b	103.45 ± 0.65^b

[a,b]Means in each column with the different letter are significantly different at $P = 0.05$.

^{1}, respectively, while these bands were shifted to 1652 cm^{-1} in the FTIR spectrum of the integrated nanofertilizer. These results suggested that the new structure had been established based on hydroxyapatite.

The FESEM and TEM images of hydroxyapatite (Figures 2(a) and 2(b)) revealed the rod shape of the hydroxyapatite with the diameter ranging from 20 to 30 nm and about 80 to 100 nm in length. In TEM image of the nanofertilizer (Figure 2(c)), many round nanoparticles with various sizes from 5 to 20 nm appeared in the hydroxyapatite rods. This confirms the success of the combination of nutrients into the nanostructure of hydroxyapatite. Similar observation was also observed in another hydroxyapatite-based nanofertilizer [4].

In the solution, the particles had an average size of 86 nm and a highly negative zeta potential value of -42.3 mV (Figures 2(d) and 2(e)). The measurement results indicated that the nanofertilizer particles were stable. This colloid was much more stable than a reported organic nano-NPK formula [27]. Alginate and carboxylmethyl cellulose are highly hydrophilic polymers that play the role of stabilizers for the fertilizer [28, 29]. Using these polymers, the fertilizer can be used in the form of a colloidal solution.

The elemental composition of the nanofertilizer was determined by the EDX method (Figure 3(a)), and the results are shown in Table 2. The elemental mapping results (Figure 3(b)) provide a clear observation of the elements in the nanofertilizer. Ca, P, and O are the most abundant elements because they are the main compositions of hydroxyapatite. Other elements are found evenly distributed in the material. The results strongly revealed that the macro- and micronutrient elements were successfully integrated into the hydroxyapatite/alginate nanostructures with the expected ratio.

The effects of the commercial fertilizer and nanofertilizer on the soil parameters are listed in Table 1. The results show that some important parameters of available P, available K, total N, and total organic C of the soil samples after the experiment are higher than those of the sample before the experiment. Compared with the control group, applying nanofertilizer slightly increased the available P and K and slightly decreased the total N and total organic C. The similar effect on soil was observed when applying a slow release nanofertilizer with nitrogen, phosphorus, potassium, magnesium, calcium, and humic acid [22]. The amount of trace elements also varies among the samples and has the tendency to reduce after the experiments. This can be explained by the uptake of these elements from the soil of the plants. The elements can affect much on the growth, crop yield, and product quality of some plants [30, 31].

3.2. Effect of the Integrated Nanofertilizer on Polyscias Fruticosa. Observation on the development of *Polyscias fruticosa* was conducted after 150 days. The measurement results presented in Tables 3 and 4 proved the positive effect of nanofertilizer on plant growth, compared to the control group.

As described in Table 3 and Figure 4, the average branches number and their length were also increased from 5.2 ± 0.1 to 7.8 ± 0.08 and from 13.6 ± 0.4 to 18.4 ± 0.2 cm, respectively, in response to the nanofertilizer application.

The dry matter production of the plant is an index of the dry matter product accumulated on an area unit and is the result of a series of assimilation and catabolism processes during the growth of the plant. Using nanofertilizer resulted in the dry matter of 126.48 g/plant which was 1.5 times higher than the control of 88.57 g/plant. The ability of the plant to build up dry matter influences the formation of active ingredients in the *Polyscias fruticosa*, thereby affecting the quality of the medicinal plants (roots and leaves) after harvest. Using an integrated nanofertilizer helped to improve the ability to accumulate dry matter of *Polyscias fruticosa*, thereby increasing the value and economic benefits of the plant.

Additionally, the leaf area index (LAI) is defined as the ratio of one-sided leaf area per unit ground area. Under the same amount of light, a higher LAI indicates a larger photosynthetic active area, and thus a higher photosynthetic rate and productivity of the crop are achieved [32]. In the process of growth and development, the nanofertilizer treated *Polyscias fruticosa* reached a higher leaf length of 23.2 ± 0.15 cm and LAI of 0.32 ± 0.05 m^2/plant than that of 18.5 ± 0.2 cm and 0.21 ± 0.07 m^2/plant, respectively, in the control group. Consequently, the nanofertilizer utilization promoted plant

Figure 4: The growth of *Polyscias fruticosa* during the experiment time.

Table 5: Effect of the integrated nanofertilizer on the height, spear number, and average weight of *Asparagus officinalis* after 150 days.

Sample	Plant height (cm)	Average number of spears/cluster (spears/cluster)	Average weight/cluster (g/cluster)	Average weight of each spear (g)
Integrated nanofertilizer	93.1 ± 2.3^a	18.2 ± 3.85^a	193.25 ± 7.5^a	11.46 ± 2.33^a
Control	62.7 ± 3.12^b	8.7 ± 1.6^b	46.67 ± 3.33^b	6.12 ± 0.45^b

[a,b]Means in each column with the different letter are significantly different at $P = 0.05$.

photosynthesis capacity, thereby increasing their ability to accumulate higher dry matter and yield. These results were consistent with other reports on the effects of nanoformulas on maize [33]. Interestingly, the improvement in growth parameters achieved by the application of the integrated nanofertilizer was occurred at the nanofertilizer amount of only 5% compared to that of conventional fertilizer. This is an outstanding benefit of the integrated fertilizer. In comparison, a urea-hydroxyapatite nanohybrid leads to better rice crop yield at 50% lower concentration of urea [4]. Nanozeolite and nanohydroxyapatite at the same level of P with conventional fertilizer could increase the measured parameters including the plant height; branch number; sub-branch number; chamazulene amount; flower number; phosphorous content in the soil, root, and shoot; and fresh and dry weight of flower and shoot [6].

The primary function of the root is to absorb water, dissolved nutrients, and conduct to the stem. Plants that are provided adequate nutrients will have longer and deeper root set that reach out in all directions in the soil. When the root system grows well, it will create favorable conditions for the plant to grow and develop. Therefore, the number, weight, and length of the root systems were also monitored in this study. The detailed results are shown in Table 4.

In particular, the nanofertilizer treated group had an average of 21.35 roots per plant and a total root weight of 23.5 g/plant that was about 50% higher compared to the commercial fertilizer treated group. Similar trends were also observed for the average root length and total biomass (including stem and root). The difference of these parameters between the two groups was about 5.3 cm and 46.35 g/plant, respectively. It was confirmed that the roots of *Polyscias fruticosa* grew stronger in quantity, volume, and main root length under the supplement of nanofertilizer. Moreover, *Polyscias fruticosa* is well-known for the accumulation of glucosides, alkaloids, saponins, triterpene, tannins, 13 amino acids, vitamin B1, and many other active ingredients in their roots [34]. When the roots grow well, the content of the ingredients can be increased. Especially the content of saponin, which has a good effect on 5 organs and the ability to detoxify, increase blood and milk production, digest support, reduce inflammation, treat coughs and enhance memory, and prevent fatigue, can be significantly improved when using of nanofertilizer. Hence, further investigation is necessary to evaluate whether the nanofertilizer application would result in higher content of active ingredients when harvesting (3 years since planted). Further research is in progress.

Figure 5: Asparagus officinalis was grown and monitored at the Evergreen Agricoop Truong Xuan, Nam Dinh.

Table 6: The effect of integrated nanofertilizer on some asparagus growth indicators after 12 months.

Sample	Plant height (cm)	Length of root (m)	Spear diameter (cm)	Average weight of each spear (g)
Integrated nanofertilizer	205.46 ± 5.5^a	1.92 ± 0.27^a	1.2 ± 0.3^a	16.23 ± 2.33^a
Control	178.12 ± 4.33^b	0.71 ± 0.17^b	0.9 ± 0.2^b	9.74 ± 1.89^b

[a,b]Means in each column with the different letter are significantly different at $P = 0.05$.

3.3. Effect of the Integrated Nanofertilizer on Asparagus Officinalis. Asparagus is a shrub, herbaceous, coniferous plant. Research on the development of asparagus spears of asparagus plants was conducted on the height and weight of the spears. The results of evaluating the effects of integrated nanonutrients on some growth indicators of *Asparagus officinalis* in the first stage of 150 days are presented in Table 5.

After 150 days of cultivation, the height of *Asparagus officinalis* in the group that received the integrated nanofertilizer was 93.1 ± 2.3 *cm*, which was 1.5 times higher than the control group of 62.7 ± 3.12 *cm*. The average number of spears/cluster in the nanofertilizer treated group was 18.2 spears/clump, and an average clump weight of 193.25 g/cluster that was also 2 times higher than the NPK treated group with the average number of spears/clump and average clump weight were 8.7 spears/clump and 46.67 g/cluster, respectively. Additionally, the average weight of a young shoot in the nanonutrient group of 11.46 g was almost twice as high as that of 6.12 g in the control group. Thus, in the early stage of asparagus growth (150 days), it could be seen that nanonutrients played an important role in promoting the growth rate compared to the nontreated group (Figure 5).

For a clearer view, the effect of integrated nanofertilizer on the growth and development of Asparagus officinalis was continued to monitor after 12 months. Data are presented in Table 6.

As shown in Table 6, the height of asparagus plants in the group using integrated nanofertilizer increased to 205.46 cm, higher than that of the control group of 178.12 cm. Along with that, the improvement of root length, diameter, and average weight of the spear were also observed when integrated nanofertilizer were used (Table 6 and Figure 6). The root length of asparagus in the experimental group using integrated nanofertilizer was 1.92 m, which was 2.7 times longer than the control group using conventional fertilizers (0.71 m). Spears in the group using the integrated nanofertilizer had a diameter of 1.2 cm and an average weight of each spear of 16.23 g. It was higher than the spears in the control group which had the spear diameter of 0.9 cm and an average weight of each spear of 9.74 g. This proves the effectiveness of applying integrated nanofertilizer to asparagus planting process, and the growth and development of plants and spears are faster than that of conventional fertilizers.

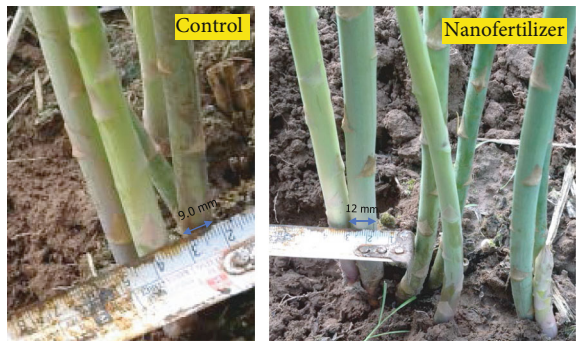

Figure 6: Different in spear diameter of the commercial fertilizer applied group (a) and integrated nanofertilizer applied group (b) after 12 months.

While some nanofertilizers were studied for their properties only [15, 16, 18, 19], some recent reports also suggested that nanofertilizer could improve the crop yield and quality. However, the nanofertilizer levels applied in these investigations were similar to that of conventional fertilizers [12, 35]. Using such a low level of the integrated fertilizer (5% compared to conventional fertilizer) could effectively reduce environmental pollution [36].

4. Conclusion

In conclusion, multinutrient contained nanofertilizer was synthesized by a simple method and successfully used to improve the growth indices of *Polyscias fruticosa* and *Asparagus officinalis* with only 5% amount of conventional fertilizer. Thus, this novel nanofertilizer could be a promising approach for the sustainable development of agriculture in terms of enhancing productivity. Further investigation will be carried out to evaluate the interactions of the nanofertilizers and biological systems or food chains before its massive application in agriculture.

Data Availability

The data used to support the findings of this study are included within the article.

Conflicts of Interest

The authors declare that there is no conflict of interest.

Acknowledgments

This work was financially supported by the Vietnam Academy of Science and Technology under Grant No. UDSPTM.02/20-21.

References

[1] N. Cui, M. Cai, X. Zhang et al., "Runoff loss of nitrogen and phosphorus from a rice paddy field in the east of China: effects of long-term chemical N fertilizer and organic manure applications," *Global Ecology and Conservation*, vol. 22, article e01011, 2020.

[2] C. O. Dimkpa and P. S. Bindraban, "Nanofertilizers: new products for the industry?," *Journal of Agricultural and Food Chemistry*, vol. 66, no. 26, pp. 6462–6473, 2018.

[3] A. Ditta and M. Arshad, "Applications and perspectives of using nanomaterials for sustainable plant nutrition," *Nanotechnology Reviews*, vol. 5, no. 2, pp. 209–229, 2016.

[4] N. Kottegoda, C. Sandaruwan, G. Priyadarshana et al., "Urea-hydroxyapatite nanohybrids for slow release of nitrogen," *ACS Nano*, vol. 11, no. 2, pp. 1214–1221, 2017.

[5] J. C. Tarafdar, R. Raliya, and I. Rathore, "Microbial synthesis of phosphorous nanoparticle from tri-calcium phosphate using aspergillus tubingensis TFR-5," *Journal of Bionanoscience*, vol. 6, no. 2, pp. 84–89, 2012.

[6] A. Mikhak, A. Sohrabi, M. Z. Kassaee, and M. Feizian, "Synthetic nanozeolite/nanohydroxyapatite as a phosphorus fertilizer for German chamomile (Matricariachamomilla L.)," *Industrial Crops and Products*, vol. 95, pp. 444–452, 2017.

[7] J. Kihara, P. Bolo, M. Kinyua, J. Rurinda, and K. Piikki, "Micronutrient deficiencies in African soils and the human nutritional nexus: opportunities with staple crops," *Environmental Geochemistry and Health*, vol. 42, no. 9, pp. 3015–3033, 2020.

[8] M. E. Williams, "Plant Nutrition 3: Micronutrients and metals," *The Plant Cell*, vol. 27, article tpc.115.tt0515, 2015.

[9] M. S. Vaghar, S. Sayfzadeh, H. R. Zakerin, S. Kobraee, and S. A. Valadabadi, "Foliar application of iron, zinc, and manganese nano-chelates improves physiological indicators and soybean yield under water deficit stress," *Journal of Plant Nutrition*, vol. 43, no. 18, pp. 2740–2756, 2020.

[10] S. K. Dhoke, P. Mahajan, and A. S. Khanna, "Effect of nano-ZnO particle suspension on growth of mung (Vigna radiata) and gram (Cicer arietinum) seedlings using plant agar method," *Journal of Nanotechnology*, vol. 2011, Article ID 696535, 2011.

[11] L. Zhou, D. Cai, L. He et al., "Fabrication of a high-performance fertilizer to control the loss of water and nutrient using micro/nano networks," *ACS Sustainable Chemistry & Engineering*, vol. 3, no. 4, pp. 645–653, 2015.

[12] H. S. El-Desouky, K. R. Islam, B. Bergefurd et al., "Nano iron fertilization significantly increases tomato yield by increasing plants' vegetable growth and photosynthetic efficiency," *Journal of Plant Nutrition*, vol. 44, pp. 1–15, 2021.

[13] C. Gupta and P. Dhan, "Effect of nano-fertilizers on soil microflora," *Annals of Plant Sciences*, vol. 9, pp. 3846–3859, 2020.

[14] M. R. Pandao, M. Sajid, J. Katore, S. S. Patil, and M. B. Nirgulkar, "Effect of nano zinc oxide on growth, yield and uptake of nutrient by linseed," *International Journal of Chemical Studies*, vol. 9, no. 1, pp. 176–179, 2021.

[15] M. A. Melaj and M. E. Daraio, "HPMC layered tablets modified with chitosan and xanthan as matrices for controlled-release fertilizers," *Journal of Applied Polymer Science*, vol. 131, no. 19, pp. 1–7, 2014.

[16] S. Noppakundilograt, N. Pheatcharat, and S. Kiatkamjornwong, "Multilayer-coated NPK compound fertilizer hydrogel with controlled nutrient release and water absorbency," *Journal of Applied Polymer Science*, vol. 132, no. 2, pp. 1–11, 2015.

[17] M. B. Taşkın, Ö. Şahin, H. Taskin, O. Atakol, A. Inal, and A. Gunes, "Effect of synthetic nano-hydroxyapatite as an alternative phosphorus source on growth and phosphorus nutrition of lettuce (Lactuca sativa L.) plant," *Journal of Plant Nutrition*, vol. 41, no. 9, pp. 1148–1154, 2018.

[18] E. I. Pereira, C. C. T. Da Cruz, A. Solomon, A. Le, M. A. Cavigelli, and C. Ribeiro, "Novel slow-release nanocomposite nitrogen fertilizers: the impact of polymers on nanocomposite properties and function," *Industrial and Engineering Chemistry Research*, vol. 54, no. 14, pp. 3717–3725, 2015.

[19] N. Kottegoda, I. Munaweera, N. Madusanka, and V. Karunaratne, "A green slow-release fertilizer composition based on urea-modified hydroxyapatite nanoparticles encapsulated wood," *Current Science*, vol. 101, pp. 73–78, 2011.

[20] M. Fatollahpour Grangah, V. Rashidi, B. Mirshekari, E. Khalilvand Behrouzyar, and F. Farahvash, "Effects of nano-fertilizers on physiological and yield characteristics of pinto bean cultivars under water deficit stress," *Journal of Plant Nutrition*, vol. 43, no. 19, pp. 2898–2910, 2020.

[21] M. Morsy and A. Ahmed, "Response of two yellow maize hybrids to amino acids, mineral Npk and nano-fertilizers under Toshka District conditions," *Alexandria Science Exchange Journal*, vol. 42, no. 2, pp. 327–340, 2021.

[22] Q. Teng, D. Zhang, X. Niu, and C. Jiang, "Influences of application of slow-release nano-fertilizer on green pepper growth, soil nutrients and enzyme activity," in *IOP Conference Series: Earth and Environmental Science*, p. 208, Hong Kong, China, 2018.

[23] K. S. Phan, H. T. Nguyen, T. T. H. Le et al., "Fabrication and activity evaluation on Asparagus officinalis of hydroxyapatite

based multimicronutrient nano systems," *Advances in Natural Sciences: Nanoscience and Nanotechnology*, vol. 10, no. 2, article 025011, 2019.

[24] L. J. W. J. Gilissen, "Chapter 5 - food, nutrition and health in the Netherlands," in *Nutritional & Health Aspect-Traditional & Ethnic Food*, B. Susanne, Z. Christina, A. Dimitrios, and C. H. F. Javier, Eds., pp. 85–108, Academic Press, 2020.

[25] P. T. Tran, N. H. Dang, O. Kim et al., "Ethanol extract of Polyscias fruticosa leaves suppresses RANKL-mediated osteoclastogenesis in vitro and LPS-induced bone loss in vivo," *Phytomedicine*, vol. 59, article 152908, 2019.

[26] F. He, D. Zhao, J. Liu, and C. B. Roberts, "Stabilization of Fe –Pd nanoparticles with sodium carboxymethyl cellulose for enhanced transport and dechlorination of trichloroethylene in soil and groundwater," *Industrial and Engineering Chemistry Research*, vol. 46, no. 1, pp. 29–34, 2007.

[27] P. M. Nibin, K. Ushakumari, and P. K. Ishrath, "Organic Nano NPK formulations on soil microbial and enzymatic activities on post-harvest soil of Bhindi," *International Journal of Current Microbiology and Applied Sciences*, vol. 8, no. 4, pp. 1814–1819, 2019.

[28] E. Grządka, J. Matusiak, A. Bastrzyk, and I. Polowczyk, "CMC as a stabiliser of metal oxide suspensions," *Cellulose*, vol. 27, no. 4, pp. 2225–2236, 2020.

[29] J. Guan, Y. Zhang, Q. Liu, X. Zhang, R. Chokshi, and S. Mao, "Exploration of alginates as potential stabilizers of nanosuspension," *AAPS PharmSciTech*, vol. 18, no. 8, pp. 3172–3181, 2017.

[30] S. H. J. Al-Hchami and T. K. Alrawi, "Nano fertilizer, benefits and effects on fruit trees: a review," *Plant Archives*, vol. 20, pp. 1085–1088, 2020.

[31] Q. B. Ngo, T. H. Dao, H. C. Nguyen et al., "Effects of nanocrystalline powders (Fe, Co and Cu) on the germination, growth, crop yield and product quality of soybean (Vietnamese species DT-51)," *Advances in Natural Sciences: Nanoscience and Nanotechnology*, vol. 5, no. 1, article 015016, 2014.

[32] J. K. Kim, K. J. Park, K. S. Cho, S.-W. Nam, T.-J. Park, and R. Bajpai, "Aerobic nitrification-denitrification by heterotrophic Bacillus strains," *Bioresource Technology*, vol. 96, no. 17, pp. 1897–1906, 2005.

[33] J. Estrada-Urbina, A. Cruz-Alonso, M. Santander-González, A. Méndez-Albores, and A. Vázquez-Durán, "Nanoscale zinc oxide particles for improving the physiological and sanitary quality of a Mexican landrace of red maize," *Nanomaterials*, vol. 8, no. 4, p. 247, 2018.

[34] N. Q. Nguyen, M. T. Nguyen, V. T. Nguyen et al., "The effects of different extraction conditions on the polyphenol, flavonoids components and antioxidant activity of Polyscias fruticosa roots," *IOP Conference Series: Materials Science and Engineering*, vol. 736, 2020.

[35] N. I. Abu-Elsaad and R. E. Abdel hameed, "Copper ferrite nanoparticles as nutritive supplement for cucumber plants grown under hydroponic system," *Journal of Plant Nutrition*, vol. 42, no. 14, pp. 1645–1659, 2019.

[36] A. Abbasifar, F. Shahrabadi, and B. ValizadehKaji, "Effects of green synthesized zinc and copper nano-fertilizers on the morphological and biochemical attributes of basil plant," *Journal of Plant Nutrition*, vol. 43, no. 8, pp. 1104–1118, 2020.